GaAs-Based Integration Photonics: Waveguides and Splitting Elements

A thesis submitted in fulfilment of the partial requirement for the degree of Doctor of Philosophy

by

Tahani Raja S. Albiladi

School of Physics and Astronomy - Cardiff University

UK

September 2022

Abstract

With the development of long lived, epitaxially grown InAs quantum dot lasers in GaAs on silicon, GaAs-based photonics has become a promising system for integrating large numbers of small footprint active and passive components on the same substrate. To ensure high performance of a circuit, each component or building block, needs to be individually investigated so a library of optimised components can be developed.

In this thesis, several GaAs-based passive integrated photonic components are proposed and analysed by employing commercially available multi-dimensional simulation tools with the aim of understanding the performance and tolerances of the important component functions prior to the manufacturing stage. These components will be useful as basic and composite building blocks in future GaAs-on-silicon photonic integrated circuits.

Deeply etched waveguides are investigated, and single mode operation is shown to be maintained under ± 0.1 µm variation in width, etching depth, core height and variation in wavelength between 1.2 and 1.4 µm, making the waveguides tolerant against typical fabrication errors. Single mode operation is also mapped as a function of core width, height and etching depth for shallow etched waveguides.

Efficient tapers are optimised for the propagation of light between multimode and single mode waveguides. The tapers are tolerant of width, etching depth and wavelength changes of $\pm 0.1 \mu m$ with transmission higher than 98%.

Two compact splitters: multimode interferometer, MMI, and Y-branch are optimised at 1.3 µm. The multimode interferometer has efficiency up to ~99% with reduction of ~4% over spectral and geometrical changes of width, length and etching depth of $\pm 0.1 \mu m$. An efficient Y-branch is designed with efficiency up to 94% with less stability, compared to the multimode interferometer, against variations like etching depth and wavelength. It is found that waveguides of single mode operation at 1.3 µm are achievable and efficient tapers and splitters can be obtained within the

fabrication capabilities available in a university facility. Hence, these components are appropriate for on-chip integration.

Acknowledgements

First of all, I would like to express my sincere appreciation and thanks to my supervisors, Prof. Peter M. Smowton and Dr. Daryl M. Beggs, for accepting me under their supervision, invaluable advice, patience and continuous moral and academic support. My thanks extend to Dr. Mikako Matsuura for her mentorship. Thanks also should go to Optoelectronic group members for their generous support. Special thanks to my PhD mate, Fwoziah, for her wonderful inspiration, understanding and continual support and advice.

I also, would like to thank King Saud University and Saudi Bureau in London for the scholarship that allowed me conducting this project.

Lastly, words cannot express my deepest gratitude to my parents, husband, siblings, children and friends. It would be impossible to complete my study without their great encouragement, endless understanding and thoughtful prayers.

Contents

List of Abbreviations

1D	One Dimensional
2 D	Two Dimensional
BCB	Benzocyclobutene
CWDM	Course Wavelength Division Multiplexing
DBR	Distributed Bragg reflector laser
DUV	Deep Ultraviolet lithography
DWDM	Dense Wavelength Division Multiplexing
E-beam	Electron Beam lithography
EIM	Effective Index Method
EUV	Extreme Ultraviolet lithography
FDM	Finite Difference Method
FMM	Film Mode Matching
FTTC	Fibre-To-The-Cabinet
FTTH	Fibre-To-The-Home
LED	Light Emitting Diode
OCT	Optical Coherence Tomography
QD	Quantum Dot
TE	Transverse Electric Mode
TM	Transverse Magnetic Mode
UV	Ultraviolet lithography

Software

Here is included a list of the software used in the simulations and calculations presented in this thesis,

1- Fimmwave (version 7.2 and 7.3): is a commercial software by Photon Design used to run simulation in 1 D and 2 D waveguides. Effective index, Film mode matching and Finite difference solvers were used to study waveguides.

2- Fimmprop (version 7.2 and 7.3) is extension of Fimmwave that treats light propagation situations using Eigenmode expansion method.

3- Python (version 2.7) where codes were created to automate control the parameters in Fimmwave and Fimprop.

List of Figures

List of Tables

Chapter 1 :

Integrated Photonic Circuits

In this chapter, I will give a brief background description of photonic integration technology, components and fabrication techniques. I will describe the GaAs/AlGaAs structure that will be used and give a summary of previous work. I will highlight the significance and motivation of extending photonic integration to a GaAs-based material system at ~1.3 µm.

1.1   Thesis Aims

Long lifetime, epitaxially grown InAs quantum dot lasers based on a GaAs crystal lattice and grown directly on silicon are exciting for the future integration of electronic components, typically done in silicon, and photonic components. There are several different ways that optical components could be integrated with such laser sources and much progress has been made developing silicon photonic components [1], [2]. GaAs-based photonics is also a promising system for integrating large numbers of small footprint active and passive components on the same substrate, without the need to couple light between silicon and the III-V material. To ensure high performance of a circuit, each component, building block, needs to be individually investigated through several steps, namely: structure (passive or active material system) design, basic building block design, composite building block design. The aim of this work is to develop a full understanding of the structure/components performance and tolerances prior to manufacturing stage by using commercially available multi-dimensional simulation tools. This work should lead to reduced raw material consumption, time and cost of both fabrication and characterisation. Ultimately a library of optimised components can be developed efficiently for high performance on-chip integration. I will examine several GaAs-based passive components, basic and composite, and suitable for integrated photonics at a wavelength ~1.3 µm. Compactness and fabrication tolerances will be considered and the spectral response considered from 1.2 to 1.4 µm.

1.2   What is Integrated Photonics?

Computational power and the capacity of data communication are growing exponentially as observed back in 2011 [3]. Data hungry technologies such as the

proliferation of YouTube videos and the trend to cloud computing have exacerbated and accelerated this growth [4], [5]. The necessity of controlling and transferring an extremely large amount of data requires huge bandwidth which can be provided by the high frequency of the light. Optical fibres have been installed worldwide to facilitate these communications, as they can transmit light signals large distances with low loss ~ 0.15 dB/km [6] and wavelength division multiplexing is now used to transmit channels at different wavelengths across a wavelength range from 1260 – 1610 nm as illustrated in Figure 1.1 and Table 1.1.
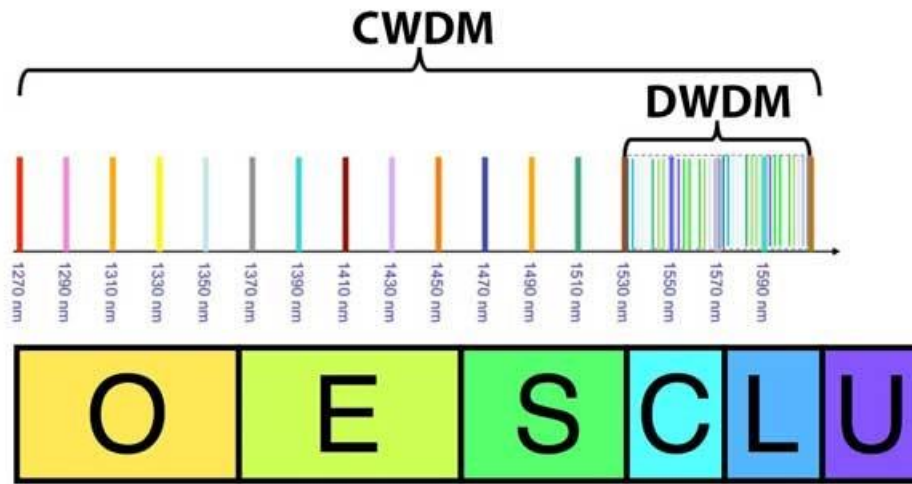
Figure 1.1: Coarse (CWDM) and Dense (DWDM) wavelength division multiplexing channels [7]**.**

Table 1.1: The optical bands and their uses [8]**.**

Band	Range	Uses
O	1260 – 1360 nm	Optical communications
E	1360-1460 nm	Optical communications (limited)
S	1460-1530 nm	Passive optical network systems
C	1530-1565 nm	Long-distance transmission systems
L	1565-1625 nm	Submarine cable operators
U	1625 – 1675 nm	Network monitoring

As the need for bandwidth increases, these optical communications move closer to the end-user, with fibre-to-the-cabinet (FTTC) being standard for broadband, and the roll-out of fibre-to-the-home (FTTH). Optical communications have already largely replaced electrical ones within data centres, and future developments are expected to see optical communications replace electrical ones even at chip level. These chip-level optical interconnects will provide the needed bandwidth for communications between computing cores on massively parallel computing chips and have also been suggested as the basis for an optical quantum computer.

In addition to communication functions being miniaturised on chip there are a variety of sensing functions that can be supported by similar technology. Reducing the size and weight of bulk optics solutions will open up more applications for these sensing technologies. An example is optical coherence tomography (OCT) [9], [10], which is used, for example, by opticians for studying the retina using wavelengths around $1.3\,\mu m$ and which could be applied in point-of-use or home setting, if miniaturised, for identifying skin cancers. For such an application, a broad band or tuneable wavelength from $1.2 - 1.4\,\mu m$ produces the highest resolution measurement and in this thesis I will adopt this wavelength range for testing the performance of the components I will investigate.

For purposes of chip-level or integrated optical communications and applications of photonic devices, the material requirements are a dielectric material that is transparent to light at the appropriate frequencies extended from the visible to the near-infrared light and can be used in top-down fabrication processes such as lithography and etching. Many semiconductors meet this requirement for frequencies beyond the band-edge. Silicon is a popular choice, as the silicon industry is mature and can provide off-the-shelf technologies like silicon-on-insulator, and fabrication processes are mature.

Due to expanding communication systems and increment of the transferred data amounts, there is a need to develop faster, higher performance, small sized and low-cost systems. Therefore, the integrated photonic systems have been made with several types of materials.

Optical systems have developed through three different generations:

1- The conventional optical system with beam diameter of order of millimetres and several centimetres components size that are usually fixed on an optical bench of dimension of meters. Some of this system's elements are mirrors, prisms and lenses.

2- The micro-optics system which uses reduced elements like diode lasers and emitting diodes that need difficult alignment when they are connected to each other.

3- The integrated photonic system which has the feature of small components size (~ micrometres).

Generic photonic integration is the technology where several basic building blocks are integrated on a common planner chip to generate vast functionalities of controlling light characteristics like the amplitude, phase and polarisation. To have a wider capability of applications (e.g., optical communication), the basic building blocks are combined to build more complex optical components known as composite building blocks. However, the essential element of the integrated photonics is the waveguide and light confinement is the fundamental idea. Generally, the light can be confined by using media, the upper and lower claddings, with particular refractive indices enclosing a medium, the core, with higher refractive index. Thus, most of the light is confined by the boundaries of the core as result of the total internal reflection at the core/claddings interfaces.

1.2.1   System Characteristics

The integrated photonic system has some characteristics that make it preferable and more reliable.

1- The broad range of applications can be covered efficiently by fabricating a number of basic building blocks.

2- The ability of combining different designs (and connection between them by waveguides) for multi-purpose on a single chip, multi-project wafer, in the same process. Hence, the difficulty and cost of the alignment is avoidable during fabrication process.

3- The multi-project wafer offering tiny, precise and very efficient light devices. Furthermore, it helps to minimise consuming raw materials substantially.

4- High reduction of costs results from the simulation and customizing the multi-project wafer fabrication [11], [12].

Today, there are various devices made on different material substrates depending on the specific application of the device. One of the most promising materials are III–V semiconductors, particularly GaAs and InP [12]. The InP-based device integration is more developed than the GaAs-based ones because GaAs based structures tend to include AlGaAs, which is more problematic when exposed to air due to oxidation. However, the use of Quantum Dots (QDs) with GaAs based materials is significantly more advanced and QDs have been shown to exhibit a number of advantages for generic integration such as the wide wavelength coverage. Problems with AlGaAs can also be removed by replacing AlGaAs with GaInP and so GaAs-based devices are now again of real interest for academic research and development of generic photonics.

1.2.2   Building Blocks

Waveguides are the basic optical element where the light is transmitted, generated or manipulated. The waveguides can be constructed from active or passive materials depending on the desired application. They also can be designed, as waveguides of different dimensions that have different properties for different functions and conditions. In simple terms, the waveguides can be said to be constructed from a core and the cladding, although each may be made-up of several layers in an epitaxial material based on GaAs. The material of each layer is chosen in order for the waveguide to obey the total internal reflection rules, i.e., the core refractive index is higher than that of the cladding layers. On top of that, the composition of the active material in the waveguide core is engineered to emit a particular wavelength in the case of lasers or LEDs. Ideally, the waveguides are used to compose the basic building blocks and to connect the component to each other [11]. Basic building blocks are the essential operative components that are formed by the waveguides including semiconductor optical amplifiers, saturable absorbers, photodetectors, etc. If two or more basic building blocks are combined, then a composite building block is designed (see Figure 1.2). One of the major

aims of this technology is to keep the design as simple as possible by using a limited number of basic building block. Arrayed waveguide grating (de)multiplexers, Mach-Zehnder interferometers, multimode interferometer and Y-branch are examples of composite building blocks. [11].
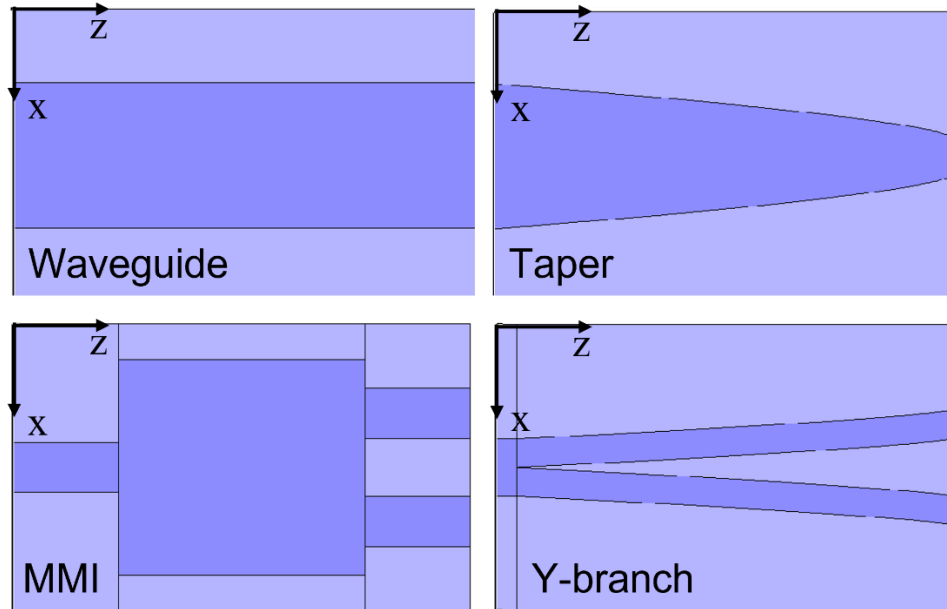
Figure 1.2: Top view (xz plane) of some photonics building blocks. The devices widths are along x-axis and the propagation is along the z-axis.

1.2.3   Fabrication Techniques

Based on lithography, fabrication techniques are basically divided into two main types: electron beam (e-beam) lithography and photolithography (UV lithography).

E-beam lithography is a direct write technique and is therefore slow; it is good choice for low-volume manufacturing with resolutions below 10 nm available [13]. This resolution is due to electrons' small wavelengths (typically ~0.1 nm for high energy electrons) which means e-beam is not diffraction limited, but instead is limited by forward scattering of electrons as they interact with the resist.

On the other hand, ultraviolet (UV) lithography is an indirect write technique. A mask is needed to define the wanted pattern onto the wafer, but the whole wafer can be exposed simultaneously, making it very quick and preferable for high-volume manufacturing where economies of scale can be used. However, compared

to e-beam, UV lithography resolution is far worse as it is diffraction limited [14]. For UV lithography, the critical dimension, or resolution R, depends on several parameters:

$$R = k_1 \frac{\lambda}{NA} \tag{1.1}$$

where k_1 is a processing factor which ranges between 0.5 to 0.8, for modern fabrication depending on resist quality and techniques of resolution enhancement. NA is the numerical aperture of the system (~0.5-0.6) and λ is the wavelength used in the process [15]. So, it is clear that the resolution is controlled by the wavelength used for a specific process.

In our facilities, in Cardiff University, the mercury lamp I-line (365 nm) is used and a waveguide width of 1.0 ± 0.1 μm can be achieved. However, fabrication limitations can be much better using other techniques where feature size limits are about 150 nm and 20 nm related to deep ultraviolet (DUV) and extreme ultraviolet (EUV) lithography, respectively [16], [17].

1.3   GaAs/AlGaAs Material System

Many attractive optical properties take place near the band edge of a semiconductor. Hence, the semiconductors are a worthy choice to build the photonic devices and photonic integrated circuits [18]. Several types of materials have been used to integrate photonic circuits including glasses, lithium niobate, silica on silicon, III-V semiconductor compounds and polymers. Silicon substrates are mainly used to fabricate passive devices, for purposes of modulating the phase and intensity of the light, owing to the indirect band gap. One of many advantages of Si-based photonics may be the ability of better control the mode size to coincide with that of the optical fibre and hence low loss is resulted from the circuit-fibre coupling [19]. For optical communication, III–V semiconductor composition, particularly GaAs and InP, are one of the most promising materials where both active and passive devices can be employed [12]. However, GaAs-based technology has an advantage with regard to quantum dots, where it is more advanced in comparison of InP-based devices [20] and also benefits from cheaper and larger area substrates. To generate and amplify the

light, photonic integrated circuits are assembled on a direct band gap semiconductor substrate composition: like InP and GaAs [21]. Regarding active devices, temperature insensitive InAs/InGaAs/GaAs quantum dot laser and ring laser operating in the spectral range of ~1.3 μm with high-performance have been reported [22], [23].

GaAs is a semiconducting material composed of a group III element, Ga, and a group V element, As. In comparison with Si, GaAs has some properties make it preferred over silicon for applications like digital circuits and fabricating optical components. First, electrons move relatively faster in GaAs and hence, devices can operate at higher frequencies through direct electrical modulation. Second, the ability of producing GaAs as semi-insulating substrate warrants operating monolithic integrated circuits at speeds above 1 GHz with low power dissipation. Third, GaAs has a direct band gap (Figure 1.3) which means electrons do not need to interact with the lattice to change their momenta to make transitions between the upper and lower band GaAs. Therefore, GaAs is suitable to fabricate lasers and LEDs [24].
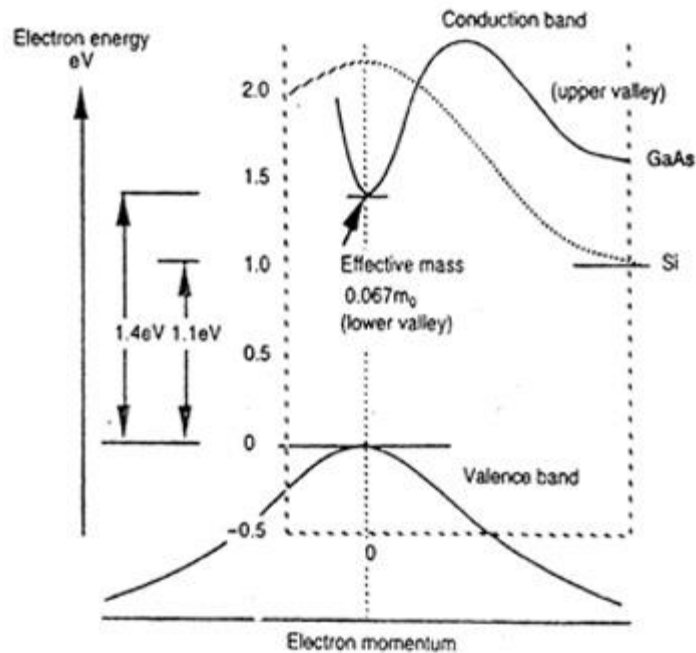
Figure 1.3: Energy bands structure of Si and GaAs [25]**.**

1.3.4   Timeliness and Importance of This Work

Different GaAs-based quantum dot lasers have been reported of emission centred around 1.3 μm [22], [23], [26]. This wavelength is suitable for wide range of

applications like optical coherence tomography (OCT) [9], [10]. In addition, 1.3 µm matches one of the optical fibre maximum transparency windows and hence suitable for data transfer and communications. Therefore, this research on GaAs structures investigates several designs of passive components that are suitable for integration with active devices and operate in the infrared region, namely ~1.3 µm.

Previous work has been completed on GaAs based passive photonic components and a summary of that work is presented to set the context. The beam propagation method has been used to investigate deep etched waveguides and study higher modes leaking into a second lower cladding (of different Al fraction) for single mode width design. It has been found that the fundamental mode has much lower losses than those of the first higher mode through the second lower cladding [27]. Similarly, low loss, deep etched, wide single mode waveguides with width, up to 5 µm, were designed using the discrete spectral index method at 1.064 and 1.319 µm. This method track the leaking to the GaAs substrate through the lower cladding to estimate the mode losses [28]. Furthermore, fundamental TE and TM degenerate, deep etched waveguide width was obtained at 1.55 µm using a vector finite element method to avoid critical guide width at which mode type conversion would happen. The critical widths have been experimentally investigated and reported for both symmetric and asymmetric, due to nonvertical etching, waveguides [29]. Also, electrooptic modulators were studied by developing a 1D approximation. Based on vertical sidewalls deep etched waveguide, 1 D modulator has been presented and compared with experiment with good agreements [30]. Regarding geometry optimisation, mode behaviour was studied to optimise waveguides for mid infrared spectroscopy applications by finite-element based simulation. An optimal waveguide dimensions for chem/bio sensing applications have been found [31].

For large size waveguides, single mode cut-off width of large core waveguide was found at 1.55 µm at two etching depths using the beam propagation method. Results have been experimentally verified where better confinement and circular mode profile were obtained by deeper etched waveguide [32]. In addition, the effective index method was used to design a five layer heterostructure GaAs/AlGaAs based waveguide for single mode operation at ~1.3 µm. Low loss, 4.3 µm wide waveguide has been realized and can be used to fabricate low loss modulators [33].

With regards to lateral tapering, a taper of length of 500 μm was simulated for low loss waveguide-fibre coupling using beam propagation method [27]. Also, a tapered waveguide length was optimised to connect deep and shallow etched waveguides for the purpose of lateral mode-size conversion at a wavelength of 785 nm by eigenmode expansion method [34]. For spot size conversion functionality of high-speed electrooptic, a more than 1 mm long tapered waveguide modulator was examined at 1.55 μm using the beam propagation method [35].

Multimode interferometers (MMI) were studied with shallow (length of 830 μm) and deep (111 μm long) etching levels for GaAs based structures by beam propagation method. It has been found that the deep etched MMI has better functionality than that of the shallow etched MMI [27]. Furthermore, 12 μm wide and 309 μm long deep etched multimode interferometer implementation was simulated by eigenmode expansion method for GaAs based tuneable dual-wavelength laser system at 785 nm [34]. Additionally, a multimode interferometer coupler was optimised for a Mach-Zehnder interferometer electo-optic switch at 1.55 μm. The simulation predicted that MMI performance is more sensitive for width variation than length variation and this was confirmed by experimental results [36]. Regarding splitting functionality, a tuneable power splitter was demonstrated by designing a bent GaAs based multimode interferometer with wide input waveguides (quasi-single-mode operation). Using beam propagation method, it was found that the splitting ratio has high fabrication tolerance [37]. Furthermore, 1 × N multimode interferometer beam splitter was studied at operating wavelength of 1.064 μm with splitting uniformity of ±4% [38] and a 1 × 2 multimode interferometer (24 μm wide × 1820 μm long) was simulated by beam propagation method for optical switching at 1.55 μm. [39].

Symmetrical Y-branches have been examined at 1.153 μm. It was found that there is positive correlation between radiation loss and the full branching angle and negative corelation between bend losses and etching depth [40]. For electro-optic modulation, a Mach-Zehnder interferometer was designed based on low loss symmetrical Y-branch at 1.3 μm with relatively large foot print (~ 1.8 mm length) [41]. Furthermore, a Y-branch dual wavelength laser was achieved by monolithically integrating a 500-1500 μm length Y-branch with DBR lasers and a curved output

coupler at 850 nm [42]. Also, a 5 µm wide mid-infrared Y-branch based Mach-Zehnder interferometer was designed for biosensing applications [43].

It was proven that GaAs based system is appropriate as an on-chip integration platform due to low propagation loss at 894 nm [44]. Also, it was demonstrated that various functionality photonics components could be integrated on a single GaAs chip at 1.55 µm [45]. Passive and active components were fabricated by single-step chemically assisted ion beam etching [46]. Moreover, it was proven that the silicon photonics style development can be applied to GaAs [47].

The prior work demonstrates the motivation for the development of an integrated photonic platform based on GaAs and also that it is feasible. This project focuses on studying and designing some passive components, namely, waveguides and splitters at ~1.3 µm from a GaAs/AlGaAs material system that is compatible with direct growth on silicon for 1.3 µm operation.

1.4   Thesis Structure

In this thesis the design and simulation of small footprint, passive photonic circuit components in a novel high confinement GaAs/AlGaAs structure is considered for operation at ~1.3 µm. The tolerance to unintended changes which may occur during fabrication is considered alongside the performance over a range of wavelengths. The analysis of the components was done by numerical methods of high accuracy that are appropriate even if the structure is operated close to the cut-off region [48]. This work will set up optimised small footprint designs for various GaAs/AlGaAs based library components that can be integrated with other active and passive components for different functionalities like data processing or biosensing.

In integrated photonics, power splitters are the main components for splitting optical signals. Power splitters can be designed according to two mechanisms: superposition of modes and optical field splitting. The first approach is applied in multimode interferometers while the second one is used in Y-branch splitters. As these devices are composed of simpler components, namely: waveguides, it is essential to investigate and understand them first. As the multimode interferometer is designed

using deep etched waveguides and Y-branch requires shallow etched waveguides, the two classes of waveguides are considered.

The simulation tools implement the physical concepts, solving the wave equation that is derived from Maxwell's equations. So, theoretical background about the wave equation and its solutions for 1D slab and 2D waveguides is covered in Chapter 2. Moreover, the basics of the computational schemes used to optimise and analyse the components are briefly described. Then, simulation setup and tools are explained. The fundamental components small cross-section ridge waveguides (deep etched) and large cross-section rib waveguides (shallow etched) are investigated in Chapters 3 and 4. Single mode operation is preferred for many applications and is a fundamental requirement to avoid radiation upon light guiding, and so the single mode condition is studied in both vertical and horizontal directions. The light experiences different cross-sections as it propagates through a multimode interferometer and a Y-branch. This cross-section mismatch increases the losses. Hence, the need for tapers appears. Thus, various tapered waveguides based on different design rules are analysed in Chapter 5. After making the investigation on the basic building blocks that are needed to design the splitters, Chapter 6 and 7 cover the optimisation and analysis of two different splitting functionality composite building block, multimode interferometer and Y-branch. For all components, geometrical variation and spectral responses are analysed.

Chapter 2 :

Theoretical Background and

Simulation

This chapter will cover some basics like the wave equation, methods of solving it, simulation setup and tools. The wave equation solution of a waveguide mode is derived for 1D a slab waveguide and generalised to a 2D waveguide. Various methods of solving the wave equation are briefly summarised. These methods are implemented in the simulation tool for different purposes. The way of building the model (structure, waveguide, device) and the setup of the software is explained.

2.1   Wave Equation

Waveguide modes are solutions of Maxwell's equations that are bound/confined to a waveguide core. A waveguide mode can be characterised by its eigenvalue (effective indices or propagation constants) and eigenvector (field profiles). First, we will solve Maxwell's equations for a one-dimensional waveguide, before looking at more practical two-dimensional waveguides. 1D waveguides are the simplest possible case, yet still have no analytical solution. However, solving for the 1D case will provide many insights into what makes a waveguide mode before looking at the numerical methods used to solve for 2D waveguide modes.

Starting from Maxwell's equations for a dielectric media where there are no free electric charges and no sources of the electric field ($\rho = 0$), Maxwell's equations are [12]

$$\left.\begin{aligned} \vec{\nabla} \cdot \vec{B} &= 0 \\ \vec{\nabla} \cdot \vec{D} &= 0 \\ \vec{\nabla} \times \vec{E} + \frac{\partial \vec{B}}{\partial t} &= 0 \\ \vec{\nabla} \times \vec{H} - \frac{\partial \vec{D}}{\partial t} &= 0 \end{aligned}\right\} \tag{2.1}$$

where $\vec{B}$ is the magnetic induction field vector, $\vec{D}$ is the displacement field vector, $\vec{E}$ is the electric field vector and $\vec{H}$ is the magnetic field vector. In addition to the four Maxwell's equations above, the constitutive or material equations are needed to relate $\vec{D}$ to $\vec{E}$ and $\vec{B}$ to $\vec{H}$. In general, these material equations can be complicated, involving the polarisation or magnetisation of materials, nonlinear terms and anisotropic effects, or even a history-dependent (hysteresis) behaviour. However, in linear, isotropic, and

homogenous materials such as the dielectrics that constitute most waveguides (and all the waveguides in this thesis), these material equations are simple linear relations:

$$\vec{D} = \varepsilon\varepsilon_0\vec{E} \tag{2.2}$$

$$\vec{B} = \mu\mu_0\vec{H} \tag{2.3}$$

The time dependence can be separated by using harmonic fields according to

$$\Psi(\vec{r}, t) = \vec{\Psi}(\vec{r})\exp(-i\omega t) \tag{2.4}$$

where the quantity Ψ is understood to be a stand-in for $\vec{B}, \vec{D}, \vec{H}$ or $\vec{E}$. Inserting the harmonic forms into the curls in (2.1),

$$\vec{\nabla} \times \vec{E} = -\frac{\partial\vec{B}}{\partial t} = i\omega\vec{B} = i\omega\mu_0\mu\vec{H} \tag{2.5}$$

$$\vec{\nabla} \times \vec{H} = \frac{\partial\vec{D}}{\partial t} = -i\omega\vec{D} = -i\omega\varepsilon_0\varepsilon\vec{E} \tag{2.6}$$

For a structure that is varying in y-direction and light propagates in z-direction, the change in x-direction is zero ($\frac{\partial}{\partial x} = 0$), hence equations (2.5) and (2.6) become:

$$\frac{\partial E_z}{\partial y} - \frac{\partial E_y}{\partial z} = i\omega\mu_0\mu H_x \tag{2.7 - A}$$

$$\frac{\partial E_x}{\partial z} - \frac{\partial E_z}{\partial x} = i\omega\mu_0\mu H_y \tag{2.7 - B}$$

$$\frac{\partial E_y}{\partial x} - \frac{\partial E_x}{\partial y} = i\omega\mu_0\mu H_z \tag{2.7 - C}$$

$$\frac{\partial H_z}{\partial y} - \frac{\partial H_y}{\partial z} = -i\omega\varepsilon_0\varepsilon E_x \tag{2.8 - A}$$

$$\frac{\partial H_x}{\partial z} - \frac{\partial H_z}{\partial x} = -i\omega\varepsilon_0\varepsilon E_y \tag{2.8 - B}$$

$$\frac{\partial H_y}{\partial x} - \frac{\partial H_x}{\partial y} = -i\omega\varepsilon_0\varepsilon E_z \tag{2.8 - C}$$

Independent solutions exist for each of two orthogonal polarisations: transverse electric (TE) and transverse magnetic (TM). The solution of TE mode can be found by taking second z derivative of equation (2.7-B) and second y derivative of equation

(2.7-C) and substituting the results into equation (2.8-A); the TE mode wave equation is obtained:

$$\frac{\partial^2 E_x}{\partial y^2} + \frac{\partial^2 E_x}{\partial z^2} + k^2 E_x = 0 \tag{2.9}$$

where $k^2 = \omega^2 \varepsilon_0 \mu_0 \varepsilon \mu$.

Hence, for the transverse electric (TE) polarisation, the electric and magnetic fields can be written as $\vec{E} = (E_x, 0, 0)$ and $\vec{H} = (0, H_y, H_z)$[1]. Equation (2.9) is a wave equation. Its solution is a transverse wave travelling in the y direction at a speed c/n, where $c = \frac{1}{\sqrt{\varepsilon_0 \mu_0}}$ and $n = \sqrt{\varepsilon \mu}$. The quantity c is the vacuum speed of light, and its prediction via Maxwell's equations was one of the great achievements of physics in the 19th century. The quantity n is usually called the refractive index of the material, and it describes the factor by which a material slows the light as the light is travelling through.

2.1.1   (1D) Slab Waveguide

In general, 1D waveguides could have many different layers with differing thicknesses and refractive indices. Here we will consider the simplest case of the slab or planar waveguide – a symmetric core of one material with refractive index n_2 and height H sandwiched between two semi-infinite cladding layers of refractive index n_1 (See Figure 2.1-A). Slab waveguides, although not truly 1D, can be treated this way as its width is much larger than its core height. So, for a homogenous structure, the spatial dependence of the refractive index varies only in direction perpendicular to the structure layers, $n = n(y)$. The refractive index of the structure has the profile (Figure 2.1-B):

$$n(y) = \begin{cases} n_1, & |y| > \dfrac{H}{2} \\ n_2, & |y| \leq \dfrac{H}{2} \end{cases} \tag{2.10}$$

---

[1] The other polarisation is the transverse magnetic (TM) will not be included it in the current analysis. However, the results from TE polarisation can be generalised to TM polarisation by substituting second z derivative of equation (2.8-B) and second y derivative of equation (2.8-C) and substituting the results into equation (2.7-A).

where n_1 and n_2 are the cladding and core refractive indices, respectively and H is the core height.
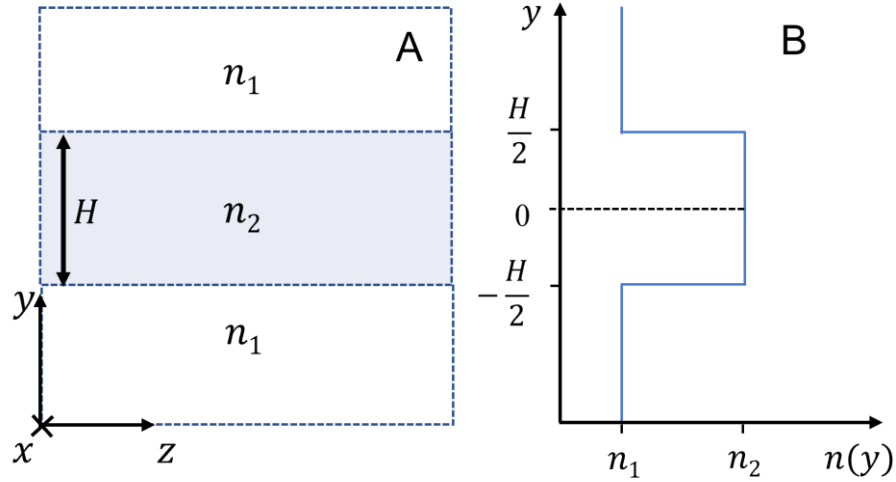
Figure 2.1: (A) Lateral view (yz plane) of symmetric 1D slab waveguide. *H* is the core height measured along y-axis and light propagates along z-axis. (B) Refractive index profile across the structure layers of slab waveguide.

This waveguide supports TE modes travelling in x-direction having the form:

$$E_x = E_{0,x}(y)\exp(ik_z z - i\omega t) \tag{2.11}$$

Noting that for a certain mode, the propagation constant k_z must be the same in the three layers to satisfy the continuity condition at the core-cladding interfaces. Substituting equation (2.11) into TE mode wave equation, equation (2.9), TE wave equation becomes:

$$\frac{\partial^2 E_{0,x}(y)}{\partial y^2} + k_y^2 E_{0,x}(y) = 0 \tag{2.12}$$

Where:

$$k_y^2 = k^2 - k_z^2 \tag{2.13}$$

The solution of equation (2.13) in the core has the form of sinusoidal wave (incident wave and its reflection) while in the claddings the solution takes the form of exponential decay of the outgoing waves transmitted through the core-cladding interface. Hence, the general solution is

$$E_{0,x} = \begin{cases} A\exp(-ik_{1,y}y) & y < -\dfrac{H}{2} \\ Bsin(k_{2,y}y) + Ccos(k_{2,y}y) & -\dfrac{H}{2} \le y \le +\dfrac{H}{2} \\ D\exp(+ik_{1,y}y) & y > +\dfrac{H}{2} \end{cases} \qquad (2.14)$$

The solutions need to be confined in the core and oscillate as sines and cosines which means $k_{2,y}$ is real. On the contrary, in the claddings the solutions are decaying exponentially then, $E_{0,x}$ has imaginary $k_{1,y}$.

The three layers, core and claddings, have the same propagation constant k_z but different k and k_y:

$$k_1^2 = k_z^2 + k_{1,y}^2 = \left(\frac{n_1\omega}{c}\right)^2 \qquad (2.15)$$

$$k_2^2 = k_z^2 + k_{2,y}^2 = \left(\frac{n_2\omega}{c}\right)^2 \qquad (2.16)$$

From equations (2.15) and (2.16), k_z is written in terms of k and k_y as:

$$k_z^2 = k_1^2 - k_{1,y}^2 = k_2^2 - k_{2,y}^2 = \left(\frac{n_{eff}\omega}{c}\right)^2 \qquad (2.17)$$

Equation (2.17) represents a circle of radius $\frac{n_{eff}\omega}{c}$ and n_{eff} is the effective refractive index of the waveguide mode where:

$$n_1 \le n_{eff} \le n_2 \qquad (2.18)$$

From equation $(2.7 - C)$, it is clear that H_z is the gradient of E_x. Hence,

$$H_{0,z} = -\frac{1}{i\omega\mu_0\mu} \begin{cases} -ik_{1,y}A\exp(-ik_{1,y}y) & y < -\dfrac{H}{2} \\ k_{2,y}Bsin(k_{2,y}y) + k_{2,y}Ccos(k_{2,y}y) & -\dfrac{H}{2} \le y \le +\dfrac{H}{2} \\ ik_{1,y}D\exp(+ik_{1,y}y) & y > +\dfrac{H}{2} \end{cases} \qquad (2.19)$$

E_x and H_z are the tangential components which are needed to be continuous at the core-cladding interface, i.e., at $z = \pm\frac{H}{2}$:

$$E_{0,x}(\pm\frac{H}{2})_- = E_{0,x}(\pm\frac{H}{2})_+ \qquad (2.20)$$

$$H_{0,z}(\pm\frac{H}{2})_- = H_{0,z}(\pm\frac{H}{2})_+ \tag{2.21}$$

These two conditions are satisfied for the two types of modes: even (or symmetric) and odd (or antisymmetric) modes. For even modes, $A = D$ and $B = 0$ while for odd modes $A = -D$ and $C = 0$.

Now, putting

$$u = \frac{k_{2,y}H}{2} \tag{2.22}$$

$$v = \frac{-ik_{1,y}H}{2} \tag{2.23}$$

with

$$u^2 + v^2 = \frac{\omega^2 H^2}{4c^2}(n_2^2 - n_1^2) \tag{2.24}$$

Equation (2.24) represents a circle of radius R (where $R^2 = \frac{\omega^2 H^2}{4c^2}(n_2^2 - n_1^2)$) depends on the incident wave frequency, waveguide height and the structure's refractive index contrast. By substituting equations (2.22) and (2.23) into equations (2.14) and (2.19) and applying boundary conditions, equations (2.20) and (2.21), the following eigenvalue equations are obtained. For even modes:

$$v = u \tan u \tag{2.25}$$

And for odd modes:

$$v = -u \cot u \tag{2.26}$$

To find the modes that are supported by a certain structure, equations (2.25) and (2.26) together with the equation of the circle, equation (2.24), are needed to be solved graphically to find the intercepts of eigenvalues with the radius of the circle. The intercepts represent number of supported modes corresponds to different values of incident frequency, structure (n_1 and n_2) and core height [49]. To find the supported mode graphically, equations (2.24) to (2.26) are represented in Figure 2.2: the green line represent the symmetric modes, the blue one represent the antisymmetric mode and the red curve represents a semicircle whose radius is given by equation (2.24). The allowed solutions are the points of intercepts between the eigenvalues and the

semicircle. as the radius increases more modes are supported. Looking at equation (2.24), it is noticeable that the radius depends on both the structure (step index, $n_2^2 - n_1^2$, and core height) and the incident light frequency ω. So, if any of these three parameter changes, the radius will follow that change. However, since the structure and the frequency were chosen, the single mode condition is obtained by choosing a suitable core height. In 1D, the single mode region can be found analytically. It is when the red circle has a radius that touches the green line. Thus, ~ 0.44 µm can be proposed as an optimum core height with fabrication tolerance of ~ 0.20 µm. These solutions are obtained for the structure of $n_1 = 3.4088$, $n_2 = 3.1967$, wavelength= 1.3 µm and waveguide height of 1 µm.
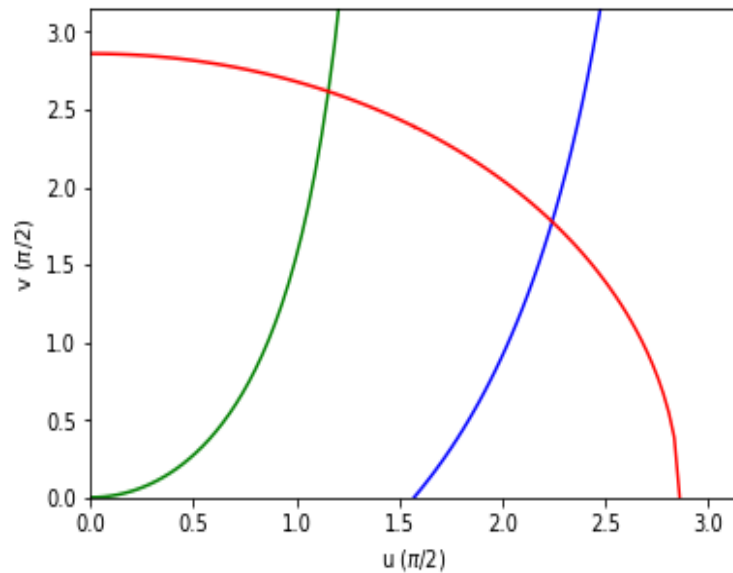
Figure 2.2: Graphical solution of the eigenvalue equation for GaAs/AlGaAs slab waveguide of core height of 1 µm and wavelength of 1.3 µm calculated by applying equations (2.24) to (2.26).

A simplified analysis of 1D slab waveguide has been covered to understand how modes properties are related to waveguide structure and geometry. In the next section, this analysis will be generalized to 2D waveguides.

2.1.2   2D Waveguide

The 1D slab waveguides have no practical use due to lack of lateral confinement but they are a first step to understand and analyse waveguides. They need to be "upgraded" to offer confinement in two directions so 2D waveguides are realised. 2D

or rectangular waveguides are one of the photonic integrated circuits basic building blocks where confinement is in two directions (Figure 2.1Figure 2.3-A). They are appropriate for on-chip planar structure processes up to few centimetre lengths such as circuits interconnection. Moreover, understanding the mode properties is essential to find the physical concept of controlling signals through devices of higher degree of complicity, composite building blocks, like power splitter or filters.
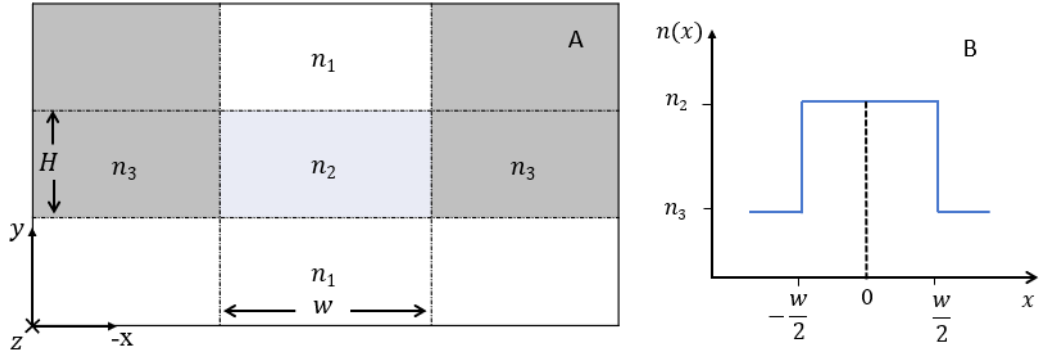
Figure 2.3: (A) 2D waveguide of cross-section (xy plane). H and w are the core height and width, respectively. Gray parts represent etched area. (B) Refractive index profile across waveguide width along x-axis where n_2 and n_3 are core and cover refractive indices, respectively with $n_2 > n_3$ to provide the optical confinement.

Figure 2.3-A illustrates symmetrical 2D waveguide cross-section structures where H is the core height and w is the width. The refractive index is varying in both direction x and y, $n = n(x, y)$, and $n_2 > n_1$ and n_3 so that the light is confined in both directions, vertical and horizontal. For simplicity, the confinement is assumed high enough that the fields in the corners are negligible. Now, taking into consideration the same conditions as in the 1D slab waveguide treatment, the harmonic field behaviour, equation (2.4), in two dimensions can be written as

$$\vec{\Psi}(\vec{r}, t) = \vec{X}(\vec{x})\vec{Y}(y)exp(-i\omega t) \qquad (2.27)$$

Where $\vec{X}(x)$ and $\vec{Y}(y)$ are the modal field in x and y direction (as seen in Figure 2.4) The vertical and transverse solutions of the wave equation across the waveguide can be written in analogy to the solutions obtained for the 1D slab waveguide $E_{0,x}$ (equation 2.14) [50].

	$\exp(+ik_{1,y}y)$ $sin(k_{1,x}x) + cos(k_{1,x}x)$	
$\exp(-ik_{3,x}x)$ $sin(k_{3,y}y) + cos(k_{3,y}y)$	$sin(k_{2,y}y) + cos(k_{2,y}y)$ $sin(k_{2,x}x) + cos(k_{2,x}x)$	$\exp(+ik_{3,x}x)$ $sin(k_{3,y}y) + cos(k_{3,y}y)$
	$\exp(-ik_{1,y}y)$ $sin(k_{1,x}x) + cos(k_{1,x}x)$	

Figure 2.4: Mode field across a symmetric rectangular waveguide in Figure 2.3-A.

2.1.3   Methods of Solving the Wave Equation

There are various methods to study mode formation or propagation through guiding structures (waveguides or devices). Some of them are analytical and some are numerical. Analytical approaches are approximations and restricted to simple structures like 1D slab waveguides due to accuracy limitation when applied to complicated photonic devices [51]. On the other hand, the numerical methods, based on both coding and software are of good accuracy to treat 2D waveguides or devices of higher complexity. In this section, the techniques used in this research will be explained briefly. Some of these methods are semi-analytical like the effective index method that was used to treat 1D slab waveguides. Other approaches are finite difference and film mode matching that were used to study 2D ridge and rib waveguides. For the 3D investigation where propagation is included in the calculation, eigenmode expansion method was applied together with the finite difference method to optimise the devices. Both 1D and 2D waveguides were investigated by Fimmwave (version 7.2 and 7.3) and the 3D calculations were done by Fimmprop (version 7.2 and 7.3). Parameters like core height, waveguide width, device length and shape were scanned using a Python code as an application programable interface to control the Photon Design software.

2.1.3.1   Effective Index Method

The effective index method (EIM) is a semi-analytical approximation that includes treating the 2D waveguides in two steps: divide the structure into a set of

slices and apply the 1D slab waveguide analysis in the y direction to find an effective index, $n_{eff}(x)$, for each slice, then the new 1D slab waveguide is treated in terms of $n_{eff_i}(x)$ and analysed as a 1D slab waveguide in the other direction, x [52]. The effective index of the central slice, n_{eff_2}, represent the core refractive index in the second step [2], [53]. The waveguide in Figure 2.5-A is approximated as seen in Figure 2.5-B.
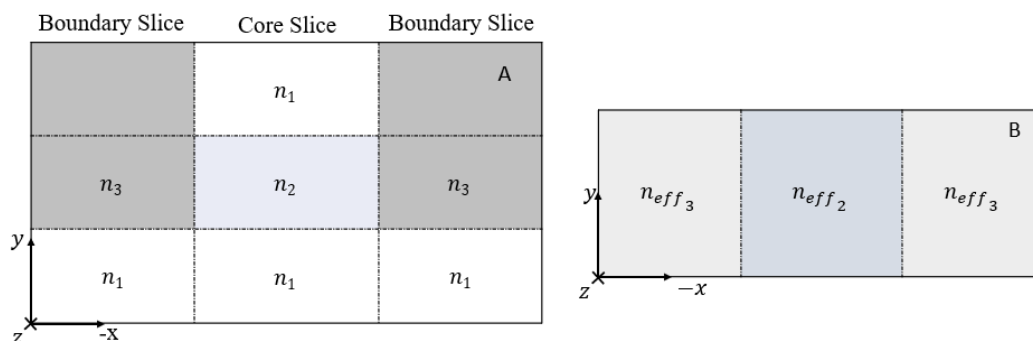
Figure 2.5: (A) 2D waveguide slices. Each slice is invariant along x-axis and contains three layers along y-axis. (B) Effective 1D slab waveguide of (A) consists of three effective slices that are invariant in both x and y directions.

2.1.3.2   Film Mode Matching Method

Film mode matching (FMM) treats a waveguide by dividing it into a series of vertical slices, i. Each slice is considered as a planar 1D slab waveguide where the refractive index, n is invariant in the x direction. The wave equation (2.28) is applicable in all points enclosed in each slice i.

$$\frac{\partial^2 \Psi}{\partial x^2} + \frac{\partial^2 \Psi}{\partial y^2} + k_{i,x}^2 \Psi = 0 \tag{2.28}$$

where $k_{i,x}$ is the wave vector in the slice i. The modal field in the waveguide is expressed by a linear combination (equation 2.29) of the vertical 1D modes of the slices. Taking in consideration the field continuity and their normal derivatives at each cell interfaces, the mode profile in each rectangle takes the form [54]:

$$\Psi(x,y) = \sum_{i=1}^{N} u_i \Psi_i(x,y) \tag{2.29}$$

Where Ψ_i represents 1D fields profiles, u_i is the mode amplitude an N is the number of 1D mode in a slice i. The cross-section of a waveguide treated by FMM is presented in Figure 2.6 [55].
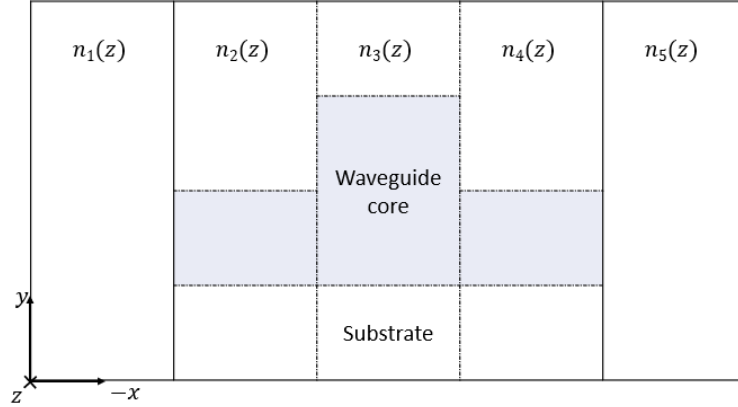
Figure 2.6: Cross-section of i slices waveguide. Each slice is invariant in x-direction and composes of several layers in y-direction.

2.1.3.3   Finite Difference Method

Finite difference method (FDM) is based on solving the wave equation in a waveguide using the finite difference approximation where the second derivatives for 2D waveguide are defined by equations (2.30) and (2.31). Figure 2.7 shows 2D finite difference scheme [56], [57].

$$\frac{\partial^2 \Psi}{\partial x^2} = \frac{\Psi_{i+1,j} - 2\Psi_{i,j} + \Psi_{i-1,j}}{\Delta x^2} \tag{2.30}$$

$$\frac{\partial^2 \Psi}{\partial y^2} = \frac{\Psi_{i,j+1} - 2\Psi_{i,j} + \Psi_{i,j-1}}{\Delta y^2} \tag{2.31}$$
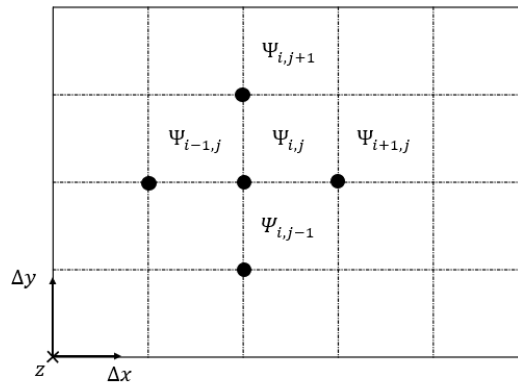
Figure 2.7: 2D finite difference discretisation along x and y axes using value of $\Psi(x)$ and $\Psi(y)$.

Eigenvalue matrix equations are generated by discretising the waveguide into a set of cells by choosing convenient number of mesh points. Applying the boundary conditions, the wave equation can be solved and hence the modes propagation constants and profiles are obtained with accuracy altered by mesh size (grid resolution), order of approximation (order of accuracy) and electromagnetic field nature (scalar, semi-vectorial or vectorial) [48].

2.1.3.4   Eigenmode Expansion Method

As an input field, $\Psi(x, y, z = 0)$, propagates in a certain direction, $+z$, it is expressed by the wave equation solutions along a waveguide. The behaviour of the input is expressed as a linear expansion of eigenfunctions and amplitudes of incident modes (travelling in $+z$) and reflected modes (travelling in $-z$) as [58]:

$$\Psi(x, y, z = 0) = \sum_{i=1}^{N} \left(u_i^f \Psi_i(x, y) \exp(ik_{i,z}z) + u_i^b \Psi_i(x, y) \exp(-ik_{i,z}z) \right) \quad (2.32)$$

Where $\Psi_i(x, y)$ is mode i profile, u_i^f and u_i^b are forward and backward modes amplitudes, respectively. Knowing that all modes are orthogonal,

$$\int_{-\infty}^{\infty} \Psi_i(x, y, z) \Psi_j^*(x, y, z) dz = 0 \text{ for } i \neq j \quad (2.33)$$

a mode amplitude u_i can be found from the relation

$$u_i = \int_{-\infty}^{\infty} \Psi_i(x, y, z) \Psi_i^*(x, y, z) dz \quad (2.34)$$
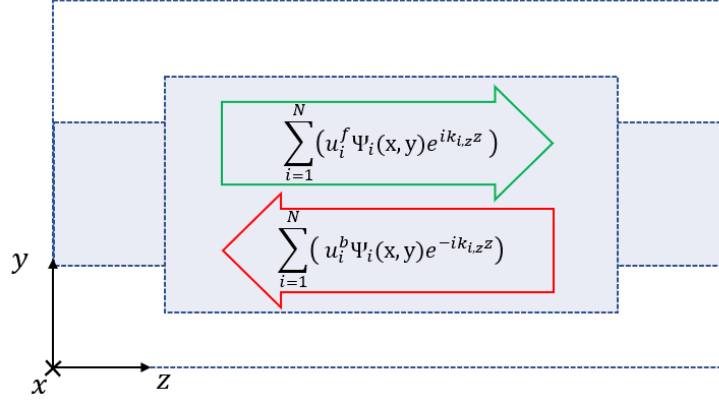
Figure 2.8: Forward and backward modes in propagation direction along z-direction over a waveguide length.

2.2 Simulation

Photonic component development is a long process includes design, fabrication and characterisation. Design stage is of high importance since it can produce a lot of proposed versions of the same component and allow to test the performance by altering some physical quantities. Therefore, simulation tools play an important role in optimising and studying various components and analyse their response under several conditions before they approved for fabrication. Hence, fabrication time and resources are conserved.

The first step in developing photonic waveguides and devices is designing and optimising them according to the functionality and fabrication adequacy. Then, based on evaluating the tolerance and performance under various circumstances, the decision of fabricating a certain component is taken. After that, if the design is applicable and the fabrication process is set, then the component can be manufactured repeatedly without the need for repeated optimisation, tolerances tests or resetting fabrication processes [57]. Once the design of a certain component is approved upon characterisation, it can be added to a components library that designers can refer to [11]. Hence, time, effort and resources can be saved.

The main design steps followed in this thesis are:

1. The refractive indices of both GaAs and AlGaAs (Figure 2.9) as function of the wavelength at 300 K[2] were taken into consideration according to information provided in [59].

2. Building the layer of the structure as a 1D slab waveguide.

3. Extending the slab waveguide to 2D waveguide by applying the etching and using BCB [60] as a planarisation layer (cover).

4. Using the optimised 2D waveguide to design and optimise higher level components.
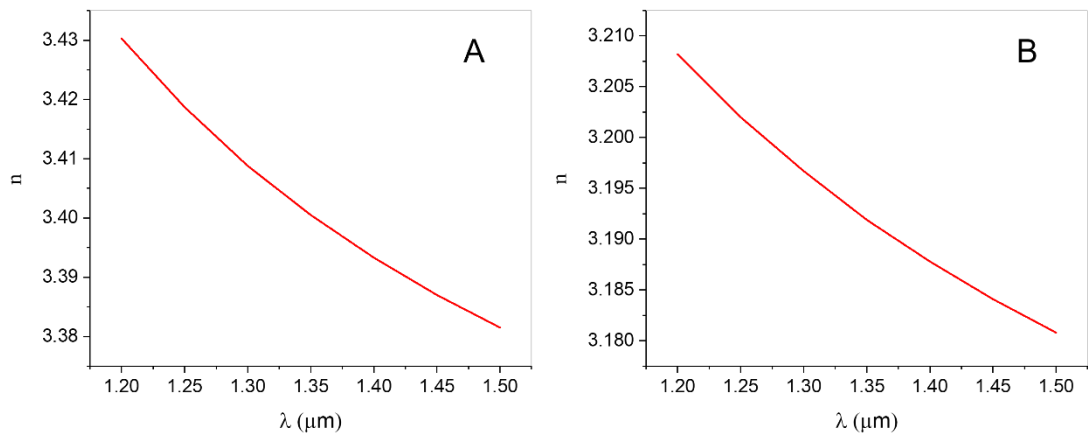
Figure 2.9: (A) GaAs and (B) Al$_{0.5}$Ga$_{0.5}$As refractive indices as function of operating wavelength at 300 K.

The simulation was carried out using Fimmwave, for 1D and 2D calculations, and its extended module Fimmprop, for light propagating or 3D calculations [61]. For each step, the software calculation window and solver parameters convergences need to be checked. In the following sections, details on software optimisation will be discussed.

---

[2] The refractive index is temperature dependent according to $dn = \frac{dn}{d\lambda}\Delta\lambda + \frac{dn}{dT}\Delta T$ for GaAs [120] and $n(x,\lambda,T) = \sqrt{10.906 - 2.92x + \frac{0.97501}{\lambda^2 + C} - 0.002467(1.41x + 1)\lambda^2 + [(T - 26°C) \times (2.04 - 0.3x) \times 10^{-4}/°C]}$ for Al$_x$Ga$_{1-x}$As and C depends on x [121].

2.2.4   Simulation Setup

Any numerical simulation or calculation will contain within it "non-physical" calculational parameters such as the resolution of the calculational grid, or how far away from the structure under test the calculations boundaries are set. No physical value should depend on any of these computational parameters, but there is usually a trade-off between computational resources (time and memory) and accuracy. As an example, take the resolution of the computational grid – finer grids will in general give more accurate results, but take longer and use more memory. In this thesis, accuracy is usually most important, as the computational resources required of our simulations are modest. Therefore, the accuracy benchmark is chosen based on the most accurate value of a physical parameter, like the effective index, by testing the convergence of the calculation under computational parameters change like mesh size. The benchmark accuracy keeps in mind the accuracy limitations imposed by some of the assumptions, making calculating any more accurately pointless. Convergence testing plots the physical result (e.g., the effective index of a mode) vs. the computational parameter (e.g., the resolution) to find the values for which the calculation is converged – i.e., the result is close to the true one with little or no dependence on the computational parameter.

2.2.4.1   Optimisation of Calculation Window

Choosing an appropriate window size is an essential step before performing simulations. Too small a window size will disrupt the mode profile and hence the results accuracy and too big a window size means too long a calculation time with no higher accuracy. So, choosing an optimal window size will save time and guarantee high accuracy. For that, the upper and lower claddings thicknesses need to be checked to ensure that mode profiles are not affected by vertical boundaries. In addition, the same step is needed in the horizontal direction by testing right and left slices that surrounding the core slice for the 2D waveguide [62].

2.2.4.2   Solver Parameters Optimisation

Each technique of solving the wave equation has parameters that specify the type and density of discretisation and hence control the accuracy. The number of modes is a common parameter that is set before testing the other parameters. On the waveguide level in Fimmwave, the modes effective indices convergence is tested. For a higher level of work, propagating-dependence simulation, on Fimmprop, the convergence of output power is tested.

2.2.4.2.1   Maximum   Number   of   Calculation   Modes   Convergence

The first step in optimizing the solvers is including a sufficient number of calculation modes in the simulation. This step is done by increasing the number of calculation modes until the results converge. This step will be presented in Chapters 3 and 4 when the work is done on waveguides. In addition, it will be discussed in Chapters 5 to 7 when the cross-section is propagation dependent, namely: for tapers and splitters.

2.2.4.2.2   Film Mode Matching Solver (FMM) Convergence

The mode matching solver accuracy is controlled by the number of 1D modes per slice. The higher the number of 1D modes, the higher the accuracy. This parameter cannot be increased without taking the calculation time into consideration as this is extended as the 1D mode number is getting bigger.

2.2.4.2.3   Finite Difference Solver (FDM) Convergence

Number of mesh cells along vertical and horizonal directions controls the density of grid points over the waveguide cross-section which alters the accuracy. Like the 1D mode parameter, bigger number of mesh cells means longer calculation time. As number of mesh cells changes, the effective indices convergence in the 2D waveguides and the output power in devices will be checked.

2.2.4.3   Taper Algorithm Parameters

For waveguides that vary in the propagation direction, like tapers and bend waveguides, taper discretisation convergence tests are important. The taper algorithm determines the discretisation size and density based on how fast the modes evolve along the taper. Stronger changes in the modes means finer discretisation is required. The taper algorithm is controlled by:

1- How finely the evolution of the modes should be followed and
2- The smallest fraction of the taper length that the taper algorithm is limited to in the discretisation.

In this chapter, basic information about the waveguide mathematical analysis was presented. First, the wave equation was derived and solved for 1D slab waveguide and then applied to 2D waveguide. Then, some methods of solving Maxwell's Equations in waveguides were summarised. Finally, the simulation method was briefly described along with software optimisation. In the next chapter, 1D slab and 2D ridge waveguides are investigated to find the single mode conditions and study the tolerances.

Chapter 3 :

Small Cross-Section Ridge Waveguides

At its most basic, a waveguide is simply a channel which transports or guides light. This guiding function is especially important in photonic integrated circuits, where the performance of the waveguide can determine the performance and footprint (and therefore economics) of the whole chip or device. As well as a basic guiding functions, waveguides can be considered as a basic building block of generic photonic integration, which can be used as component parts of larger and more complex devices. Waveguides are designed based on the wavelengths being transported and/or their intended function in a device. Careful engineering of a waveguide's size and shape can control, for example, the effective refractive index of the waveguide modes and the number of modes available. Waveguides can be chosen to be single mode or multimode, straight or bent, tapered or of constant width. This chapter focuses on studying 1D slab and ridge GaAs/AlGaAs waveguide and finding a single mode height (for slab waveguide) and width (for ridge waveguide) at a wavelength ~ 1.3 μm. As well as designing/engineering waveguides for the properties and applications, it is necessary to consider how reproducibly they can be fabricated and what range of wavelengths they will need to support with reasonable performance. In this chapter, I will study performance as vary waveguide parameters like waveguide width, etching level and core height are varied, to understand how tolerant they are to unexpected variations in fabrication and also vary operating wavelength, and to study the range over which they can be used.

3.1　Methodology

The parameters of the waveguides used in the calculation are shown in Figure 3.1 with refractive index values corresponding to ~1.3 μm wavelength (see Figures 2.9 in chapter 2), where it is assumed that the steam oxidation of $Al_{0.98}Ga_{0.02}As$ results in Al_2O_3 as reported in [63], [64]. The convergence of the fundamental mode's effective index was checked with respect to the calculation window size, allowing a suitable trade-off between accuracy and resource efficiency.

The height was checked on the 1D slab waveguide level by scanning the upper and lower cladding heights. Following this the deep etched 2D ridge waveguide was built from three identical 1D slab waveguides with etching applied on the boundary slices (Figure 3.2). The width of the boundary slices was checked to find the

convergence [1]. At this point solver parameters were tested to obtain sufficient accuracy. At this stage, the simulation can be done to record the modes characteristics as the waveguide core height or width increases to find the single mode conditions and to study the tolerances in waveguide dimensions. The effective index solver was used to study the vertical modes in the 1D slab waveguide. The single mode width cut-off of the ridge waveguide was found using a finite difference solver and then by using the film mode-matching solver to make sure that same result is obtained using different solvers. Once this is established, the other ridge waveguide investigations were done by the finite difference solver as it is faster. It is also used to study the devices in the following chapters 5-7.
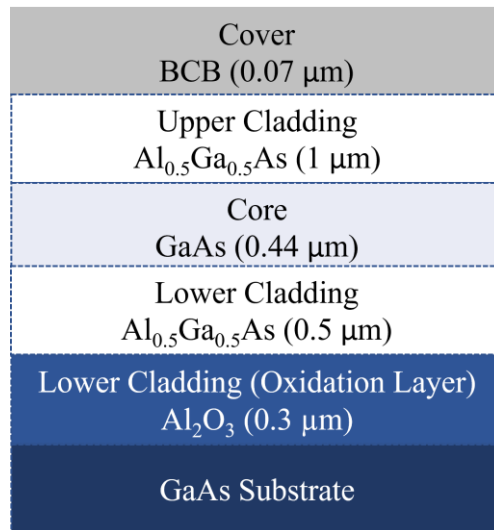
Figure 3.1: 1D slab waveguide structure layers and heights along y-direction. The compositions and heights are optimised to be compatible with the laser structure and to confine the light.
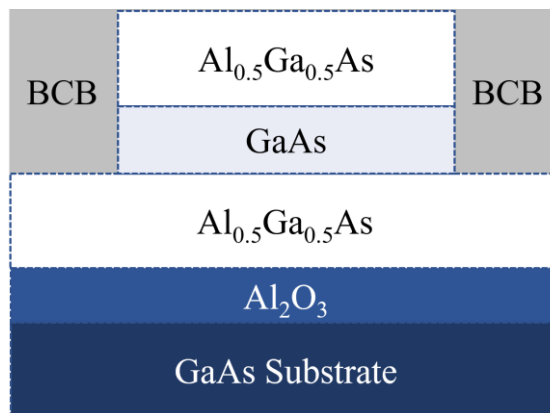
Figure 3.2: 2D ridge waveguide slices. The central slice contains the core and the boundaries are the parts where the etching is applied and covered by BCB for planarisation.

3.1.1 Calculation Window Height Optimisation

On this level of work 1D, the mode list was generated using the effective index solver to investigate mode properties. First, the GaAs substrate is excluded from the simulation because with the existence of the substrate, calculation time is increased and many modes existing entirely within the substrate are calculated, which make it difficult to identify the much smaller number of modes in the required waveguide core. After that, the top and bottom calculation boundaries were inspected for the purpose of convergence tests. Because the structure is not symmetrical in the vertical direction (across the structure layers), the calculation height optimisation was done in two steps. First, the effective index of the TE_{00} mode was scanned as the upper $Al_{0.5}Ga_{0.5}As$ height was varied at a fixed lower $Al_{0.5}Ga_{0.5}As$ height value of 0.5 µm (Figure 3.3-A). After that, this step was repeated, as presented in Figure 3.3-B, to find the convergence of the lower $Al_{0.5}Ga_{0.5}As$ at constant upper $Al_{0.5}Ga_{0.5}As$ height. Hence, the vertical boundaries were set so that the upper and lower $Al_{0.5}Ga_{0.5}As$ height values are 1 µm and 0.5 µm, respectively. So, these two layers heights and Al amounts are chosen to:

1- Make the whole structure have suitable confinement,

2- Be as small as possible to avoid cracks (when grown on silicon) and

3- Be suitable for integration with laser and Si-based devices.
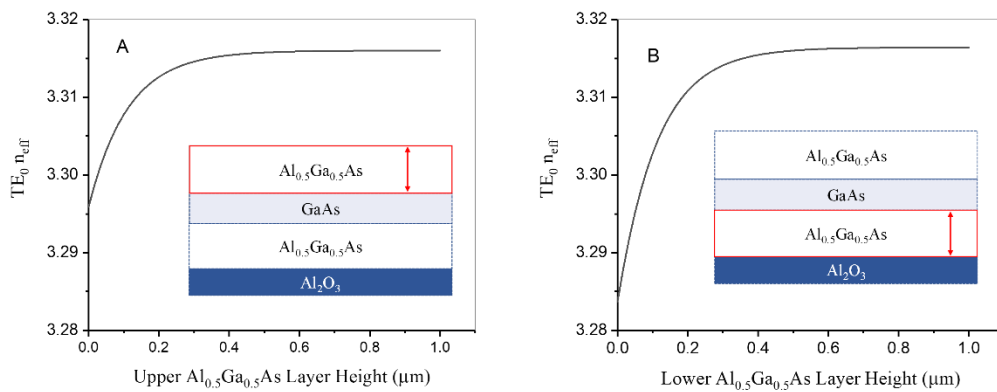
Figure 3.3: (A) Upper $Al_{0.5}Ga_{0.5}As$ convergence test at lower $Al_{0.5}Ga_{0.5}As$ height=0.5 µm. (B) Lower $Al_{0.5}Ga_{0.5}As$ convergence test at upper $Al_{0.5}Ga_{0.5}As$ height=1 µm. The calculation is performed for GaAs/AlGaAs slab waveguide using Fimmwave IEM solver in y-direction (1D calculation).

After performing the height convergence test, the field profile of the TE_{00} mode was checked to ensure it exponentially decays towards zero at the boundaries. The electric field at the top and bottom boundaries is 0.3% and 0.1% of its maximum value which means more than 99% of the electric field is included in the calculation window. Figure 3.4 displays the TE_{00} mode electric field profile across the structure layers. It can be seen that the fundamental mode is exponentially decaying to zero through the cladding layers and not being disrupted by the calculation top and bottom boundaries. Hence, keeping the proposed values of the upper and lower claddings height is a good decision. The calculation steps in the window height setup are summarised in Figure 3.5.
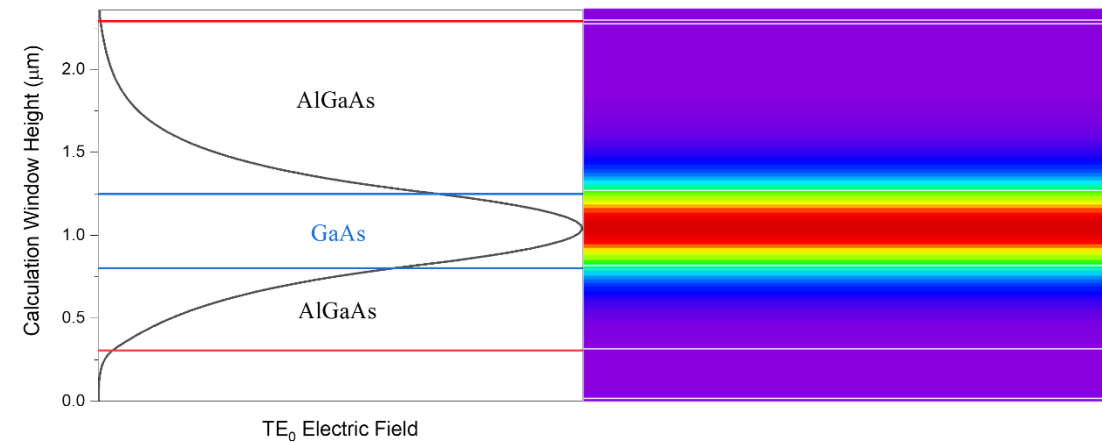
Figure 3.4: GaAs/AlGaAs slab waveguide TE_{00} electric field and intensity profiles across calculation window height in y-direction calculated by Fimmwave EIM solver.

1 • Build the structure layers (single slice): Substrate, lower cladding, core, upper cladding and cover.

2 • Exclude the substrate since its existence increase the calculation and analysis time.

3 • Test the convergence of TE_{00} effective index under upper cladding height variation at fixed lower cladding height.

4 • Test the convergence of TE_{00} effective index under lower cladding height variation at upper cladding height obtained from 3.

5 • Check the TE_{00} mode profile to ensure smooth decay toward zero at the top and bottom boundaries.

Figure 3.5: 1D calculation window height optimisation steps.

3.1.2 Calculation Window Width Optimisation

For the simulation in 2D, the calculation width needs to be set to ensure convergence similar to what was done in the slab waveguide. The horizontal size of the calculation window was optimised (by tracking the effective index convergence) to ensure that the results were not disrupted by the calculation boundaries. So, the effective index of the fundamental TE_{00} mode was recorded as the calculation window width is increased. The horizontal axis in Figure 3.6-A represents the distance between the central, right and left slices' edges, which includes the core, to the right and left boundaries of the calculation window. It can be noticed that the calculation boundaries can be placed at horizontal distance of 0.4 µm from the core boundaries as this result in relative error of smaller than 0.005% when compared with a simulation of much larger boundary (I used 1 µm in the comparison). This calculation was performed on a single step for both sides, left and right, due to structure horizontal symmetry. According to Figure 3.6-A, the side slices size was chosen to be 0.4 µm. To ensure that this value is sufficient, the TE_{00} mode electric field profile is plotted versus the calculation window width as seen in Figure 3.6-B. This shows the evanescent field

decaying smoothly at the calculation horizontal boundaries without being disrupted. However, it is apparent that there is significant discontinuity in the TE_{00} mode field at the core boundaries. This phenomenon is caused by the high step index as well as the electric boundary at the edge between the core and etched area that is covered by BCB (n=1.544) after etching [65].
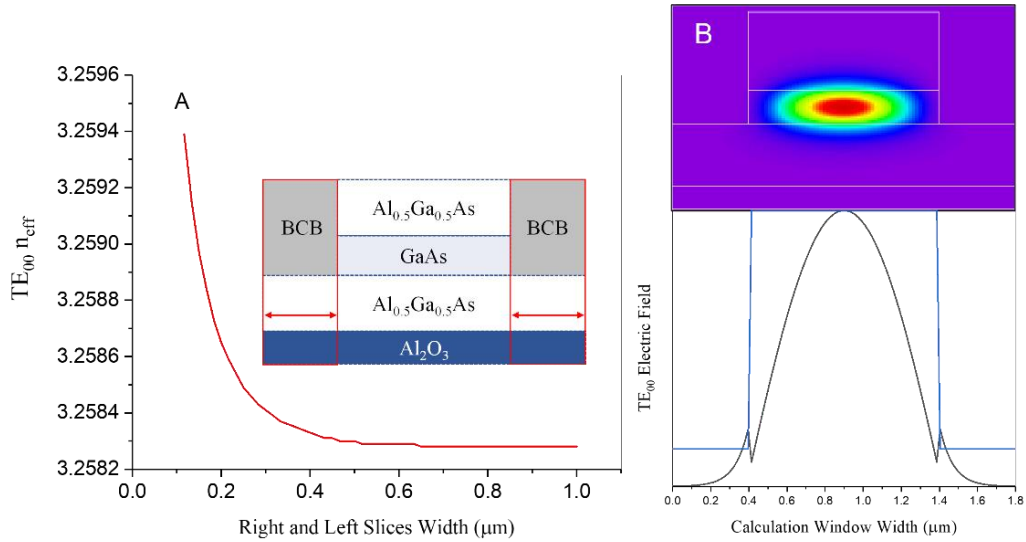
Figure 3.6: (A) Calculation window width convergence test for GaAs/AlGaAs 2D ridge waveguide. TE_{00} mode effective index variation as calculation boundaries get further from the core slice. (B) Electric field and intensity profiles of TE_{00} mode across the calculation window width in x-direction as obtained by FDM solver implemented in Fimmwave (2D calculation).

3.1.3   Solvers Optimisation

The parameters used in the mode solver affect the accuracy of the results that are obtained So, the higher (or finer) parameter value (or size), the higher accuracy. However, the parameter value (or size) cannot be chosen independently since too high (or too fine) parameter values increases computational resources which depend on the machine efficiency and number of tasks being processed while the calculation is taking place. For example, the higher the number of maximum calculation modes (or 1D modes) increases the accuracy and the calculation time and needs bigger memory to perform the simulation. The same is said when the parameter is the grid size (number of cells along a calculation direction). The finer the grid size, the higher resource requirements.

3.1.3.1   Finite Difference Method Solver (FDM)

The accuracy obtained when using a finite difference method solver (FDM) depends on the number of mesh cells across the calculation window cross-section. The TE$_{00}$ mode effective index, $n_{eff}(number\ of\ cells)$, was recorded over number of cells 10 to 300 (Figure 3.7-A). Then $n_{eff}(300)$ was used as reference point to calculate the relative error, Δn_{eff}. This parameter value was chosen as a compromise between sufficient accuracy and accepted calculation time. As an example, relative error of $\Delta n_{eff} = \sim 10^{-5}\%$ corresponds to more than 240 cells and calculation time =24 s/calculation or longer (Figure 3.7-B).
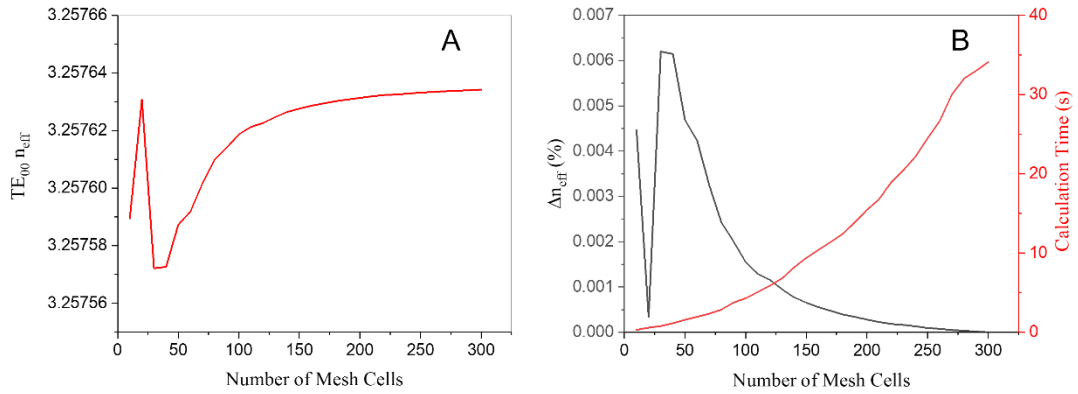
Figure 3.7: (A) Fimmwave FDM solver parameter, number of mesh cells, convergence test for GaAs/AlGaAs 2D ridge waveguide. (B) Relative error and calculation time as function of number of mesh cells across the calculation window cross-section.

3.1.3.2   Film Mode Matching Method Solver (FMM)

The number of 1D modes in each slice of the waveguide is the film mode matching method solver (FMM) parameter. As seen in Figure 3.8-A, $n_{eff}(1D\ modes)$ was scanned for 1D mode values from 10 to 200 and then the relative error, Δn_{eff}, was calculated and presented together with calculation time in Figure 3.8-B. For $\Delta n_{eff} = \sim 10^{-5}$, the ccalculation time is more than 120 s/calculation.
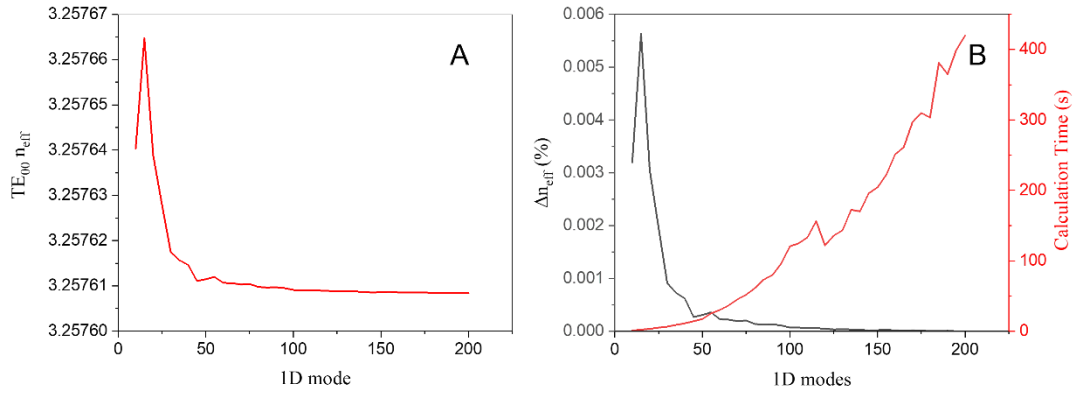
Figure 3.8: (A) Fimmwave FMM solver parameter, 1D mode, convergence test for GaAs/AlGaAs 2D ridge waveguide. (B) Relative error and calculation time as function of number 1D modes.

In this section both the calculation window size and parameters to optimise the solver were investigated to set up the software to perform the simulations. In the next section, I will study waveguides modes in both vertical and horizontal directions to find single mode cut-off height and width.

3.2   Single Mode Cut-Off

The single mode cut-off was studied in two independent steps. First, the single mode cut-off height was found for a 1D slab waveguide. Then the single mode cut-off width was obtained for the 2D ridge waveguide.

3.2.4   Single Mode Height

The number of supported modes as a function of the core height was studied using a Fimmwave [61] solver, effective index method (EIM) solver . The single mode cut-off was determined by scanning the height of the core as in Figure 3.9. The structure starts confining modes at effective index value of 3.20 (just above the cladding refractive index [28]) and modes of effective index value less than 3.20 are not supported by this structure and only leaky modes can propagate [31]. The fundamental mode is supported by core height starting from 0.1 μm and the first higher mode becomes guided for core height larger than 0.6 μm. Thus, with a height

(~0.44 μm) a fabrication tolerance (variation in the height achieved) of ± 0.20 μ*m* is possible without guiding the second mode.
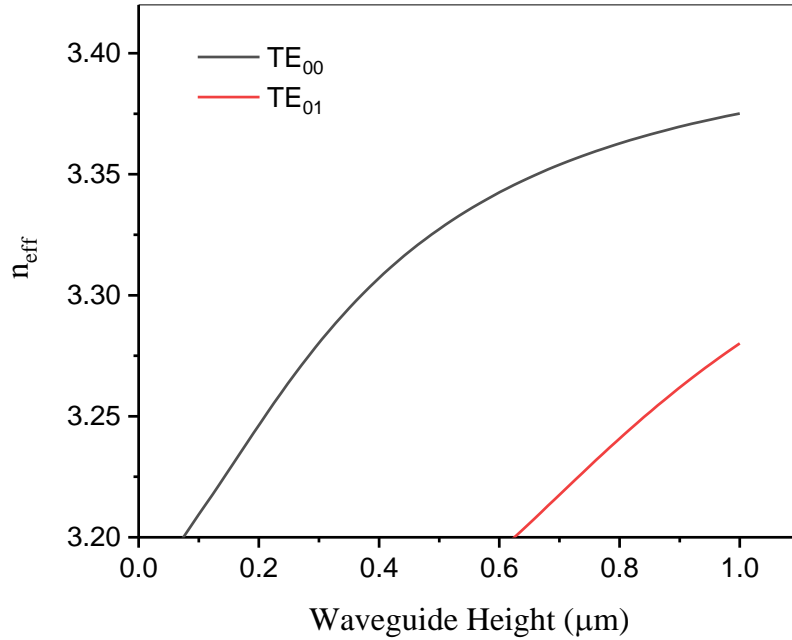
Figure 3.9: Effective indices of the of TE₀₀ and TE₀₁ as core height increases up to 1 μm at wavelength of ~1.3 μm using EIM for the GaAs/AlGaAs 1D slab waveguide shown in Figure 3.1.

3.2.5 Single Mode Width

Two solvers were used to find the single mode cut-off width (FDM and FMM) after optimising the calculation width and performing the convergence tests.

3.2.5.1 Finite Difference Method Solver (FDM)

Figure 3.10 shows TE like mode effective indices evolution as the width of the waveguide increases. According to this graph, the single mode cut-off width is located at 1.42 μm. This result was generated using the FDM solver with relative error $\sim 10^{-4}$%.
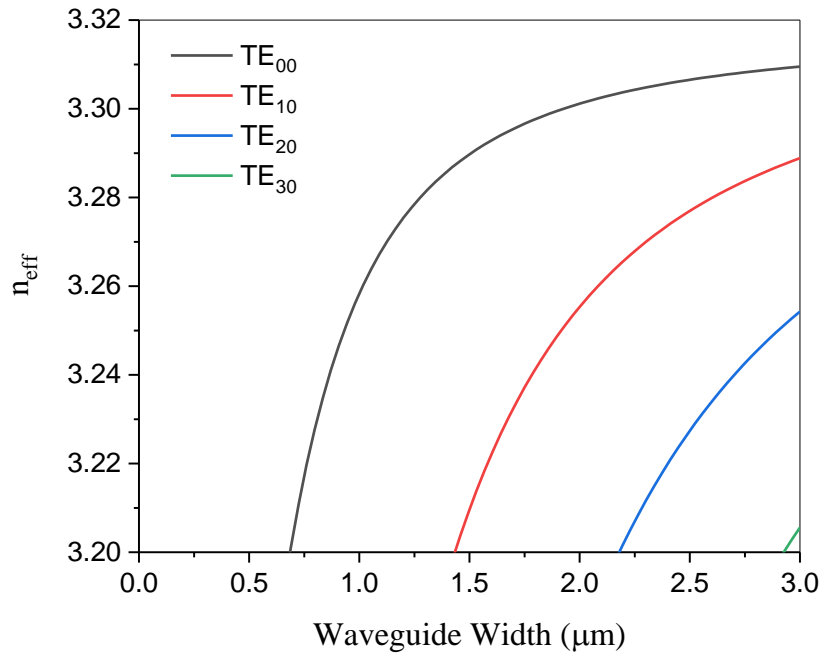
Figure 3.10: Effective indices of supported modes by 2D ridge waveguide in Figure 3.2 of 0.44 μm core height and width up to 3 μm at wavelength of ~1.3 μm calculated using Fimmwave FDM solver with relative error $\sim 10^{-4}$%.

3.2.5.2   Film Mode Matching Method Solver (FMM)

The single mode width was recalculated using the FMM solver to confirm the results found using the FDM solver. The solver parameter value was chosen for a relative error of $\sim 10^{-4}$%. The graph in Figure 3.11 confirms the result obtained by the FDM solver.
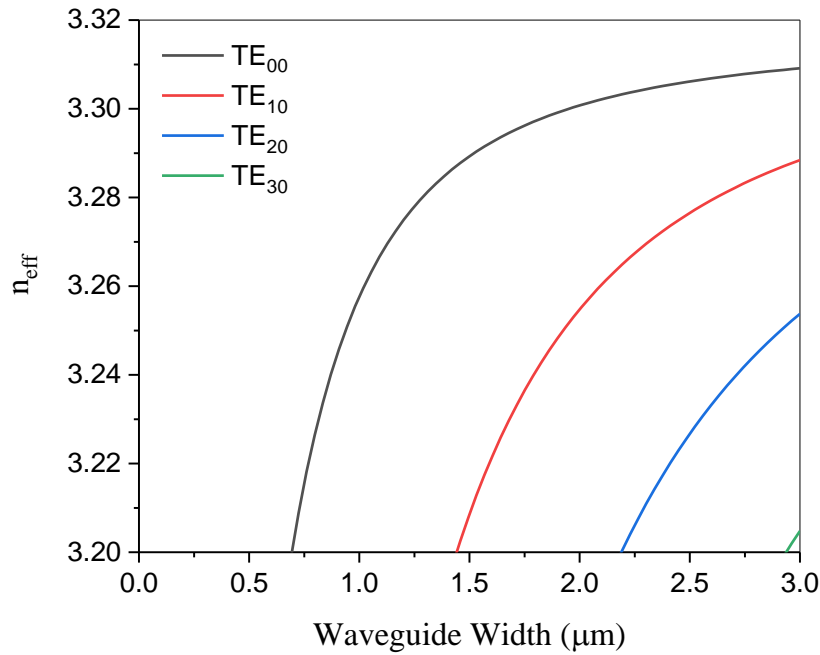
Figure 3.11: Effective indices of supported modes by 2D ridge waveguide in Figure 3.2 of 0.44 μm core height and width up to 3 μm at wavelength of ~1.3 μm using Fimmwave FMM solver with solver parameter corresponds to $\sim 10^{-4}$% relative error.

3.3   Fabrication Tolerances

3.3.6   Waveguide Width

Considering Figure 3.10 and Figure 3.11, it is clear that this structure supports a TE like fundamental mode for widths above 0.7 μm whilst the first higher mode is being confined for widths above 1.42 μm. Figure 3.12-A displays the TE_{00} electric field/intensity profile at a waveguide width of 0.7 μm and Figure 3.12-B shows a TE_{10} electric field/intensity profile within the waveguide of width = 1.42 μm. Both figures show that TE_{00} and TE_{10} are confined well within and not disrupted by the calculation boundaries. Consequently, the single mode width needs to be bigger than that of cut-off of TE_{00}, 0.7 μm, and less than that of the TE_{10} cut-off, 1.42 μm, by an amount equivalent to the tolerance that can be achieved reproducibly in fabrication. Thus, a width of 1.2 μm is a good choice assuming the fabrication error is ~ 100 nm. This value is preferable to smaller widths due to the greater sensitivity at small widths to

fabrication imperfections such as side wall roughness. Also, smaller widths lead to smaller mode size and hence lower coupling efficiencies. Moreover, the first higher mode (TE_{10}) cut-off width (1.42 μm) is not suitable option for the reason that 100 nm error would exceed the limit of single mode condition.
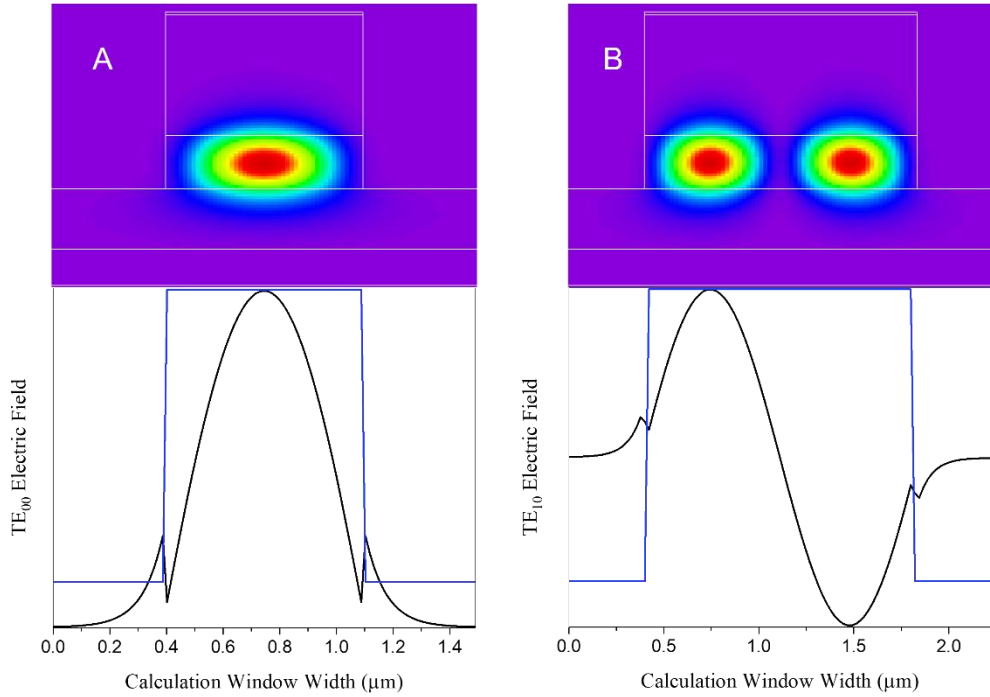
Figure 3.12: (A) Electric field/intensity profile of TE$_{00}$ mode across GaAs/AlGaAs 2D ridge waveguide in Figure 3.2 of core height and width 0.44 μm and 0.7 μm, respectively. (B) Electric field/intensity profile of TE$_{10}$ mode across waveguide of core height and width 0.44 μm and 1.42 μm, respectively. Results are obtained by Fimmwave FDM solver.

3.3.7   Etching Level

A depth etched down to the lower cladding/core interface was chosen as the initial point to trace the changes of the effective index as the waveguide etching depth is varied. The single mode condition was studied at 100 nm below and above the initial point. Figure 3.13-A illustrates the values of the TE$_{00}$ mode effective index as a function of etching level over range of ± 100 nm above/below lower cladding/core interface. The relative change Δn_{eff} was calculated with respect the initial point (lower cladding/core interface) and plotted in Figure 3.13-B. The effective index decreasing as the etching becomes deeper because the overall structure's refractive index is reduced as the BCB refractive index (n=1.544) contribution becomes higher.

As the etching level increasing underneath the initial point, the effective index change becomes slower as the BCB becomes closer to the oxidation layer (n=1.5).
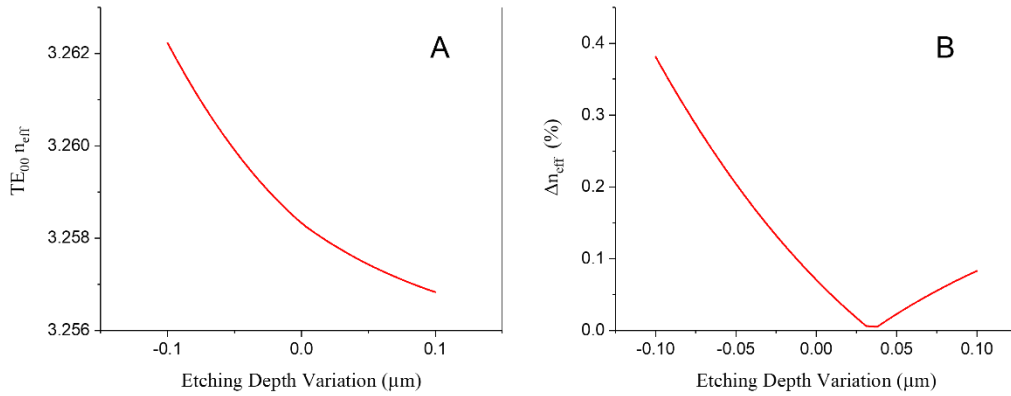
Figure 3.13: (A) FDM calculation of TE$_{00}$ effective index as function of etching level of the GaAs/AlGaAs 2D ridge waveguide in Figure 3.2. (B) TE$_{00}$ effective index relative error versus etching level.

The single mode width condition was traced as the etching level changes and recorded in Table 3.1. It is clear that as the etching becomes deeper, the single mode cut-off width gets wider by ~40 nm [66]. This change is due to the overall boundary slices refractive index reduction as the BCB amount becomes bigger upon deeper etching. So, modes need a wider waveguide to meet the cut-off value of effective index (3.2) and hence become confined.

Table 3.1: Single mode cut-off width of GaAs/AlGaAs 2D ridge waveguide at different etching levels and wavelength of 1.3 µm using Fimmwave FDM solver.

Etching Level	Single Mode Cut-off Width (µm)
100 nm shallower	~1.38
Lower cladding /core interface	~1.42
100 nm deeper	~1.46

3.3.8   Core Height

The waveguide core height was scanned to verify that the single mode condition in the vertical direction is maintained at width of 1 µm. To study the effect of core height variation on the single mode cut-off width, the waveguide width was investigated over variation range of 100 nm less and more the proposed core height value, 0.44 µm. In Figure 3.14, the effective index n_{eff} of both TE$_{00}$ and TE$_{01}$ as function of waveguide core height is presented. The waveguide maintains single mode behaviour in the vertical direction, as shown in the graph, between 0.22 µm and 0.86 µm.
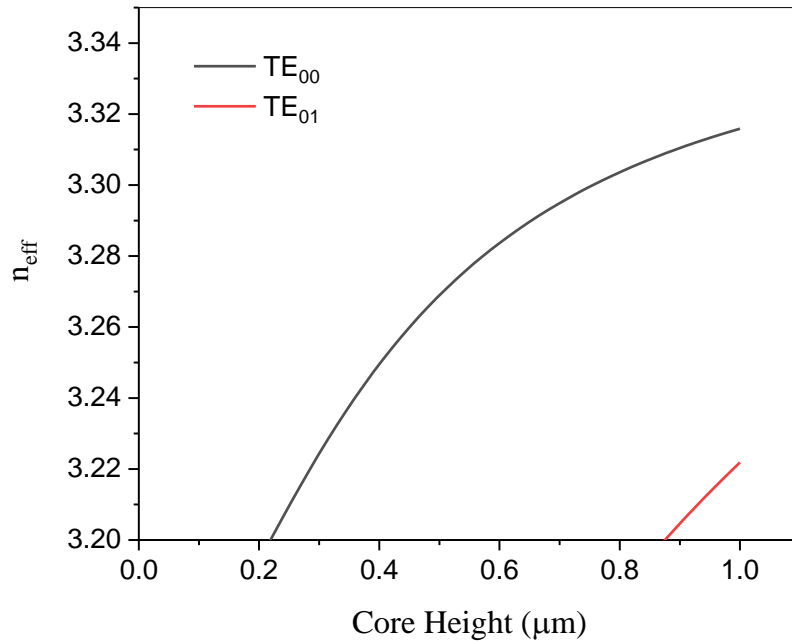
Figure 3.14: Effective indices of the of TE₀₀ and TE₀₁ as core height increases up to 1 µm for GaAs/AlGaAs 2D ridge waveguide of width of 1µm at wavelength of ~1.3 µm using Fimmwave FDM solver.

From data in Table 3.1Table 3.2**Error! Reference source not found.**, it is noticeable that as the core height increases, the single mode width cut-off decreases. As the core become higher, the structure meets the cut-off effective index value (3.20) at narrower widths.

Table 3.2: Single mode cut-off width of GaAs/AlGaAs 2D ridge waveguide at various core heights and wavelength of ~1.3 μm.

Core Height (μm)	Single Mode Cut-off width (μm)
0.34	1.61
0.44	1.42
0.54	1.35

Number of supported modes for various sets of values (core height, waveguide width) is shown in Figure 3.15. The structure does not support modes at a width less than 0.6 μm even with a core height of 1 μm. The single mode condition is fulfilled at widths between 1.2 μm and 2.4 μm for various core heights.
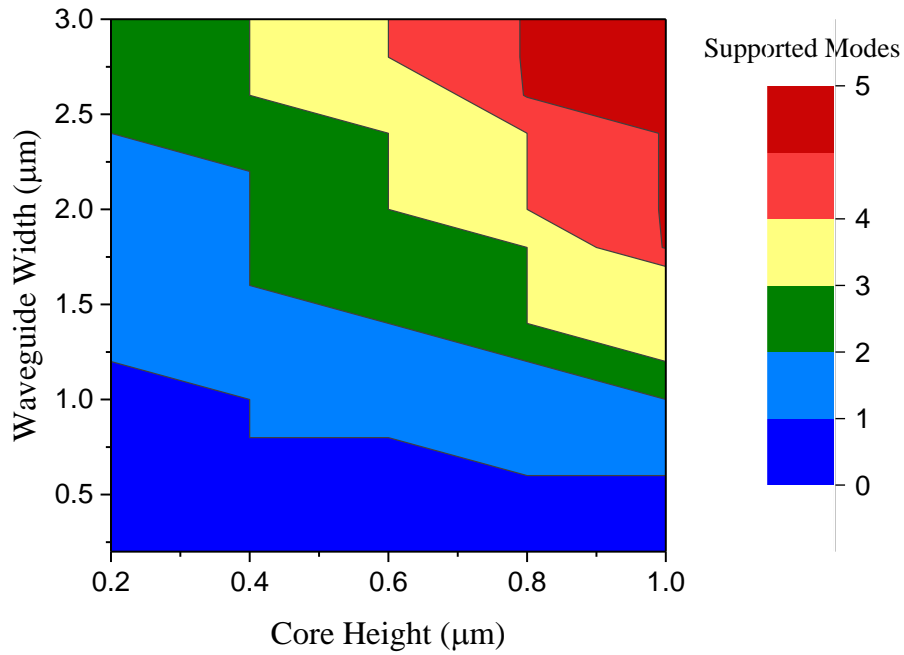
Figure 3.15: Number of supported modes by GaAs/AlGaAs 2D ridge waveguide of different heights and widths at 1.3 μm calculated by Fimmwave FDM solver.

3.4   Wavelength Response

The effect of changing the wavelength was studied at three etching levels (Figure 3.16). As the wavelength increases, the mode size is increases as well. Hence, the TE$_{00}$ mode effective index decreases because the mode area is extended to the material surrounding the core, which is of lower index. However, the TE$_{00}$ mode is still confined by the structure as its effective index is larger than the structure effective index cut-off, 3.20. The TE$_{00}$ mode $n_{eff}(\lambda)$ at the three etching levels is fitted by polynomial regression (3.1) [67]. This polynomial represents the modal effective response (effective modal dispersion) of the fundamental mode, TE$_{00}$, and $\alpha's$, stated inTable 3.3, are fitting constants.

$$n_{eff}(\lambda) = \alpha_2\lambda^2 + \alpha_1\lambda + \alpha_0 \tag{3.1}$$
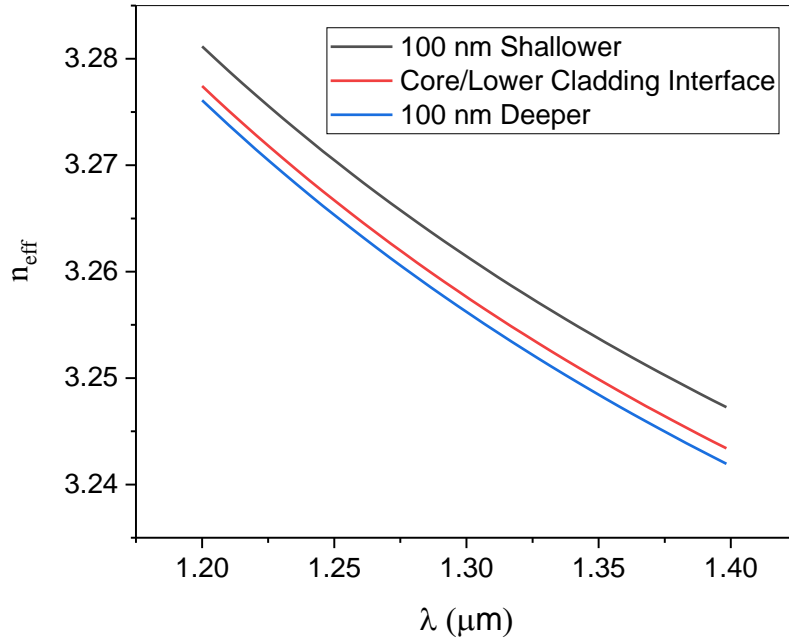
Figure 3.16: TE$_{00}$ effective index as the wavelength increases from 1.2 μm to 1.4 μm for different etching levels of GaAs/AlGaAs 2D ridge waveguide of 0.44 μm height and 1 μm width calculated by Fimmwave FDM solver.

Table 3.3: Fitting constants of equation (3.1) at different etching levels for wavelength range from 1.2 μm to 1.4 μm. values are obtained for GaAs/AlGaAs 2D ridge waveguide using Fimmwave FDM solver.

Etching Level	α_2 (μm^{-2})	α_1 (μm^{-1})	α_0
100 nm shallower	0.2194	-0.7396	3.8523
lower cladding /core interface etching	0.2203	-0.7428	3.8510
100 nm deeper	0.2211	-0.7454	3.8517

The single mode cut-off width was scanned at wavelengths of 1.2 μm and 1.4 μm at the lower cladding/core interface etching level and compared to that at 1.3 μm. Table 3.4 compares the single mode cut-off width and system effective index cut-off at different operating wavelengths at lower cladding/core interface etching level. The cut-off width increases due to mode size increase as wavelength becomes longer. By calculating TE$_{00}$ mode effective area at different wavelengths, it is clear that as the wavelength increases the mode size becomes bigger and hence the mode needs a wider waveguide to be confined. As more mode area spreads over material with a lower refractive index area, the cut-off effective index of the structure becomes smaller.

Table 3.4: Single mode cut-off width of GaAs/AlGaAs 2D ridge waveguide of 0.44 μm core height at different wavelengths. Calculation performed using Fimmwave FDM solver.

λ (μm)	Single Mode Cut-off Width (μm)	Effective Index Cut-Off	TE$_{00}$ Affective Area (μm^2)
1.20	1.35	3.26	0.47
1.30	1.42	3.20	0.53
1.40	1.53	3.18	0.60

3.5   Conclusion

A GaAs/AlGaAs based waveguide was investigated and the single mode height and width necessary for single mode operation were obtained as well as the structure effective index cut-off. The behaviour of a ridge waveguide under the influence of various changes was investigated. It was found that the proposed waveguide has good stability over some fabrication changes as well as a varying wavelength. Hence, a deep etched waveguide structure of core height of 0.44 μm will be considered for multimode design in Chapter 6.

In this chapter, a waveguide that is compatible with lasers and devices like multimode interferometers was studied. In the next chapter large cross-section rib waveguides will be considered.

Chapter 4 :

Large Cross-Section Rib Waveguides

In this chapter single mode operation of large cross-section rib waveguides are investigated over a range of core heights by tracking the first higher TE mode. Thus, design rules of GaAs/AlGaAs waveguides of core heights up to 2 µm were set up at operating wavelengths of 1.3 µm. The fabrication tolerance and wavelength response were studied over a range of variations.

4.1 Background

To ensure low loss coupling and smaller mode mismatch between a typical fibre (or large size circuit components) and a single mode waveguide, large cross-section waveguides (up to few microns width and height) are essential to offer a mode size better matching the size of the fibre (Figure 4.1) [68]. Waveguides of this range of size are also desirable because they are expected to relax fabrication tolerances and minimum feature sizes. The core slice can be controlled to support one mode only by choosing proper etching level so that the higher modes have effective indices smaller than the fundamental mode of the boundary slices [69]. Based on the structure demonstrated in section 3.1, the schematic of the rib waveguide studied is seen in Figure 4.2. The waveguide dimensions can be parametrised using the value of the free space wavelength λ, as shown, which makes sense because the waveguide dimensions are now comparable to λ. The parameter a describes the width of the waveguide rib, $W = 2a\lambda$, and the height of the core is $H = 2b\lambda$. The etching depth, or rather the height of the waveguide that is not etched, is described by the parameter $r = h/H$. Studying the relation between W/H (or equivalently a/b) and r gives a quantitative description of the single mode conditions of different sets of values (H, W, r).
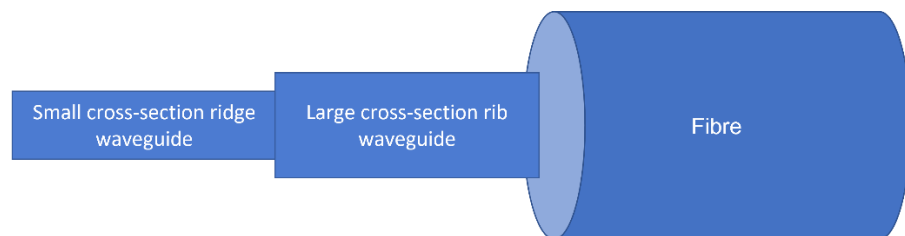
Figure 4.1: Fibre-circuit coupling through large cross-section waveguide.

To be the basis of large cross-section waveguides, the central slice needs to satisfy the large cross-section condition (equation 4.1) stated by Soref et al [69].

However, a large cross-section waveguide is one in which the horizontal single mode cut-off is due to the vertical mode at a certain critical etching level (for example, $H = 0.9\ \mu m$ for a GaAs/AlGaAs based waveguide).
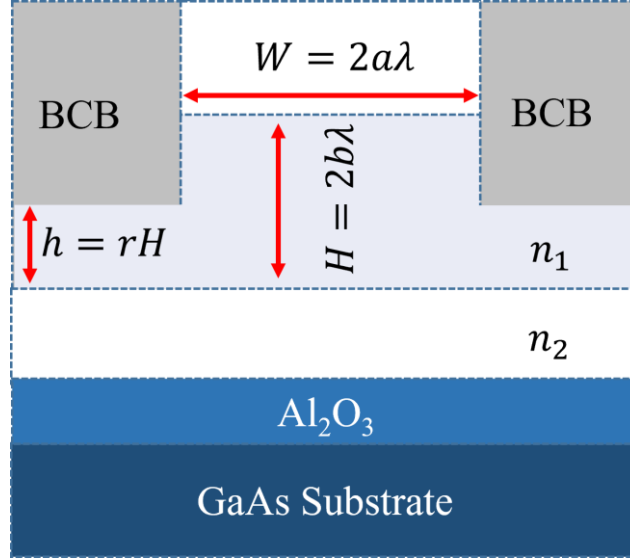
Figure 4.2: Large cross-section GaAs/AlGaAs 2D rib waveguide structure in xy plane. W is the central slice width, H is the central slice core height and h is the core height of the boundary slices.

$$2b\sqrt{n_1^2 - n_2^2} \geq 1 \tag{4.1}$$

So, the critical value of b is when the equality is satisfied in equation (4.1):

$$b_c = \frac{1}{2\sqrt{n_1^2 - n_2^2}} \tag{4.2}$$

Which is defined as limit of large cross-section [69]. Note that the condition to be a large cross-section waveguide does not depend on either the etching depth, r, or the width but on the confinement of the structure. The bigger the difference in the denominator of (4.2), the smaller the b_c and hence smaller core height is needed for large cross-section waveguide (higher vertical mode confinement). n_1, n_2 are the core and lower cladding refractive indices, respectively and b is a constant related to H and the wavelength,λ, by

$$b = \frac{H}{2\lambda} \tag{4.3}$$

a and b are related to each other by

$$\frac{W}{H} = \frac{a}{b} \leq c + \frac{r}{\sqrt{1 - r^2}} \qquad (4.4)$$

where c is a correction constant that depends on H, r and polarisation [70] and r is etching level factor of values of

$$r_c < r < 1 \qquad (4.5)$$

We will see how good (4.4) is with our structure. For a central slice core height, the design of large cross-section rib waveguide is controlled by the critical etching depth which determines the single mode cut-off of the (2D) rib waveguide, r_c [71]

$$r_c = \frac{2H\sqrt{n_1^2 - n_{eff}^2(TE_{01})} - \lambda}{2H\sqrt{n_1^2 - n_{eff}^2(TE_{01})}} \qquad (4.6)$$

Where $n_{eff}(TE_{01})$ is the effective index of the first higher mode of the (1D) slab waveguide of a certain height, H, corresponding to the central slice in Figure 4.2.

4.2 Methodology

This work focuses on certain core height values as presented in Table 4.1.

Table 4.1: Waveguide core heights.

b	$H = 2b\lambda$
$< b_c$	0.9
b_c	1.1
$> b_c$	1.2 ($H < \lambda$)
0.5	1.3 ($H = \lambda$)
0.77	2.0 ($H > \lambda$)

For each height, the vertical modes were calculated by the effective index solver to determine the first higher 1D mode of central slice. Then, the critical etching

depth factor r_c for the large cross-section rib waveguide was found using equation (4.6). After that, the rib waveguide width was scanned to find the single mode cut-off width. By studying the relation between H and r_c, the single mode cut-off in each case was classified based on whether it was a vertical or horizontal mode that ended the single mode condition. For each height the single mode width of the rib waveguide was found for different etching depths (different r values) using the finite difference solver [61] and the results compared to literature values of c ($c = 0.3$ where beam propagation and mode matching methods were used [69], $c = 0$ [72] obtained using the effective index method based on experimental results in [73] and $c = \frac{0.15 r^3}{\sqrt{1-r^2}}$ using effective index method [71]). The steps are summarised in Figure 4.3. The rib waveguide higher order modes leak out if their effective indices are smaller than that of the boundary slices fundamental vertical mode [74], [75] which was calculated by the film mode matching solver [61].

1
- Calculate the first higher vertical mode, TE_{01}, of the central slice.

2
- Find the critical etching depth factor, r_c, from equation (4.6).

3
- Scan the rib waveguide width to find the single mode cut-off width.

4
- Find the single mode width for each height at different r values.

5
- Find the value of c for each height.
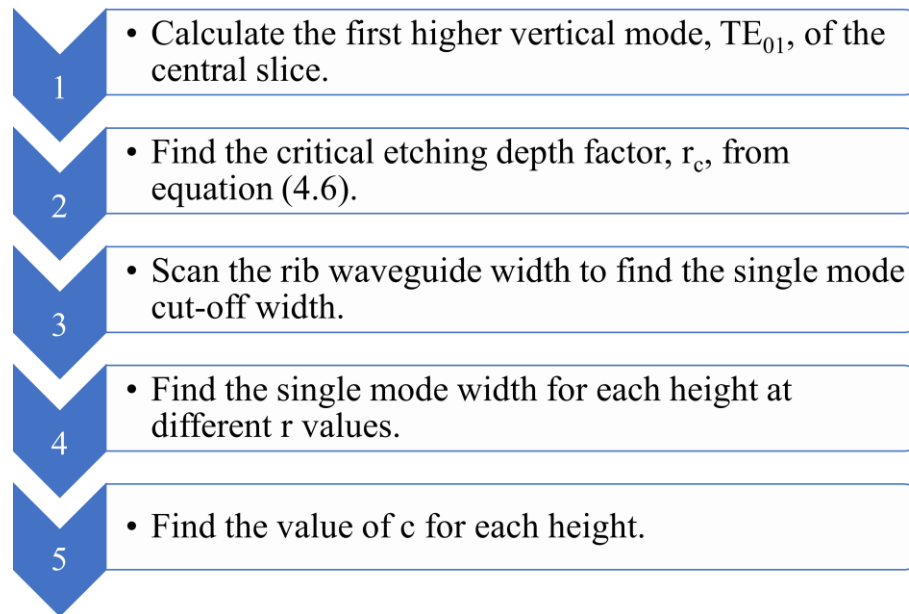
Figure 4.3: Calculating c values for different core heights of GaAs/AlGaAs 2D rib waveguide.

The same strategy of optimising the calculation window size and input parameters for the solver as in chapter 3 was followed here to compromise between reasonable accuracy and the calculation time required. For example, for $H = 2$ μm, boundary slices width is chosen to be 2 μm when $r = 0.5$ and number of cells across the calculation window is 100 cell which corresponds to relative error $\Delta n_{eff} = \sim 10^{-4}\%$ and calculation time =2.3 s/calculation.

4.3   Single Mode Cut-Off

The single mode condition was calculated in the vertical direction first for a slab waveguide and then the modes were traced as the rib waveguide width is increased to find the single cut-off width.

4.3.1   Single Mode Height

For the central slice (1D) slab waveguide core heights H, in Figure 4.2, the effective index of the first higher order mode, $n_{eff}(TE_{01})$ was calculated using the effective index solver in order to obtain r_c values. Figure 4.4 shows the positive correlation between H and $n_{eff}(TE_{01})$. This behaviour is expected as the higher the core, the bigger mode area that is enclosed by the core.
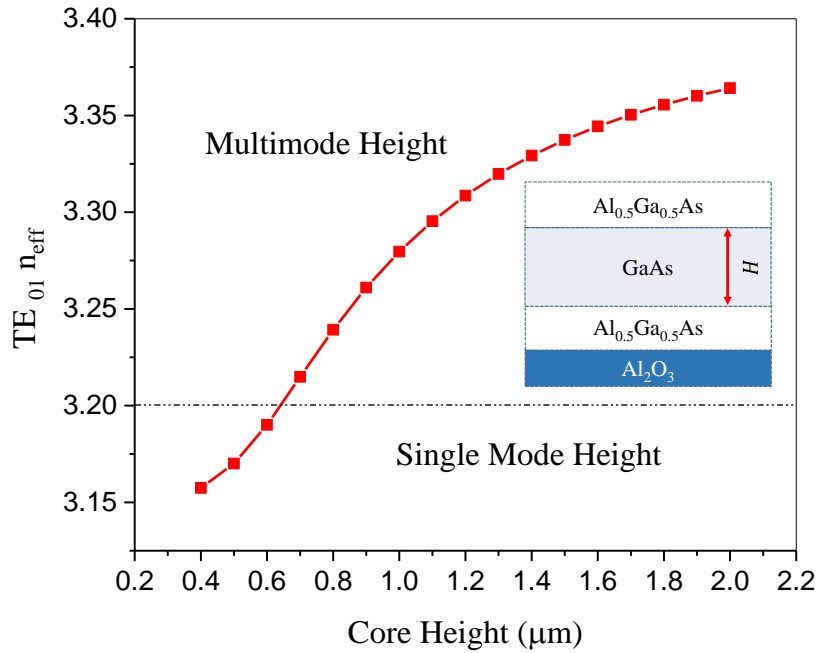
Figure 4.4: GaAs/AlGaAs 1D slab waveguide TE_{01} effective index as the core height increases. Results are obtained by EIM solver in Fimmwave at ~1.3 μm.

r_c was calculated for core heights from 0.4 μm to 2 μm and the main remarkable points are illustrated in Figure 4.5. An important outcome is the negative values of r_c which occur at core heights corresponding to $2H\sqrt{n_1^2 - n_{eff}^2(TE_{01})} < \lambda$

where the core is not supporting a higher mode. Another interesting aspect of this graph is that this structure is showing the behaviour of a large cross-section waveguide at core heights below the large cross-section condition, equation (4.1). Moreover, Figure 4.5 locates the first height at which the single mode cut-off width is due to the first excited horizontal mode, TE_{10}.
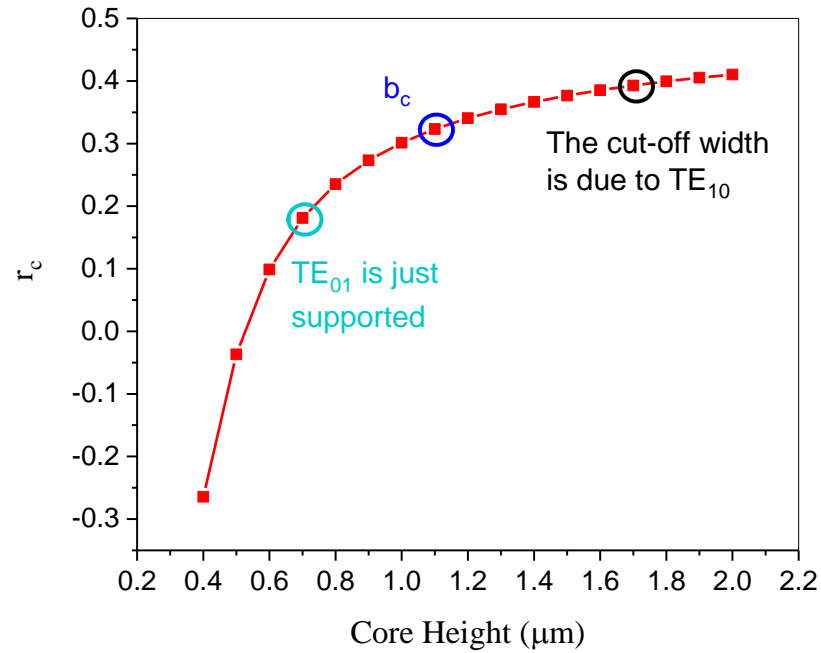
Figure 4.5: The critical etching factor for GaAs/AlGaAs 2D rib waveguide using equation (4.6) at ~1.3 μm as the core height increases.

To evaluate the lowest r_c value for various heights, r_c was calculated for core heights up to 12 μm. Interestingly, in Figure 4.6 it is clear that r_c increases as the core height increases. Furthermore, r_c hits the literature value [69], [76], 0.5, at H=10 μm.
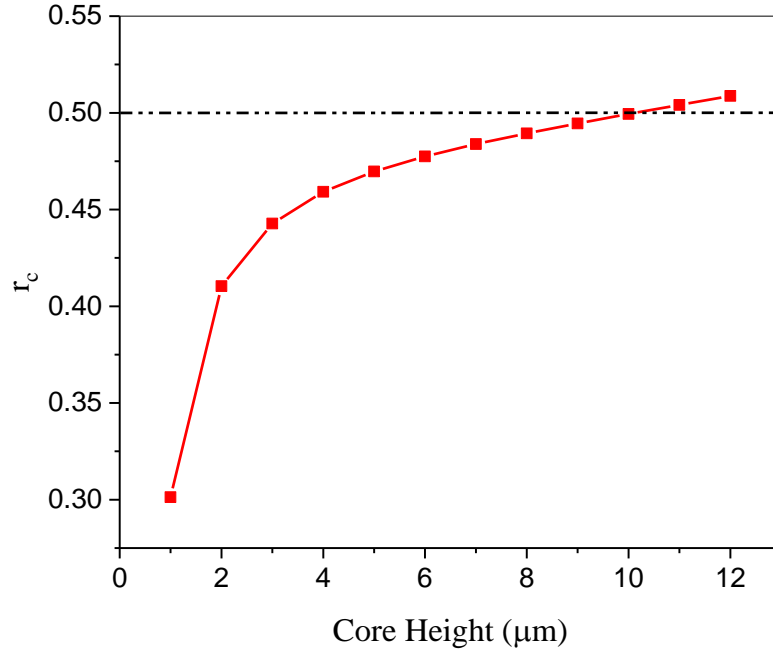
Figure 4.6: The critical etching factor for GaAs/AlGaAs 2D rib waveguide using equation (4.6) at ~1.3 μm for core height ranges from 1 μm to 12 μm.

4.3.2 Single Mode Width

Using the finite difference method solver, the single mode cut-off width of the large cross-section waveguide was investigated for rib waveguides of several core heights, $H = 0.9, 1.1, 1.2, 1.3$ and $2 \, \mu m$, at r_c as seen in Figure 4.7. The main noticeable outcome is that the single mode cut-off width at r_c becomes wider as the core height becomes higher. In addition, the TE_{01} mode effective index becomes closer to that of the TE_{10} mode and then at a certain height and width they become degenerate and then the TE_{10} mode effective index becomes bigger than that of TE_{01}. It can be seen that the single mode cut-off width is a result of the vertical mode (TE_{01}) for rib waveguides of $H \leq 1.3 \, \mu m$. However, the cut-off becomes due to the horizontal higher mode (TE_{10}) as the etching become shallower (for $r > r_c$) as TE_{01} becomes more likely to leak out into the boundary slices.
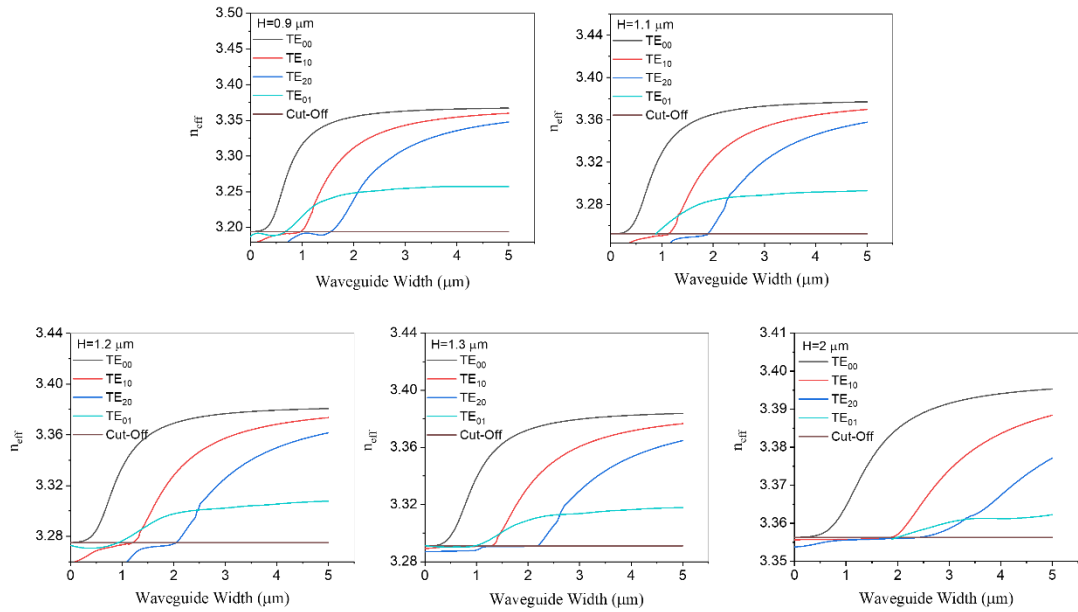
Figure 4.7: Single mode cut-off width for for GaAs/AlGaAs 2D rib waveguide of various core heights at r_c using Fimmwave FDM solver at ~1.3 μm.

The relation between r_c at various core heights ($H = 0.9, 1.0, .., 2.0\ \mu m$) and the single mode cut-off width is plotted in Figure 4.8 to recognise the type of cut-off. The outcomes of the simulation suggest that the widths at which single mode cut-off occurs are due to vertical modes (TE_{01}) for heights up to 1.6 μm.
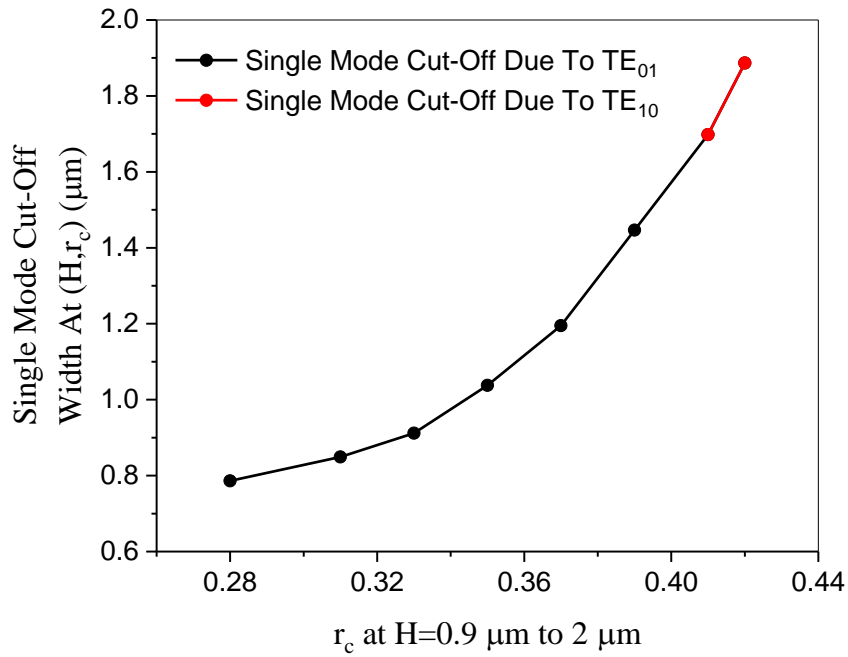
Figure 4.8: Single mode cut-off width as function of r_c(H) calculated for GaAs/AlGaAs 2D rib waveguide using FDM solver at ~1.3 μm.

A closer inspection of some core heights (Figure 4.9 to Figure 4.13) clarifies the differences between literature values of c [69], [71], [72] and the FDM solver based values. For all investigated heights, the correction factor, c, was found and it fits values of $r_c < r \leq 0.8$. Furthermore, the closest correction constant, c, in equation (4.4) is plotted as function of core height in Figure 4.14.
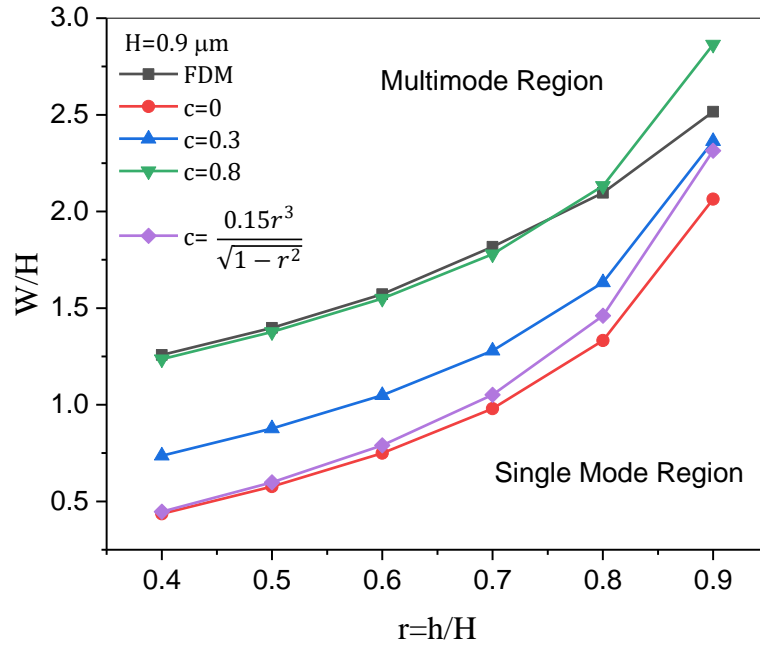
Figure 4.9: The ratio of single mode cut-off widths to the core height at various etching levels for GaAs/AlGaAs rib waveguide of $H = 0.9$ μm for various c values compared to Fimmwave FDM solver results and its best fitted c.
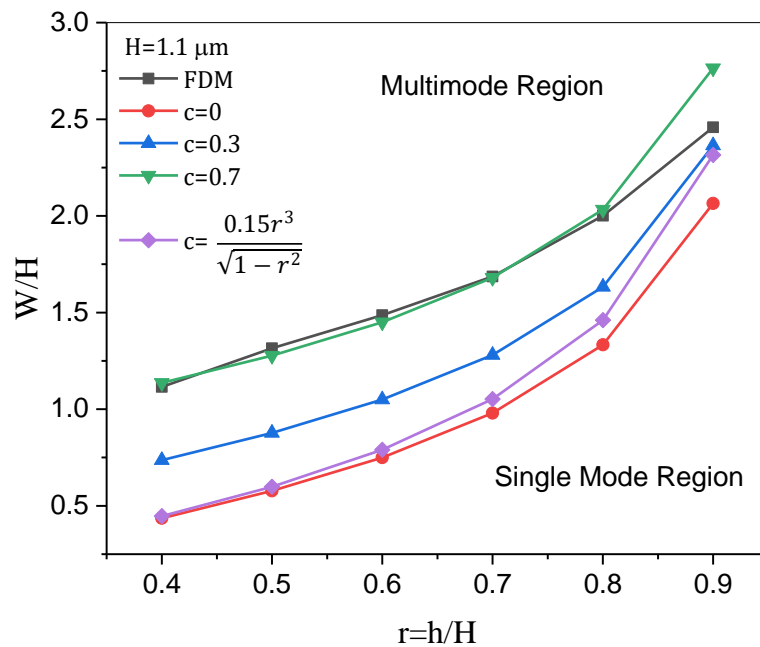
Figure 4.10: The ratio of single mode cut-off widths to the core height at various etching levels for GaAs/AlGaAs rib waveguide of $H = 1.1$ μm for various c values compared to Fimmwave FDM solver results and its best fitted c.
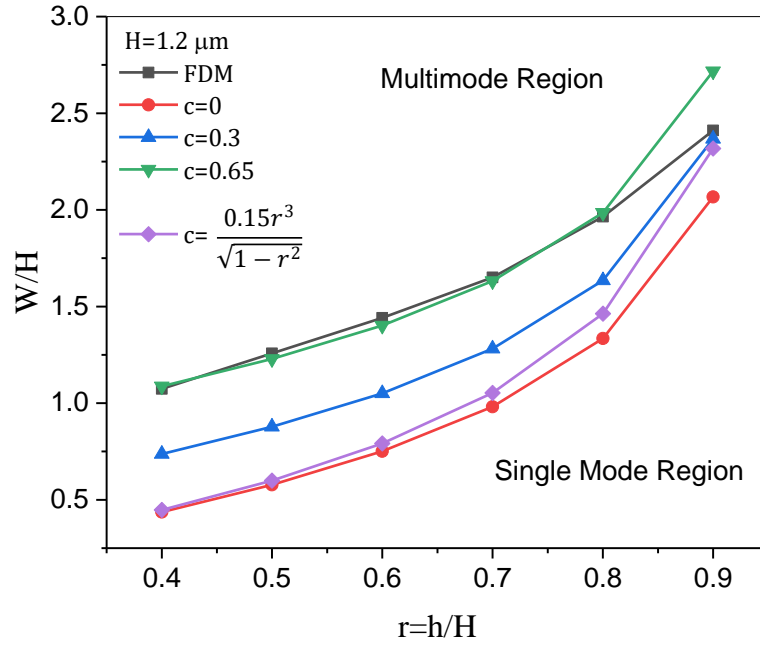
Figure 4.11: The ratio of single mode cut-off widths to the core height at various etching levels for GaAs/AlGaAs rib waveguide of $H = 1.2$ μm for various c values compared to Fimmwave FDM solver results and its best fitted c.
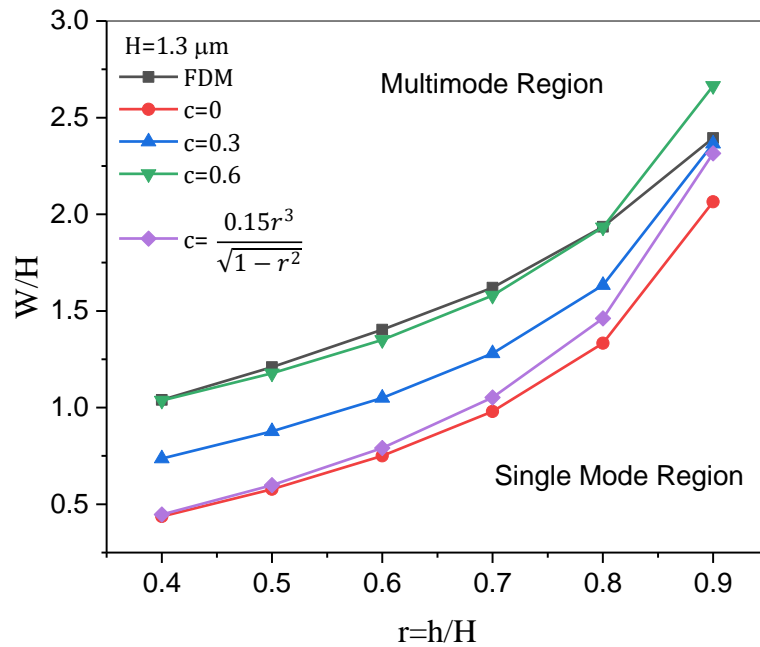
Figure 4.12: The ratio of single mode cut-off widths to the core height at various etching levels for GaAs/AlGaAs rib waveguide of $H = 1.3$ μm for various c values compared to Fimmwave FDM solver results and its best fitted c.
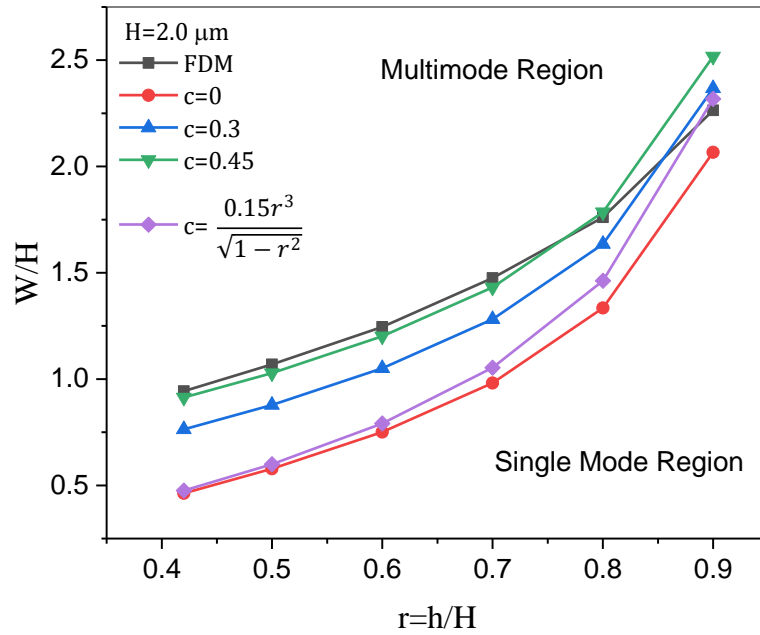
Figure 4.13: The ratio of single mode cut-off widths to the core height at various etching levels for GaAs/AlGaAs rib waveguide of $H = 2.0$ μm for various c values compared to Fimmwave FDM solver results and its best fitted c.
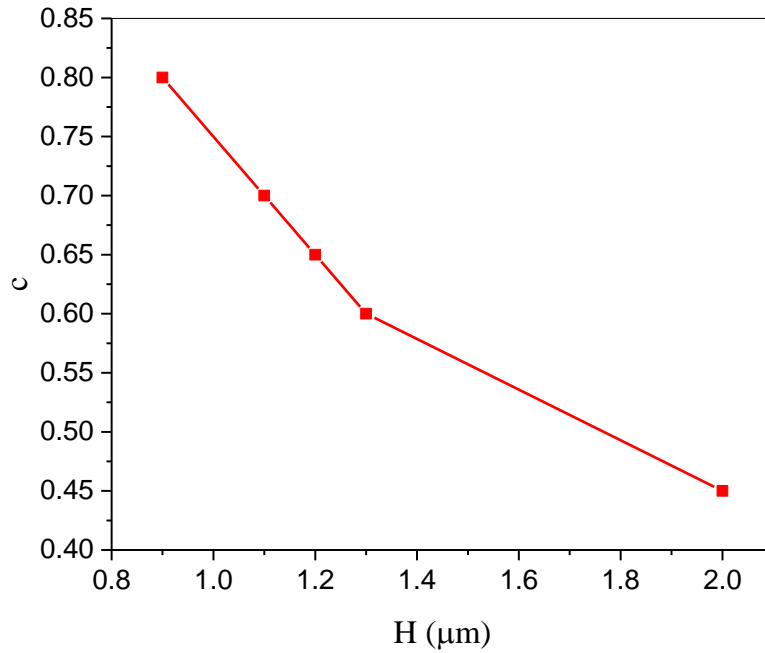
Figure 4.14: Relation between best fitted c and H of GaAs/AlGaAs rib waveguide.

4.4 Tolerances

The single mode cut-off tolerance to unintentional width variations was investigated for $H = 0.9, 1.1, 1.2, 1.3$ and $2 \, \mu m$ and $r = 0.6$. and the results are presented in Table 4.2. It is noticeable that the tolerance to variations in the width increases as H increases.

Table 4.2: Width tolerance at various core heights and $r = 0.6$ for GaAs/AlGaAs rib waveguide as calculated by Fimmwave FDM solver.

H (μm)	Waveguide Width (μm)	Tolerance (μm)
0.9	1.20	± 0.22
1.1	1.30	± 0.30
1.2	1.30	± 0.40
1.3	1.40	± 0.42
2	2.0	± 0.57

4.5 Wavelength Response

The wavelength response was tracked for single mode waveguides of $H = 0.9, 1.1, 1.2, 1.3$ and $2 \, \mu m$ and $r = 0.6$ over range of $1.3 \pm 0.1 \, \mu m$ as presented in Figure 4.15. All investigated heights exhibit the same behaviour with increasing wavelength, which is similar to the result for the small cross-section waveguides in Chapter 3.
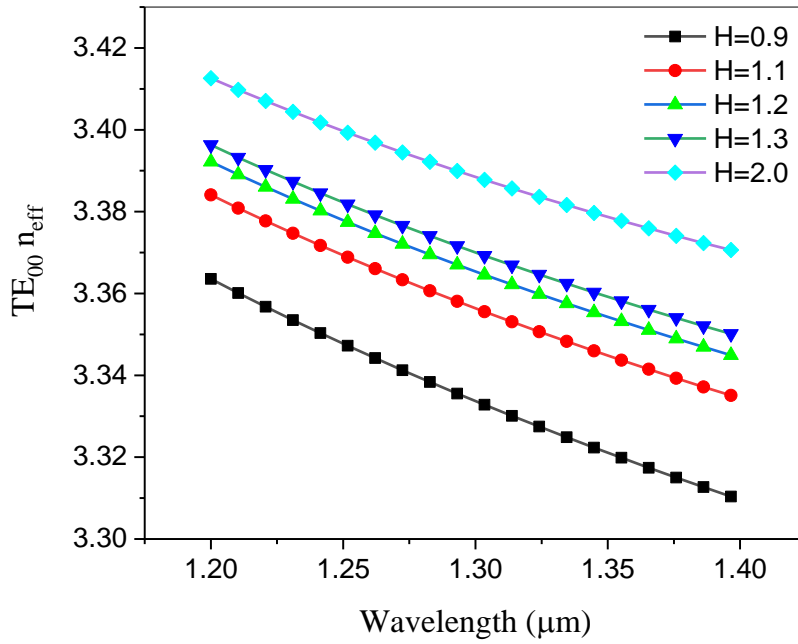
Figure 4.15: TE_{00} **effective index wavelength response for GaAs/AlGaAs rib waveguide of different heights and** $r = 0.6$**. Results obtained by Fimmwave FDM solver.**

Table 4.3 compares the single mode cut-off widths for the investigated heights at various wavelengths. It is clear that as the wavelength increases, the cut-off width increases owing to mode size increase and hence a wider waveguide is needed to confine it.

Table 4.3: Single mode cut-off width for GaAs/AlGaAs rib waveguide of $r = 0.6$ **and various core heights and wavelengths.**

Core Height (µm)	Cut-off width at $\lambda = 1.2 \ \mu m$	Cut-off width at $\lambda = 1.3 \ \mu m$	Cut-off width at $\lambda = 1.4 \ \mu m$
0.9	1.32	1.38	1.48
1.1	1.56	1.60	1.68
1.2	1.66	1.70	1.78
1.3	1.72	1.80	1.86
2.0	2.48	2.50	2.56

4.6   Conclusion

In this chapter, waveguides of core heights corresponding to large cross-sections were investigated to achieve single mode operation at shallow etching levels. A single mode design rule was set for large cross-section rib waveguides for several core heights. First, the critical etching level for a core height is defined. Then, for an etching level above the critical one, the single mode width can be obtained. Hence, single mode operation is obtained. At the critical etching level, the single mode widths were classified based on whether they are due to vertical or horizontal modes. Also, the relation between the tolerance to variation in the width and the core height was studied and the spectral response was investigated. The designs covered in this chapter are suitable for range of applications like circuit-fibre coupling large cross-section.

In the next chapter, the propagation along the waveguide will be considered to study tapered waveguides.

Chapter 5 :

Design and Optimisation of

Tapered Waveguides

An important property of a taper is its ability of changing a mode size with low loss using a relatively small footprint. In this chapter I will investigate the level of loss that can be achieved in small footprint devices, while being tolerant to unintended changes in fabrication or operating conditions and fabricated from the GaAs /AlGaAs system in a manner compatible with the work in the previous chapters. Two design rules are applied aiming to design optimised efficient (high power transmission with short length) tapers. They are compared with a conventional (linear) taper in terms of length, efficiency (power transmission) and stability over several changes like waveguide width and operating wavelength. The simulations were carried out to track mode evolution by implementing the eigenmode expansion method.

5.1   **Background**

Optical tapers should transfer optical power between two different size modes with a high efficiency. In photonic integrated circuits, this transfer is usually from one waveguide of large cross-section into one of much smaller cross-section (or vice-versa) or from a photonic circuit edge to a fibre. The small overlap of the modes between such disparate waveguides means that the efficiency of a simple butt-join (or taper of zero length) is small (depending on the mismatch between the cross-sections). The common solution to this problem is to simply make a linear taper of very long length, such that the optical power is transferred from the initial to the final mode in an adiabatic way. In some situations, designers seem to opt for a pragmatic solution of even longer lengths without considering the shortest possible adiabatic taper. In systems where material costs are higher, such as the one considered here, this is not an option for commercial applications as these linear tapers must be long to maintain the adiabaticity, and this long length is a problem for the footprint of a photonic integrated circuits.

To investigate the efficiency, several taper shapes (e.g. linear or with some form of curve) have previously been studied by treating the tapered region as a sequence of step tapered waveguides and varying several parameters to obtain the best performance [77], [78]. Taper transmission was tested for various shapes at the same length and then taper length was optimised for the shape corresponding to the highest transmission [79] . SOI non-adiabatic interference-based tapers have been proposed

by optimising both length and width of the taper such that the resonance modes undergo progressive interference along the taper [80], [81]. Adiabatic compact tapers have been proposed in silicon [82], [83]. Based on a design rule (slow waveguide divergence) that guarantees the adiabaticity along the length of the taper, an adiabatic taper has been compared to various shapes like linear, parabolic and cosine tapers [84], [85]. Silicon nitride based exponential tapers with exponents of integer values, $a = 1,2,3,4$, have been investigated and compared to other shapes for on-chip integration with arrayed waveguide gratings. It has been found that an exponential taper of exponent, $a,$ of 2 has the highest efficiency [86].

Tapers are often used as part of other components (composite building blocks). SOI based adiabatic couplers with tapers described by linear, quadratic, and exponential functions have been compared. It has been found that exponential width tapering function gives the best performance [87]. The performance of tapered AlInAs/InGaAs/InP quantum cascade lasers have been compared for three types of tapered section [88]. A taper of 6° angle, 1.5 mm length and widths of 4 and 150 μm has been implemented to increase the output power of distributed-feedback Bragg (DFB) semiconductor lasers [89]. Polymer ring resonators with a tapered section with high sensitivity for biomedical sensing have been reported [90]. Fibre-to-chip coupling Al_2O_3/Si inverse tapers at 1550 have been optimised using a particle swarm optimisation algorithm [91].

A taper of length L with arbitrary shape can be specified by its width $W(z)$ or, equivalently, the angle $\theta(z)$, for $0 \leq z \leq L$ (see schematic of top view of taper in Figure 5.1), where

$$\tan \theta(z) = \frac{1}{2} \frac{dW}{dz} \qquad (5.1)$$
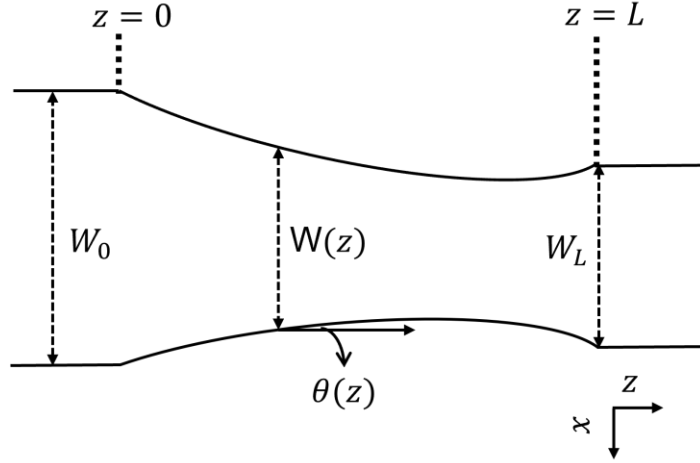
Figure 5.1: Top view schematic figure of the taper in xz plane. W_0 and W_L are taper widths at $z = 0$ and $z = L$, respectively. $W(z)$ is taper width and $\theta(z)$ is taper angle at position z where z is propagation direction.

In theory, an adiabatic design is one in which there is no transfer of energy between modes. When the modes are changing, as is the case in a taper, then the changes must be slow enough such that higher order modes are not excited (absolute adiabaticity). Although this situation is ideal, something close to absolute adiabaticity can be achieved. The taper design rules, applied here, work by ensuring that the local spreading of the waveguide walls (given by equation (5.1)) is slower than the diffraction driven spreading of the waveguide mode (given by equation (5.2)). The condition on the angle of the widening waveguide θ is

$$\theta < \frac{\lambda_0}{2W n_{eff}} \tag{5.2}$$

where W is the local width of the waveguide and n_{eff} is the effective refractive index of a waveguide of width W. Linear tapers have a constant value of θ, and the shortest adiabatic linear tapers must satisfy the above for the largest values of $W n_{eff}$. A shorter taper length that maintains adiabaticity can be found by exploiting the large n_{eff} dependence on W (Figure 5.2-A) in a high-contrast waveguide. The aim of this chapter is to investigate tapers designed according to rules from [82] and [78] for a deep etched and high confinement tapered waveguide and compare them to a linear taper. These tapers are designed to deliver a signal between multimode waveguide (Figure 5.2-B) and a single mode waveguide (Figure 5.2-C) with high performance: low loss and good

stability against fabrication variations. In the following sections, various taper design rules are demonstrated.
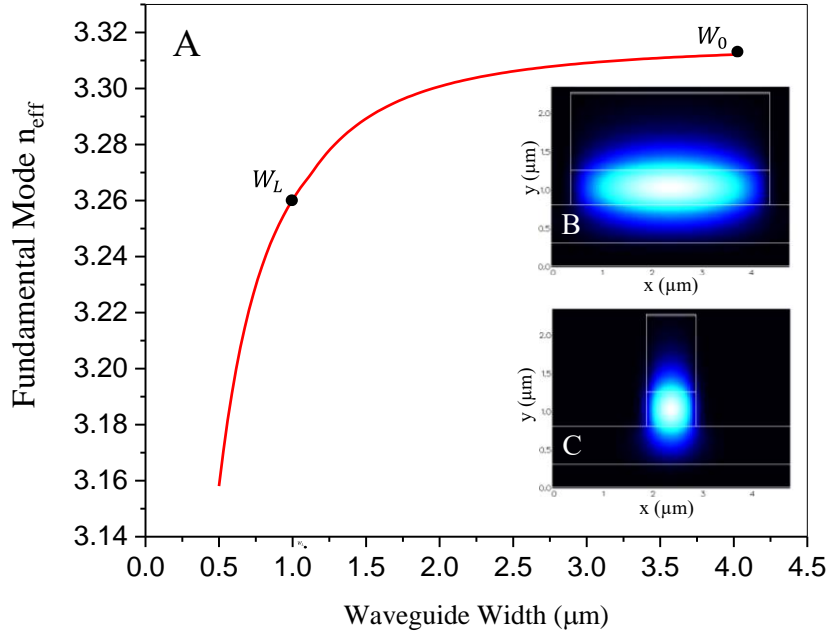
Figure 5.2: (A) Fundamental mode effective index, n_{eff}, as function of GaAs/AlGaAs waveguide width. (B) Intensity profile of the fundamental mode (in xy plane) at the beginning of the taper ($W_0 = 4\mu m$) and at (C) the end of the taper ($W_L = 1\mu m$) as calculated by Fimmwave FDM solver.

Three types of tapers are investigated in this chapter: adiabatic tapers (defined as constant α), linear tapers (defined as constant θ) and exponential (defined as constant a). In the following sections, the three constants α, θ and a are explained.

5.1.1 Adiabatic Taper

To be adiabatic at each position z along its length, the angle $\theta(z)$ must satisfy the condition given in equation (5.1). Following [82], we define an "adiabaticity parameter" α:

$$\theta = \alpha \frac{\lambda_0}{2W n_{eff}} \tag{5.3}$$

such that the taper is adiabatic for positions z where $\alpha(z) \leq 1$. Here we are interested in designing adiabatic tapers that have a constant α along their length. To design such

a taper, knowledge of the effective index as a function of waveguide width $n_{eff}(W)$ is required. In general, the width change along the taper needs to be smooth so that the mode adapts itself continuously without radiating or being converted to a higher order mode and hence maintains a high efficiency. This width change is controlled by both the length and shape of the taper. From knowledge of $n_{eff}(W)$, the taper shape $W(z)$ or $\theta(z)$ for any constant value of α can be calculated iteratively. Approximating equation (5.2) in terms of finite differences, it quickly becomes apparent that the width $W(z + \delta z)$ at position $z + \delta z$ is related to the width $W(z)$ at position z by:

$$W(z + \delta z) = W(z) + 2\delta z \tan \theta \qquad (5.4)$$

This iterative method gives the true shape only when $\delta z \to 0$, so the taper should be broken into many parts of small length (in practice we use $\delta z = 0.01$ μm). The starting point is at $z = 0$ and is chosen as the width of the initial waveguide. Before starting, it is not possible to say what the length L of any taper with a constant α will be, but it is simple to stop the iteration when $W(z)$ reaches the desired end waveguide width, with the length L being the final value of z. While equation 5.1 is a good guide we will find that smaller values of α yield more adiabatic tapers, albeit with longer lengths, and therefore should be more efficient.

5.1.2   Linear Taper

For linear tapers, the length, L, is the main parameter that improves the adiabaticity. According to the negative correlation (equation (5.5) [92]) between the taper's angle, θ, and L, a linear taper needs to be long enough to assure small taper angle along the taper where $\theta(z)$ is constant along the taper length.

$$L = \frac{W_0 - W_L}{2 \tan \theta} \qquad (5.5)$$

$W_0 = W(0)$ is the initial width of the taper at $z = 0$, and $W_L = W(L)$ is the final width of the taper at $z = L$.

5.1.3   Exponential Taper

Here I present an exponential taper to show that the shape is similar to the adiabatic tapers presented above. The exponential taper is defined by its exponent, a, and the width of the taper along the length is [78]:

$$W(z) = W_L + (W_0 - W_L)\left(1 - \frac{z}{L}\right)^a \qquad (5.6)$$

The angle of the taper along its length $\theta(z)$ is given by (see equation (5.2)):

$$\tan(\theta(z)) = \frac{1}{2}\frac{dW}{dz} = \frac{a}{2L}(W_L - W_0)\left(1 - \frac{z}{L}\right)^{a-1} \qquad (5.7)$$

When designing an exponential taper shape, the taper length L, start/end widths W_0/W_L and exponent a can be chosen independently, giving a lot of flexibility. Once the desired taper length and start/end widths are known, the exponent a can be optimised to give the best possible efficiency. An advantage of this design rule is that the shape and length can be chosen based on conditions including space on the chip and ease of fabrication of curved or straight waveguide boundaries.

5.2   Methodology

The calculations involved when studying tapers are actually the same waveguide calculations considered in chapter 3. At each position, the tapers (local) modes are calculated as if it were a waveguide of the same width. Here, the calculations are performed for a ridge waveguide that is tapered along the propagation direction (Figure 5.1) to make the transition from multimode to single mode waveguide. The calculation window size of the ridge waveguide that was set in chapter 3 is used here. Also, the FDM solver parameter (mesh size) value that is chosen in the calculation in Chapter 3 for ridge waveguides are suitable to use here.

The maximum number of calculation modes[3] included in the calculation affects the accuracy for waveguides/devices where the cross-section varies along the propagation direction. Hence, the number of modes was checked for accuracy and

---

[3] This is calculation parameter that define number of calculated modes included when simulation is caried out along propagation direction.

resource efficiency. The number of modes was set for an error less than 4.5 % (see Figure 5.3).
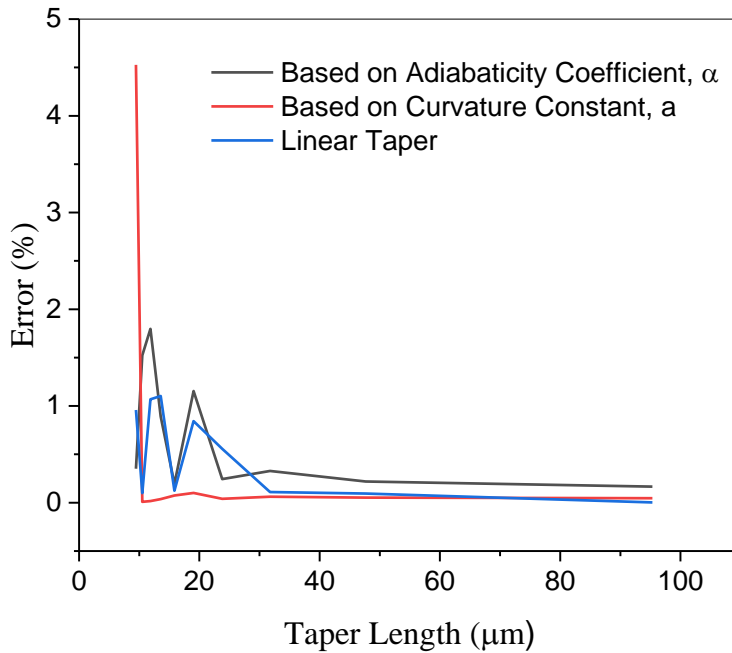
Figure 5.3: Fimmprop (eigenmode expansion) calculation error based on number of modes included in the calculations for various GaAs/AlGaAs taper lengths and types.

As seen in Figure 5.4, the smallest size of discretisation and the size of mode variation are selected for an accuracy of higher than 99.87 % for various taper lengths and types.
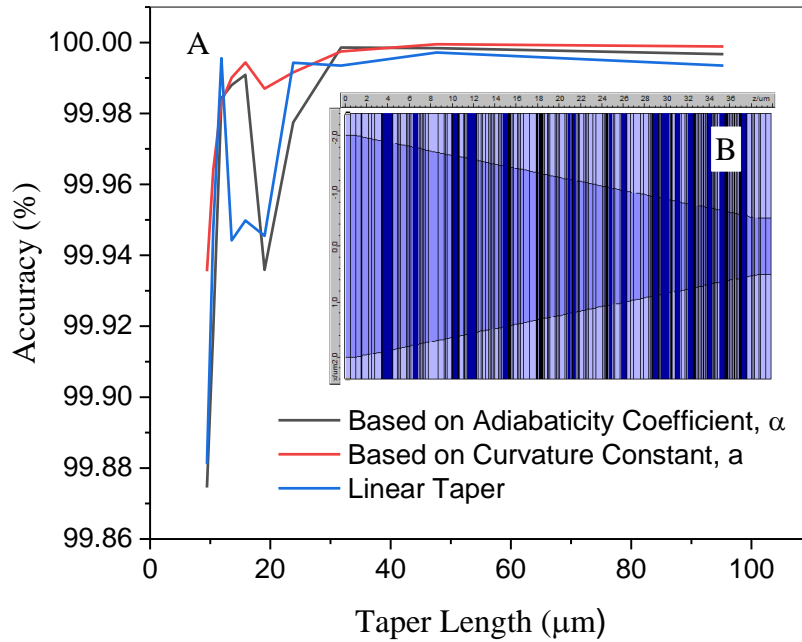
Figure 5.4: (A) Fimmprop (eigenmode expansion) calculation accuracy for each taper algorithm. (B) Taper discretisation density as controlled by mode changes along the taper.

5.3   Optimisation

In this section, various optimisation results for the fundamental TE mode are presented based on the equations (or design rules) described above of adiabatic, linear and exponential tapers. This allows the prediction of optimum GaAs/AlGaAs-based taper shapes before fabrication or integration with other components.

5.3.4   Adiabatic Taper

Applying the adiabaticity design rule, equation (5.3), for $\alpha = 1$, a taper of length, $L = 19.03$ µm is obtained and shown in Figure 5.5-A. Simulations suggest that the efficiency is 98.22 % (see Figure 5.5-B for the calculated fields).
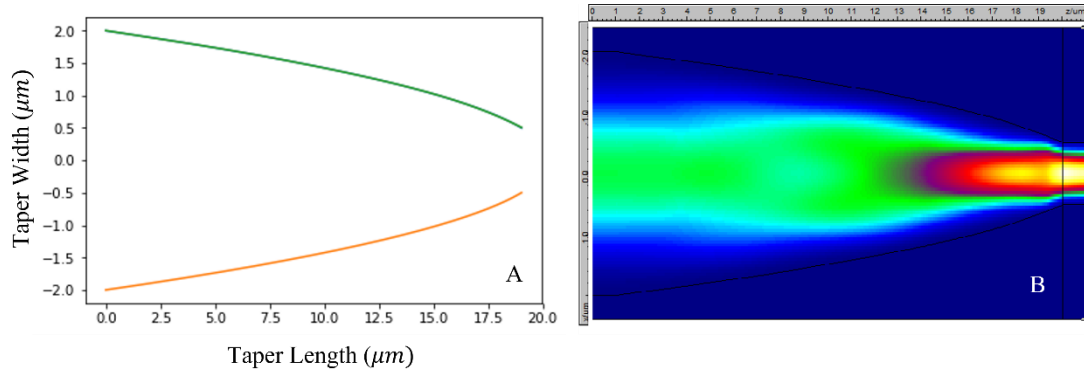
Figure 5.5: (A): xz plane view of designed GaAs/AlGaAs taper for $\alpha = 1$ and wavelength of 1.3 μm. (B): Intensity profile along z-direction calculated by Fimmprop (eigenmode expansion).

Figure 5.6-A shows the simulated power output of tapers designed with different values of the adiabaticity coefficient α, and demonstrates that for non-adiabatic tapers with $\alpha > 1.2,$ there is a strong dependence of the taper efficiency on the adiabaticity coefficient. For $\alpha > 1.2$ (equivalent to taper length shorter than 16 μm and coupling efficiency of 99.2%), losses become higher and the taper is no longer adiabatic. It is interesting to note that the efficiency of the tapers starts to level off for values of the adiabaticity coefficient $\alpha = 1.2$, which is still non-adiabatic. The relation between adiabaticity coefficient, output power and power fluctuation of the fundamental mode is shown in Figure 5.6-A where a negative correlation between α and the fluctuation is clear. Also, the adiabaticity of the final designs was checked. Adiabatic tapers should display no transfer of energy between the different optical modes. In the simulations, it is simple to check how much energy is stored in each mode, and therefore I have another measure of the adiabaticity of the final design. What was found is that even tapers that have adiabaticity coefficients $\alpha < 1$ can still display a small transfer of energy out of the fundamental mode. For example, Figure 5.6-B shows the proportion of energy in the fundamental mode along the length of the taper for a design with $\alpha = 0.2$. The energy in the fundamental mode can be seen to oscillate between the value of 1 and 0.9975, meaning that approximately 0.25% of the energy is transferred into higher modes. Figure 5.6-C clarifies the situation of a taper with $\alpha = 2$ and length of 9 μm where the fundamental mode does not have sufficient propagation distance to restore the exchanged power (24.7 %) with the higher mode and hence a high loss results.
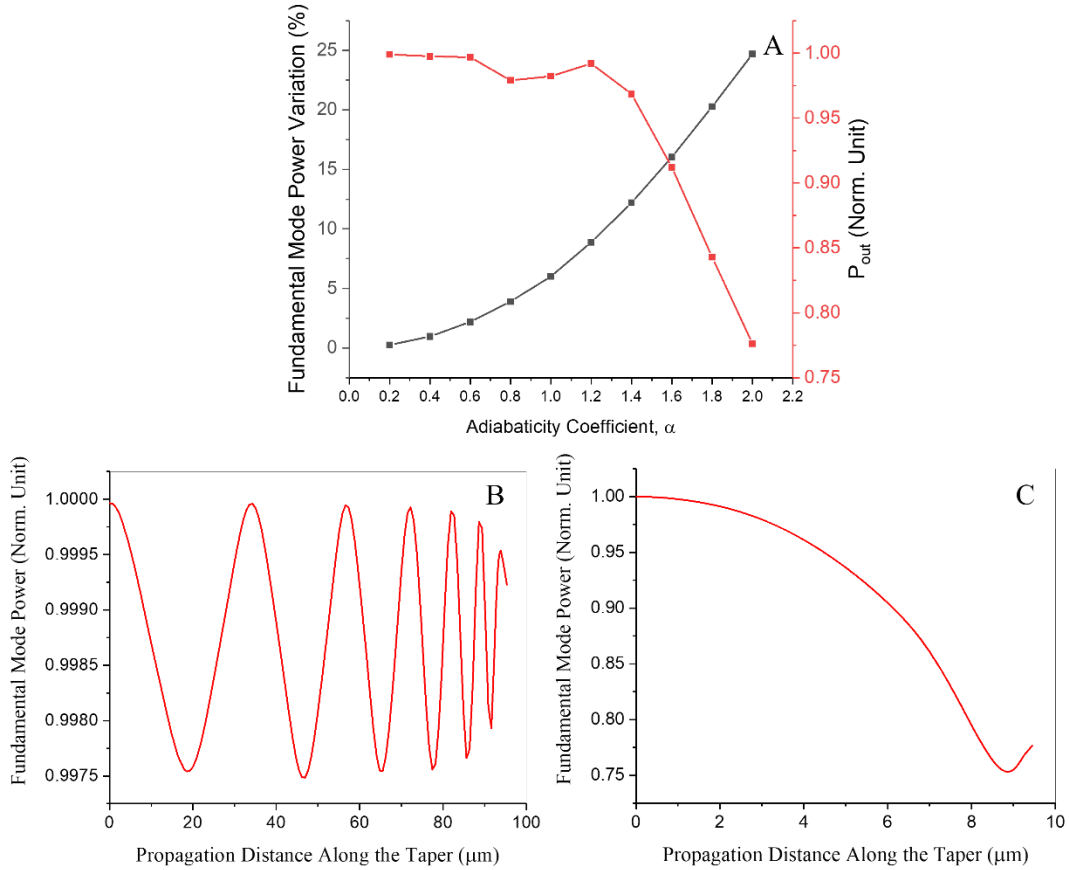
Figure 5.6: (A) Fimmprop (eigenmode expansion) results of fundamental mode power variation and efficiency for GaAs/AlGaAs adiabatic taper designs of different adiabaticity according to equation (5.3) where $\alpha = 0.2$ to 2 and $\lambda = 1.3$ μm. Fundamental mode power along designed taper of (B) high adiabaticity ($\alpha = 0.2$) and (C) low adiabaticity ($\alpha = 2$).

5.3.5   Linear Taper

As a comparison to the adiabatically designed taper above, linear tapers of the same length for each value of α were calculated. The efficiency of a linear taper as a function of its length between a starting waveguide width of $W_0 = 4$ μm and an end waveguide of width $W_L = 1$ μm is summarised in Figure 5.7. For example, the linear taper of length ~27 µm (a constant $\theta = 3.2°$) has the same length as the adiabatic taper of α = 0.7, and it has an efficiency of 98.4%. This linear taper has an adiabaticity coefficient $\alpha(z)$ that varies along its length.
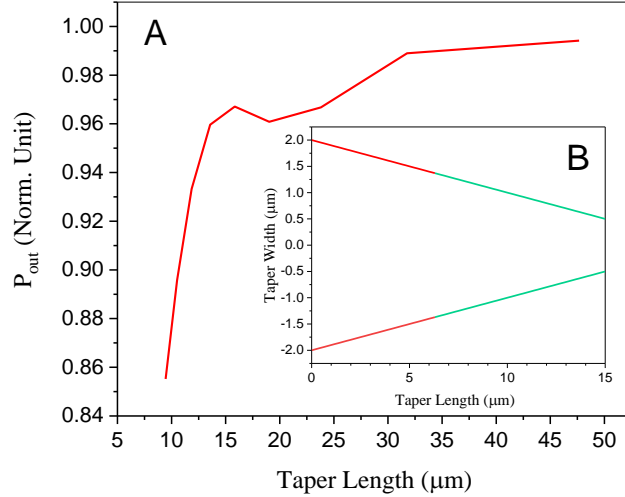
Figure 5.7: Relation between GaAs/AlGaAs linear taper length and its efficiency as obtained by Fimmprop (eigenmode expansion) at $\lambda = 1.3$ μm. (B) A schematic of linear taper of 15 μm length is shown. Red indicates non-adiabatic portions ($\alpha > 1$) and green adiabatic ($\alpha < 1$).

5.3.6   Exponential Taper

Optimizing a taper based on the geometrical design rule in equation (5.6), several values (L, a) correspond to different tapers with different efficiencies. For lengths extending from 5 µm to 20 µm, $W_0 = 4$μm and $W_L = 1$μm, the exponent a can be optimised to find the best shape. From the data in Figure 5.8, the relation between the output power and (L, a) clarifies that longer (adiabatic) tapers have better performance while at short lengths tapers show poor functionalities for all shapes (all a values). Nonetheless, the best tapers can be optimised at relatively short lengths (~16 µm) with length tolerance of ±2 µm. The behaviour of the fundamental mode power along the taper is tracked in Figure 5.9 for various shapes at the same length, ~16 µm. The taper of $a = 0.2$ has abrupt change at the end of the taper. Due to the dramatic decrease in the effective index value, there is high power loss whereas the optimum design $a = 0.65$ enhances the mode to restore about 8% of its power before the taper end. In contrast to the optimum taper, taper design of a $= 2$ is not wide enough to support interference between mode 1 and other modes so that the power is not restored by the taper end.
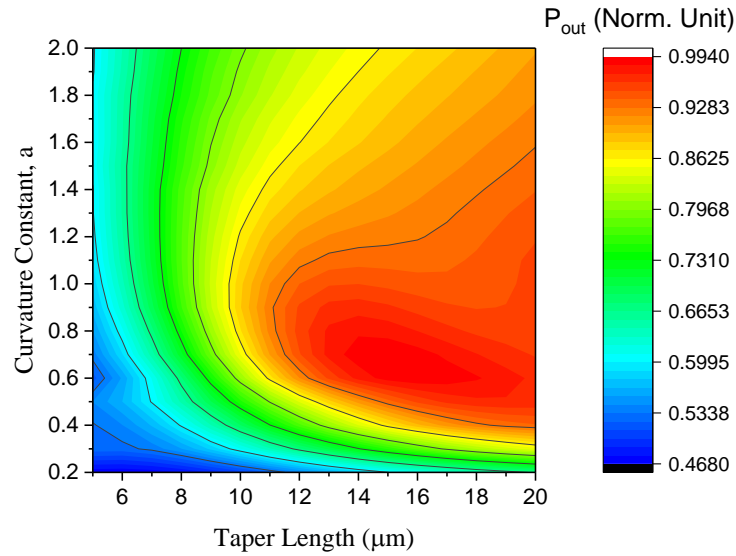
Figure 5.8: Fimmprop (eigenmode expansion) simulation results of GaAs/AlGaAs taper optimisation based on curvature constant for taper length from 5 μm to 20 μm at $\lambda = 1.3$ μm.
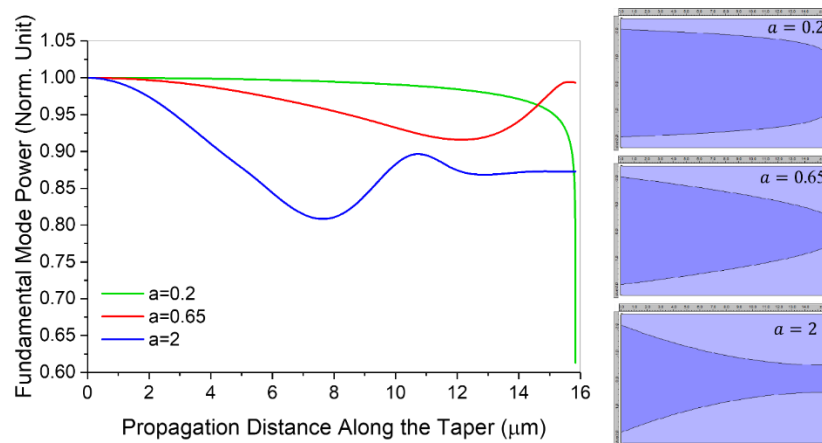
Figure 5.9: Fundamental mode power along GaAs/AlGaAs exponential tapers of various geometries calculated by Fimmprop (eigenmode expansion) at $\lambda = 1.3$ μm.

5.3.7   Length Comparison Between the Three Shapes

After studying the optimisation of the different kinds of taper, the efficiency of coupling light as function of length and the tolerance to changes in dimension, typical in fabrication, will be compared. Figure 5.10 illustrates the impact of taper lengths on the output power. The results presented here are generally similar to the outcomes of [3]: toward adiabaticity (longer tapers) the coupling efficiency is better while compact tapers need careful design to have good output. Additionally, the most interesting

aspect of Figure 5.10 is that compact, (~16 µm) well designed tapers (based on adiabaticity coefficient or curvature constant) can lead to better performance than linear tapers. Furthermore, the designed tapers can have length 1/3 of the linear taper of the same efficiency. In addition to compactness, there is another significant characteristic which is stability against some unintentional changes that may occur during manufacture. Unlike references [77]–[86], the response to some variations like waveguide width, etching depth and operating wavelength will be considered in the next section.
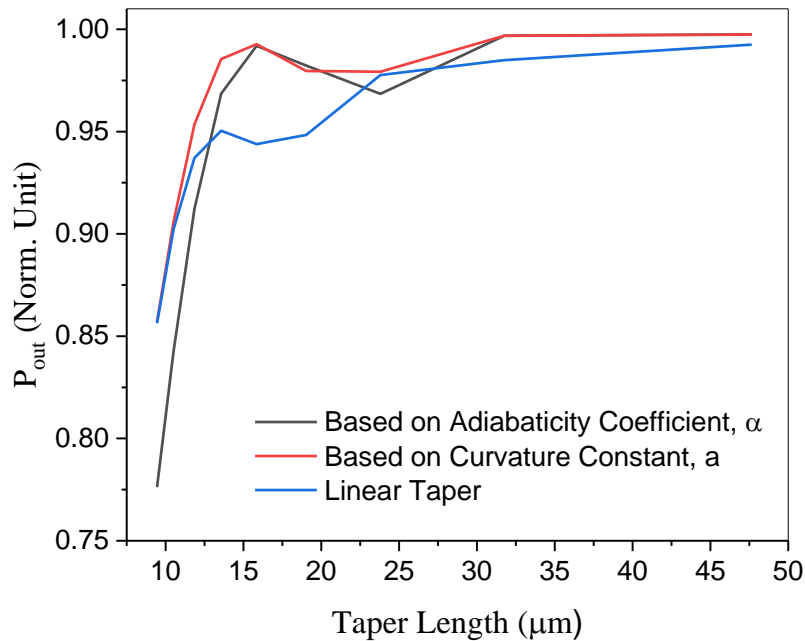
Figure 5.10: Coupling efficiency of different GaAs/AlGaAs taper types calculated by Fimmprop (eigenmode expansion) at $\lambda = 1.3$ µm.

5.4   Tolerance Analysis

In this part we describe the change in performance with variations in depth of the ridge and operating wavelength as may result from unintended variations in fabrication or simply because a wide operating wavelength range (bandwidth) is required.

5.4.8   Width Tolerance

For unintentional width variation within range of $\pm 0.1 \ \mu m$, the three types have similar response with output variation less than 0.33 %. So, tapers have good stability under waveguide width variations. Figure 5.11 shows the tapers behaviour over fabrication width variations.
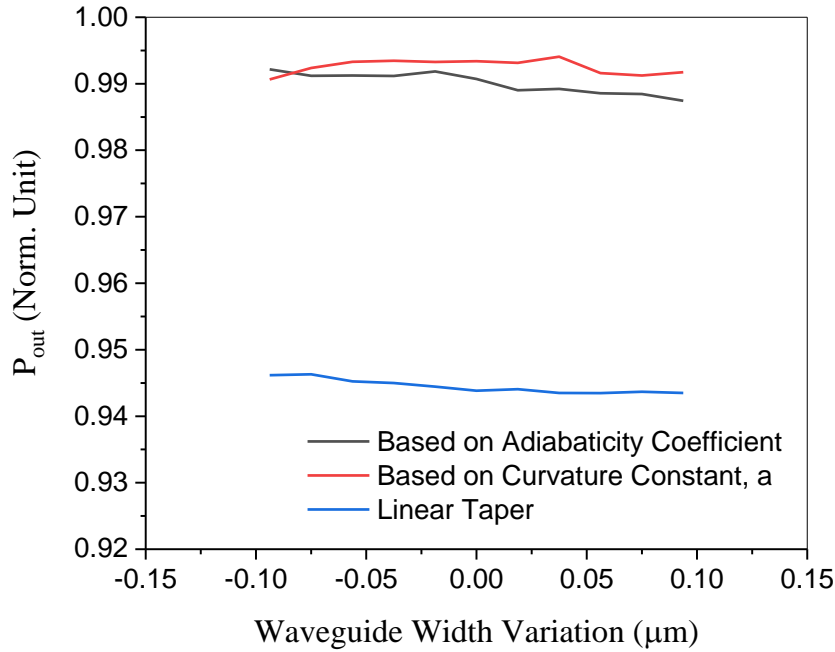
Figure 5.11: Waveguide width variation impact on GaAs/AlGaAs taper efficiency calculated by Fimmprop (eigenmode expansion) at $\lambda = 1.3 \ \mu m.$

5.4.9   Etching Depth Tolerance

The tolerance with respect to fabrication deviation in the etching depth used to create the waveguide is studied. Etching depth is one of the most difficult dimensions to control in fabrication and we examine the efficiency of the three shapes for variations of $\pm 0.1 \ \mu m$ above and below an optimum depth at the same length (~16 μm). The optimum etching depth is at the core/lower cladding interface. Figure 5.12 demonstrates a major difference between the adiabaticity based designed taper and the other tapers. The output power of the linear and curvature based designed tapers varies more significantly at deeper etching level. The output power of the

adiabaticity based designed taper varies in a similar manner with a small reduction of approximately 0.4 % to 0.6 % in output power with increasing depth of 0.1 µm. For shallower depths than the optimum, reduction in output power is ~ 0.2 % for the linear taper which means better stability than that of the designed tapers.
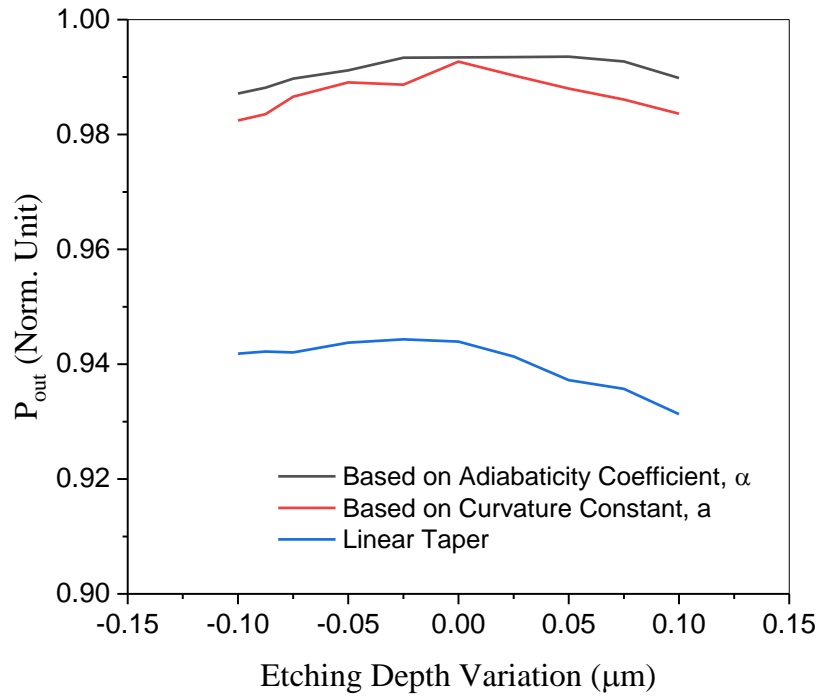
Figure 5.12: Etching depth tolerance of different GaAs/AlGaAs tapers calculated by Fimmprop (eigenmode expansion) at $\lambda = 1.3 \, \mu m$.

5.5   Wavelength Response

The spectral response (where both waveguide and material overall response are considered) of the three types of tapers are compared in Figure 5.13 at the same length (~16 µm). Over a range of 0.2 µm, it is noticeable that the designed tapers maintain good stability (with less than 0.6 % reduction in output power) in comparison with the linear taper which shows relatively larger variation and an output power that increases as the operating wavelength increases. This reflects the fact that at 1.3 µm wavelength, a linear taper of length of ~16 µm is not optimised.
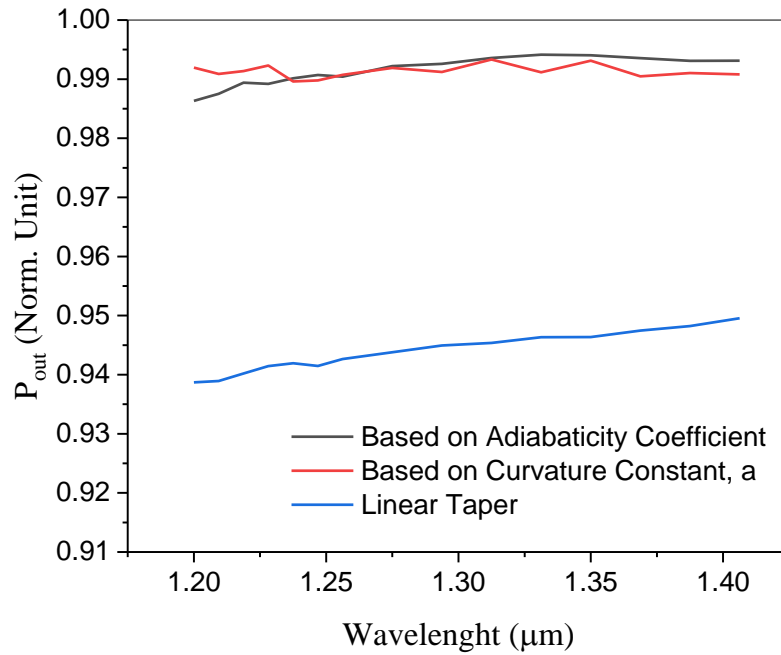
Figure 5.13: Spectral response of designed and linear GaAs/AlGaAs tapers calculated by Fimmprop (eigenmode expansion) at $\lambda = 1.3 \, \mu m$.

5.6 Conclusion

GaAs/AlGaAs based waveguide tapers designed using one of two rules have been compared to a simple linear taper based on achievable footprint, variations in depth as typically occurs in fabrication and operating wavelength. Small footprint tapers with high power transfer efficiency have been simulated. Short tapers of length ~16 µm, while also achieving a tolerance to waveguide width and etching depth variation ~±0.1 µm with a power transfer reduction of up to ~1% and variation of order 1% in the power output over wavelength range from 1.2 µm to 1.4 µm can be achieved using the adiabaticity or exponential design rule. The designed tapers are preferred due to their compactness and high performance. They can be employed to transfer signals between circuit elements especially in the case of big mismatch.

In this chapter, two tapers design rules were applied to ridge waveguides and compared to a conventional linear taper in some aspects like taper length, fabrication variations and bandwidth response. In the following chapter, two types of ridge waveguide based multimode interferometers (conventional and tapered) are investigated

Chapter 6 :

Design and Optimisation of MultiMode Interference (MMI) Splitters

In this chapter, compact, high efficiency GaAs/AlGaAs based deep etched 1×2 multimode interferometers (1×2 MMIs) will be optimised for 50/50 splitting functionality at an operating wavelength of 1.3 µm. The performance of two configurations, conventional and tapered, of symmetrical splitters will be investigated under variations typical of those found in fabrication and as a function of operating wavelength. The relation between the MMI width and length will be demonstrated, and tolerances of both conventional and tapered devices are studied at width of 6 µm.

6.1   Background

Various waveguide configurations are developed in integrated photonics to manipulate light signals during on-chip operation. Power splitting is one of the basic functionalities needed in controlling light. A power splitter will take a signal in one branch or waveguide and split the power into two or more branches or waveguides. Power splitters are classified by the number of input and output branches and the ratio of powers; for example, a typical use would be the 1×2 50/50 power splitter. Power splitters can have various designs such as Y-branches or multimode interferometers – this chapter looks at using a multimode interferometer to design a 1×2 50/50 power splitter.

Multimode interferometers (MMIs) are a fundamental component of integrated photonics that work by processing light based on the principle of self-imaging. Different configurations of MMI are widely used in photonic applications for several purposes. Based on functionality, MMI type and self-imaging mechanism are chosen. For example, an MMI can be used as 3 dB coupler [93], mode/wavelength (de)multiplexer [94], [95] or directional coupler [96]. Single or multiple input/output waveguide MMIs are designed to split, filter or combine light [97]. Designs are controlled by an operating wavelength, λ, and waveguide structure and geometry. Therefore, careful designs need to be set for certain set of conditions for a chosen functionality. For splitting functionality, an MMI can be designed as $1 \times N$ ports and for equal power division, central feeding is needed at the input and equally spaced N ports at the output at the N-fold self-image locations.

The simplest non-trivial MMI is a 1×2 splitter consisting of three sections – input waveguide, multimode waveguide and two output waveguides (Figure 6.1-A). For a symmetrical 1×2 multimode interferometer, the multimode waveguide is designed to support at least three modes (to assure two symmetrical modes are excited) to generate N-fold images of an input field [98] , while the input and output are usually selected to be single mode waveguides. When equal splitting is desired, the whole structure should be symmetric; the input waveguide is in the centre of the multimode section and the output waveguides are equidistant from the centre (and usually far enough apart that the individual waveguide modes do not overlap/interact). Also, tapers can be added in between input/output ports and the multimode section to improve coupling/efficiency (Figure 6.1-B).
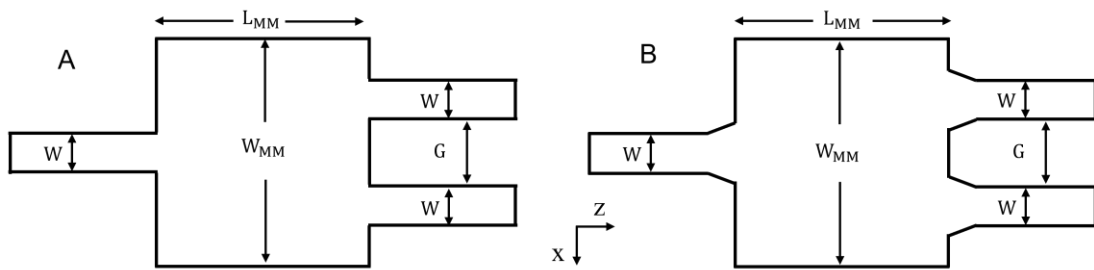
Figure 6.1: 1×2 MMI (A) conventional, (B) tapered. w is input/output single mode width, W_{MM} is multimode waveguide width, L_{MM} is multimode waveguide length and G is the gap between output ports.

As reported in [99], "self-imaging is a property of multimode waveguides by which an input field profile is reproduced in single or multiple images at periodic intervals along the propagation direction of the guide". Efficient MMI's are realised if three conditions are satisfied:

1- The waveguide supports enough modes (that could be different depending on functionality – in general, more splitting will require more modes). Thus, wide waveguides are required to be used in the central section, as wider waveguides support more modes.

2- There is a large step index that offers high confinement.

3- Small input waveguide, single mode, to reduce the radiation resulting from higher mode excitation.
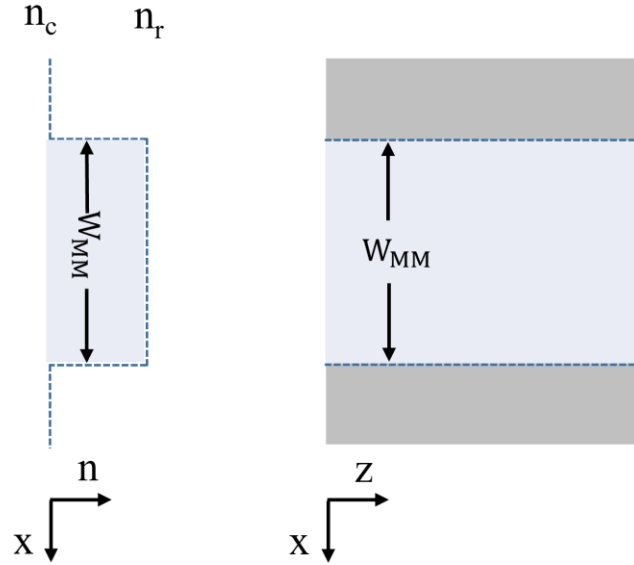
Figure 6.2: A ridge, step-index multimode waveguide refractive index profile, n(x). n_r is ridge effective refractive index and n_c is cladding effective refractive index. $n_r > n_c$, z is propagation direction and device width is in x direction.

A ridge, step-index multimode waveguide is shown in Figure 6.2. W_{MM} is the width of the multimode waveguide, n_r and n_c are ridge and cladding effective refractive indices, respectively. At a free-space wavelength λ, a number of lateral modes, m, are supported including mode numbers $v = 0,1,..(m-1)$. Following the approach given in [99], the symmetric 1×2 MMI will be analysed. The lateral wave number along x is given by

$$k_{v,x} = \frac{(v+1)\pi}{(W_{eff})_v} \tag{6.1}$$

W_{eff} is the effective width of the waveguide which includes physical width of the multimode waveguide W_{MM} and the penetration of the fields into the waveguide cladding (i.e. the evanescent fields due to the Goos-Hanchen shift [100]). W_{eff} is therefore polarisation-dependant. Generally, the effective widths W_{eff} of higher modes approximate the effective width of the fundamental mode (Figure 6.3) and will be denoted by W_e. Where σ is a constant equal to 0 for TE modes and 1 for TM modes,

$$W_e \cong W_{MM} + \left(\frac{\lambda}{\pi}\right)\left(\frac{n_c}{n_r}\right)^{2\sigma}(n_r^2 - n_c^2)^{-1/2} \tag{6.2}$$
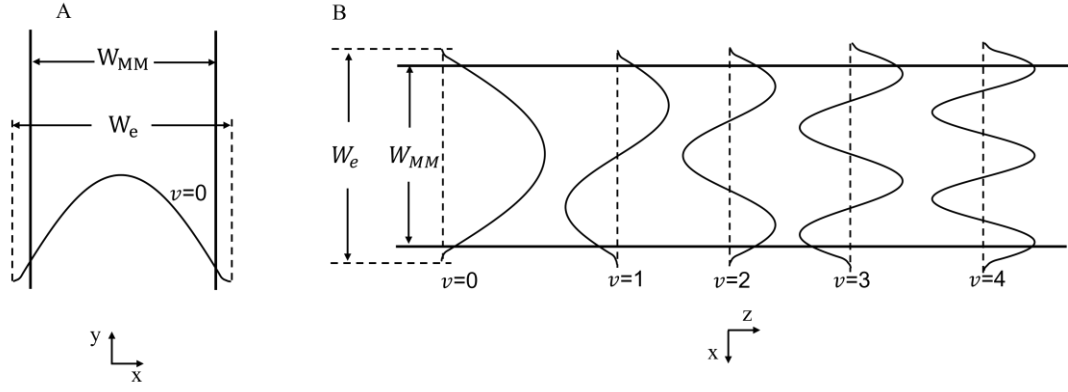
Figure 6.3: The multimode waveguide effective width W_e (A) in xy plane and (B) in xz plane of modes $\nu = 0, 1, 2, 3, 4$. x is horizontal direction of the waveguide, y is vertical direction across the structure layers and z is the propagation direction of the light.

The input field $\Psi(x, 0)$ is injected in the multimode waveguide at $z = 0$ is completely enclosed within the width W_e and distributed into all modal fields $\psi_\nu(x)$ that can be guided by the multimode waveguide. Since the input field is fed by single mode waveguide, its size is small sufficient to not excite radiation modes. Hence,

$$\Psi(x, 0) = \sum_{\nu=0}^{m-1} c_\nu \psi_\nu(x) \tag{6.3}$$

Where the field amplitude c_ν is found by overlap integrals (6.3) taking the mode orthogonality in consideration.

$$c_\nu = \frac{\int \Psi(x, 0) \psi_\nu(x) dx}{\sqrt{\int \psi_\nu^2(x) dx}} \tag{6.4}$$

At distance z from the input point, the field profile is expressed as the superposition of all the supported mode profiles

$$\Psi(x, z) = \sum_{\nu=0}^{m-1} c_\nu \psi_\nu(x) \, exp\,(-i\beta_\nu z) \tag{6.5}$$

Taking the fundamental phase $exp\,(-i\beta_0 z)$ as common factor and dropping it:

$$\Psi(x, z) = \sum_{\nu=0}^{m-1} c_\nu \psi_\nu(x) \, exp[i(\beta_0 - \beta_\nu)z] \tag{6.6}$$

Equation (6.6) satisfies the wave equation (6.7)

$$\frac{\partial^2 \Psi}{\partial x^2} + \frac{\partial^2 \Psi}{\partial z^2} + k_0^2 n_r^2 \Psi = 0 \qquad (6.7)$$

Where $k_0 = \frac{2\pi}{\lambda_0}$. The derivative in the first term gives $-k_{i,x}^2$ and in the second term equals $-\beta_v^2$. Hence, the solution of equation (6.7) represents the dispersion equation

$$k_{v,x}^2 + \beta_v^2 = k_0^2 n_r^2 \qquad (6.8)$$

which describes the relation between the modal lateral wavenumber k_v, the modal propagation constant β_v and the ridge index n_r:

$$\beta_v = \sqrt{k_0^2 n_r^2 - k_{v,x}^2} \qquad (6.9)$$

Comparing $n_r^2 k_0^2$ with k_v^2, one can finds that $k_0^2 n_r^2 \gg k_{v,x}^2$, then,

$$\beta_v = k_0 n_r \sqrt{1 - \frac{k_{v,x}^2}{k_0^2 n_r^2}} \qquad (6.10)$$

Using the binomial expansion $(1-x)^n = 1 - nx$, equation (6.10) becomes

$$\beta_v \cong k_0 n_r - \frac{k_{v,x}^2}{2 k_0 n_r} \qquad (6.111)$$

Now, substituting $k_0 = \frac{2\pi}{\lambda}$ and $k_{v,x} = \frac{(v+1)\pi}{W_e}$ where $W_{eff} \cong W_e$ in equation (6.11), we get

$$\beta_v \cong k_0 n_r - \frac{(v+1)^2 \pi \lambda}{4 n_r W_e^2} \qquad (6.12)$$

The propagation constants spacing $\beta_0 - \beta_v$ is

$$\beta_0 - \beta_v \cong \frac{v(v+2)\pi\lambda}{4 n_r W_e^2} \qquad (6.13)$$

So, the propagation constants spacing between the two lowest-order modes $\beta_0 - \beta_1$ is

$$\beta_0 - \beta_1 \cong \frac{3\pi\lambda}{4 n_r W_e^2} \qquad (6.14)$$

Where the beat length between β_0 and β_1 is

$$L_\pi = \frac{4n_r W_e^2}{3\lambda} \qquad (6.15)$$

And then equation (6.13) becomes

$$\beta_0 - \beta_v \cong \frac{v(v+2)\pi}{3L_\pi} \qquad (6.162)$$

Hence, the field at distance L , $\Psi(x,L)$ can be written by substituting (6.16) into (6.6)

$$\Psi(x,L) = \sum_{v=0}^{m-1} c_v \psi_v(x)\, exp\left[i\left(\frac{v(v+2)\pi}{3L_\pi}\right)L\right] \qquad (6.17)$$

Based on the self-imaging principle, there are certain proper lengths L_{MM} at which the constructive interference patterns are obtained with multiple or single replica. In the case of symmetric interference [4] for $1 \times N$ MMI, $c_v = 0$ for antisymmetric modes, $v = 1,3,5,..$, and the length of the multimode section, L_{MM}, can be chosen to match the shortest length at the N-fold images [99].

$$L_{MM} = \frac{p}{N}\left(\frac{3L_\pi}{4}\right) \qquad (6.18)$$

Where $p \geq 0$, $N \geq 1$ are integers with no common divisors. p represents the imaging periodicity along the multimode waveguide. The N-fold images are equally spaced and symmetrically located at $\approx \pm\frac{W_e}{N}$.

6.2   Methodology

A 1×2 MMI was designed, based on a single mode input, a multimode waveguide and two identical single mode output waveguides made of GaAs/AlGaAs structure. To study a small footprint device, a width of 6 µm was chosen for the multimode waveguide. This width allows the gap (G in Figure 6.1) in between the output waveguides to be achievable within fabrication limits and sufficient to prevent coupling between the output ports. The spacing between the outputs was approximated by $\pm\frac{W_{MM}}{N}$. Meanwhile, the length of the multimode waveguide was optimised for

---

[4] The symmetric interference can be obtained by centre-feeding the multimode waveguide at $\frac{W_{MM}}{2}$ with symmetric field profile.

width of 6 μm and it was found that two-fold image formation of the input is located at 46.5 μm. For the tapered device, the tapers were optimised to connect single mode input/output ports to the multimode waveguide. The taper width changes from single mode width to 2.5 μm at the input and vice versa at the output. Table 6.1 provides information about the device parameters.

Table 6.1: 1×2 MMI parameters.

Parameter	Value
Input/output type	Single mode waveguide
Multimode width	6 μm
Multimode length	46.5 μm
Taper width	Single mode ↔2.5 μm
Etching depth	Core-lower cladding interface
Wavelength	1.3 μm

Before further simulations were carried out, the software parameters were tested to confirm the convergence as described in Chapter 2 (Methodology). Namely, the calculation window width (the height was optimised on the level of (1D) slab waveguide in Chapter 3), maximum number of calculation modes[5] included in the calculations, the mesh number in both direction of the waveguide cross-section and the taper algorithm parameters for the tapered 1×2 MMI version. These parameters were chosen to ensure sufficient accuracy and reasonable calculation time. First, the calculation width was increased until the output power converged. The calculation width was chosen to guarantee widths greater than $W_e = W_{MM} + 0.31\ \mu m$. For example, a calculation width of $W_{MM} + 2\ \mu m$ corresponds to error about 1.6%. (Figure 6.4) After that, the number of modes was adjusted to find the convergence. From Figure 6.5, it is clear that the transmission values converge if 11 modes or more are included in the calculations with error of 0.2% or less. Then, number of mesh cells

---

[5] This is software parameter define number of modes to be calculated and differ from waveguide supported modes.

was set similar to that used in Chapter 3 for ridge waveguides. Taper algorithm parameters are chosen based on what was found in Chapter 5 for the tapered 1×2 MMI.
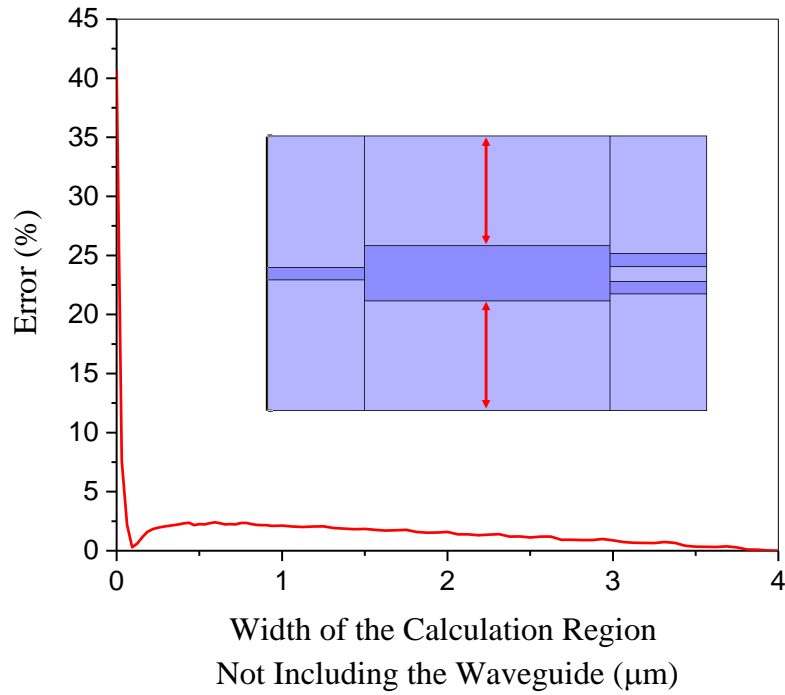
Figure 6.4: Transmission error as function of the calculation boundary distance measured from the multimode waveguide edge.
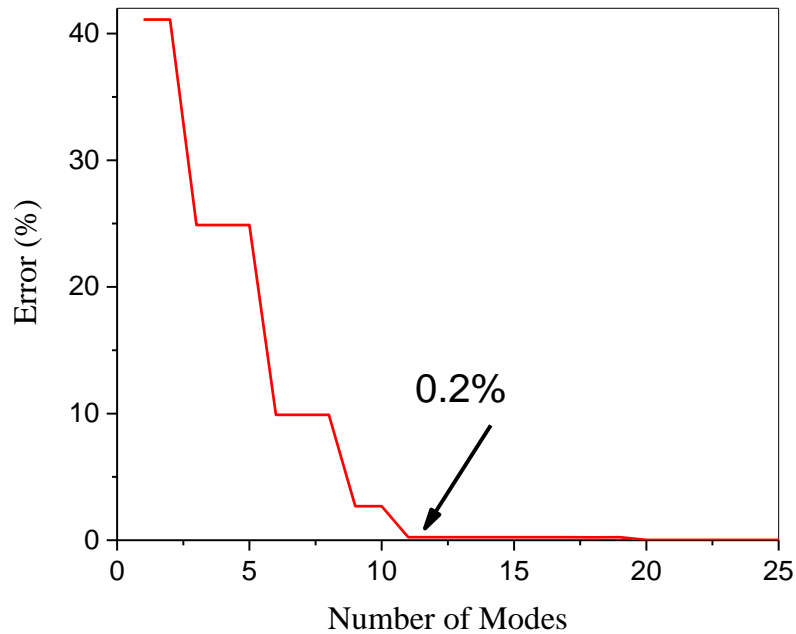
Figure 6.5: Calculation accuracy as function of number of modes included in calculation.

After the software was set up to reasonable accuracy, the device optimisation, tolerances and performance were investigated as discussed in the following sections.

6.3   Optimisation

6.3.1   Multimode Waveguides

The widths of the MMIs were chosen accordingly. Practically, the output ports' width and the spacing between them needed to be considered to choose a proper width W_{MM}. Figure 6.6 presents the effective indices of supported modes for different widths: 4-10 µm. A width of 6 µm is chosen to build the design in the following section. This width choice is wide enough to meet fabrication limitations and guarantees balanced splitting functionality by siting the outputs, so the gap is sufficient to prevent the output waveguides coupling.
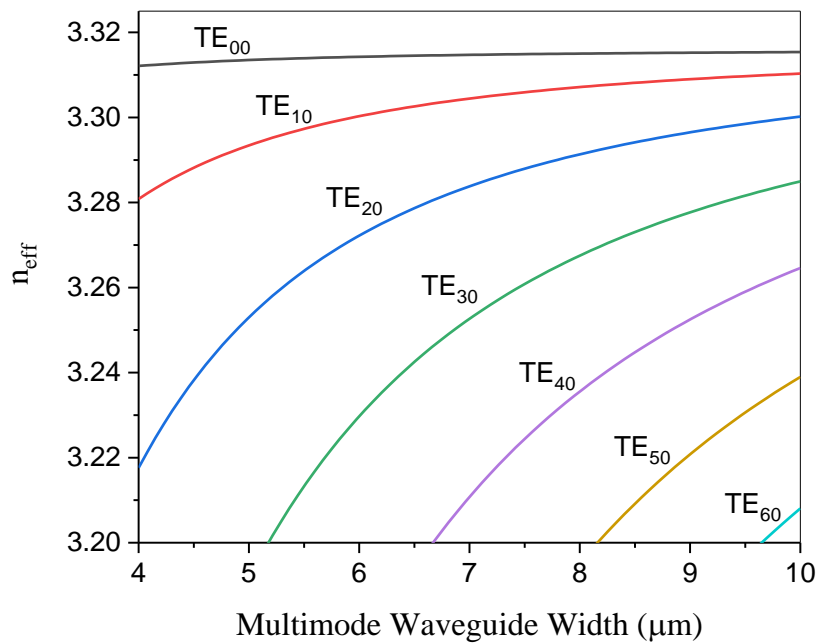
Figure 6.6: Effective indices of symmetrical modes for GaAs/AlGaAs waveguide widths from 4 to 10 µm calculated by Fimmwave FDM solver at $\lambda = 1.3$ µm.

6.3.2 Length and Width Optimisation

Both conventional and tapered 1×2 MMIs were studied over a range of widths from 4 µm to 10 µm to discover the proper lengths at which the two-fold images are formed. Figure 6.7 shows the efficiency of two configuration of 1×2 MMI as function of both width and length of the device. It is noticeable that the two-fold image formation at a certain MMI width can be obtained at several lengths (as seen in the optimisation of width and length Figure 6.7, intensity of interference pattern in Figure 6.8) and they are similar for both conventional and tapered devices. However, it is clear that the tapered device shows better tolerances. For a 1×2 MMI of width 6 µm, the proper lengths for 1,2 and 3-fold image locations are displayed in Figure 6.8. The first two-fold imaging is located at 46.5 µm as found by simulation while the approximation gives $L_{MM} = 50.8\ \mu m$. So, the difference between the simulation and approximation is more than 4 µm and will be discussed in section 6.4.1.
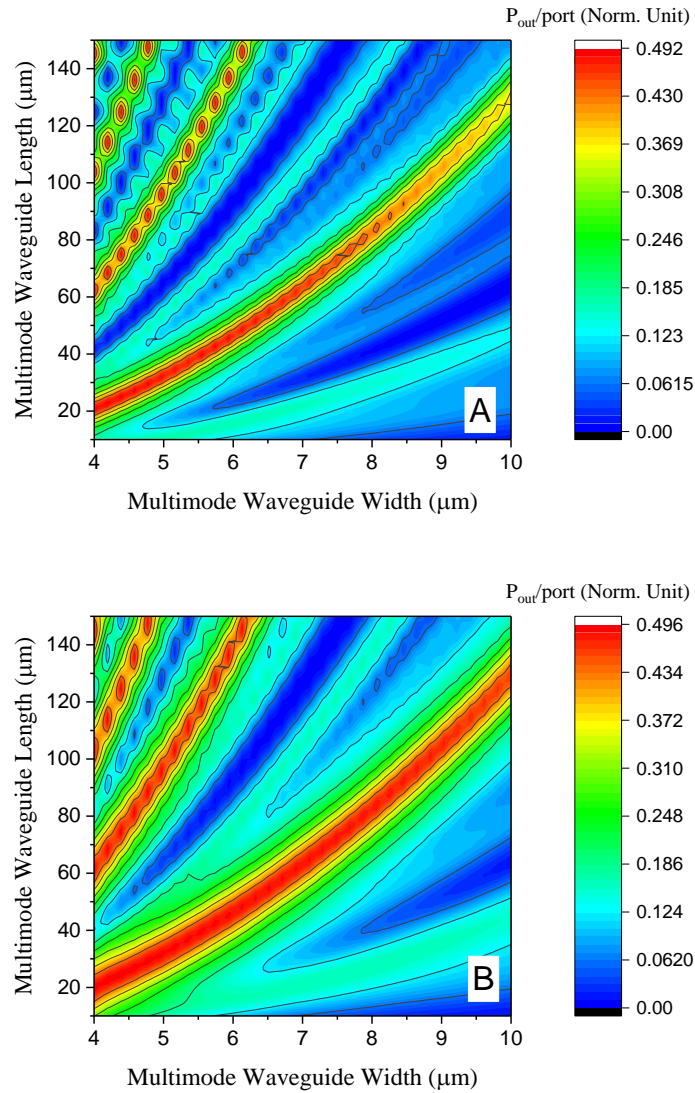
Figure 6.7: Optimum dimensions (width and length) of GaAs/AlGaAs (A) conventional and (B) tapered 1×2 MMI at $\lambda = 1.3$ μm as found by Fimmprop (eigenmode expansion). For a certain MMI width, the two-fold image formation can be obtained at different lengths.

Figure 6.8 shows intensity profile of interference pattern of various image formation for 6 μm wide MMI. A single image of the input field is located at the centre of the MMI and can be reproduced along the device. The two-fold images are formed at half the distance between the input and its first single image. It is clear that the 6 μm is sufficient to see the three-fold and four-fold images and the pattern is repeated along the device.
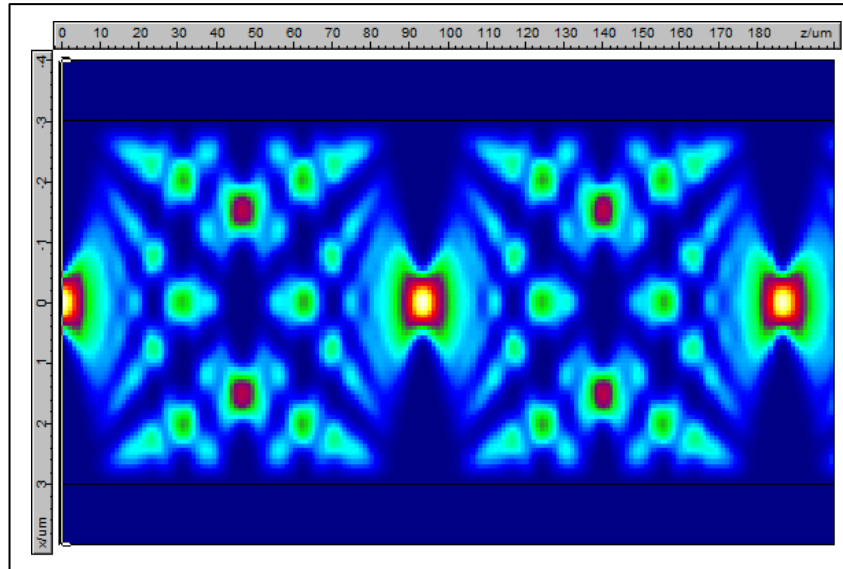
Figure 6.8: Intensity profile of 6 μm wide GaAs/AlGaAs 1×2 MMI found by Fimmprop (eigenmode expansion) at $\lambda = 1.3$ μm. First two-fold image formation can be seen at length of 46.5 μm and repeated ~ 140 μm.

6.4   Tolerance Analysis

The fabrication process is known to be associated with some defects that affect device efficiency. In the following parts the influence of geometrical fabrication errors on the device efficiency will be discussed for 1×2 MMI of width of 6 μm and length of the shortest optimum length (46.5 μm).

6.4.3   Multimode Waveguide Length and Width Tolerances

In Figure 6.9-A, the output power per output port is shown for lengths up to 100 μm. A power reduction of 10% is a consequence of ~$\pm 2 \ \mu m$ and ~$\pm 4.3 \ \mu m$ changes in the lengths of the conventional and tapered MMI lengths respectively for a 6 μm wide device. So, if the devices are designed based on the approximation, then 10% and 14% less output is expected for the tapered and conventional MMI than that of simulation based optimised ones. The tapered device shows better stability due to the role of the taper in reducing radiation at the different cross-sections between the input/output ports and the multimode waveguide. The two peaks around 16 μm and 78 μm corresponds to devices in Figure 6.9-B and Figure 6.9-C, respectively where

the collected power by the output ports is due to multi-fold images (could be three-fold images and five-fold images, respectively).
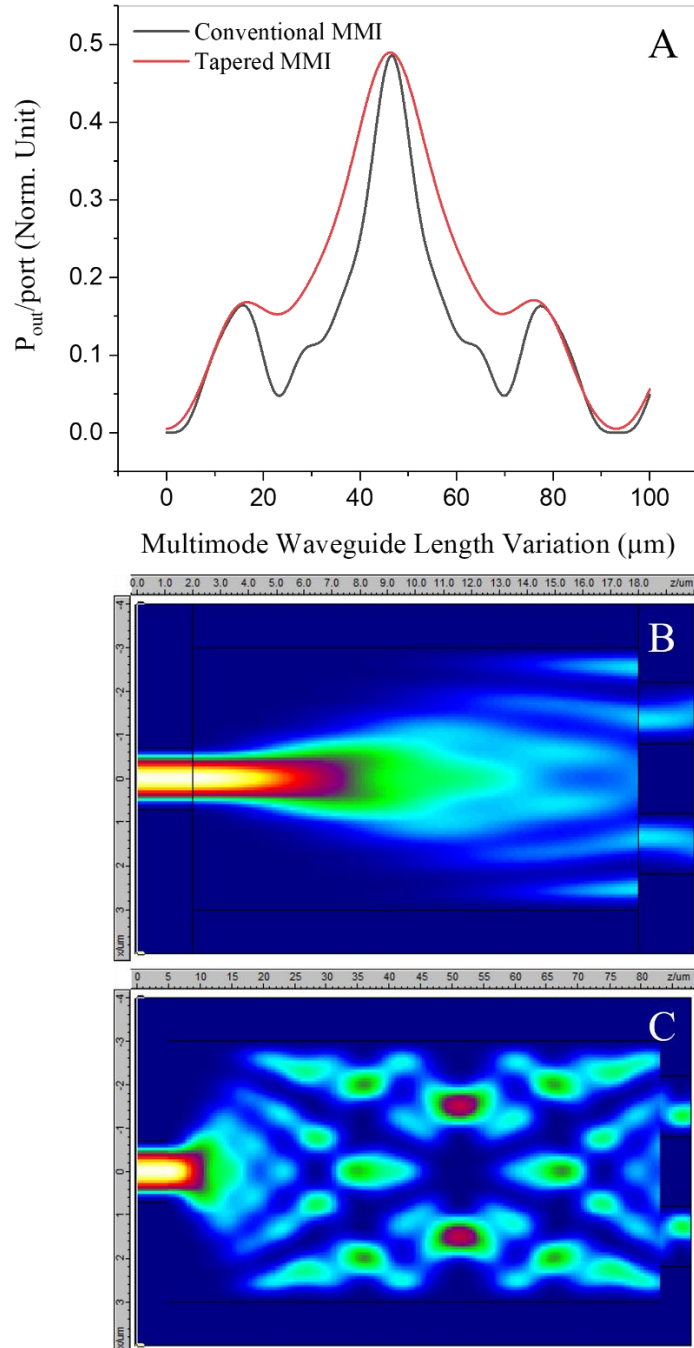
Figure 6.9: (A) Conventional and tapered GaAs/AlGaAs 1×2 MMI length tolerance at multimode waveguide width = 6 μm. The two peaks around of 1×2 MMI of lengths of (B) 16 μm and (C) 78 μm represent the power of other multi-fold image formation. Simulation was performed at $\lambda = 1.3$ μm by Fimmprop (eigenmode expansion).

A key factor for designing MMI's is the width of the device. Therefore, it is important to explore its impact on the performance. So, both conventional and tapered 6 µm wide 1×2 MMI at the shortest optimum length, 46.5 µm, were investigated. As seen in Figure 6.10 for the conventional 1×2 MMI with a width error of $\sim\pm0.1\ \mu m$, the output power per port is reduced by less than 2.9 % and it is slightly more sensitive to a reduction in width rather than an increment. On the other hand, the tapered device has higher stability so that a width error of $\sim\pm0.1\ \mu m$ leads to ~1 % output reduction.
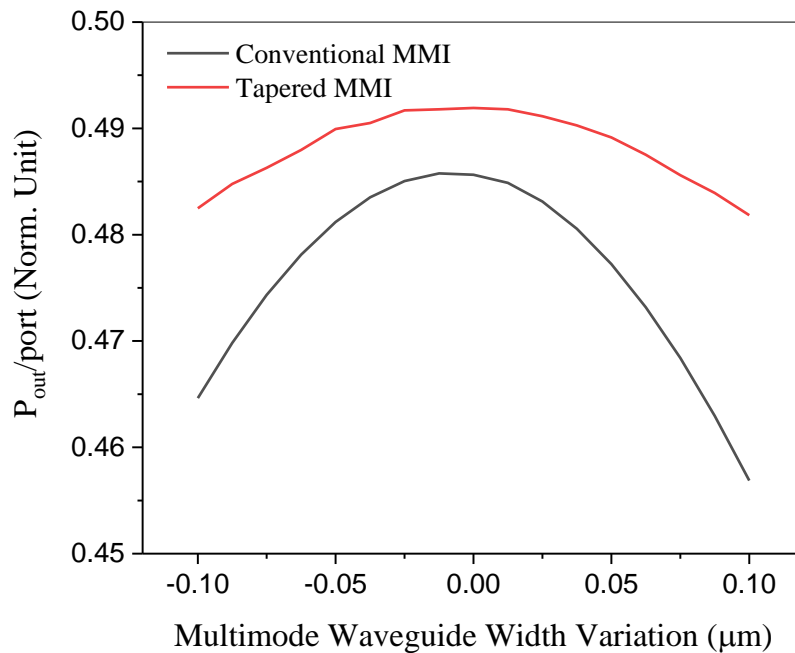
Figure 6.10: Fimmprop (eigenmode expansion) results of conventional and tapered width tolerance of GaAs/AlGaAs multimode waveguide width of 6 µm and the optimum length at $\lambda = 1.3\ \mu m$.

6.4.4 Input/Output Width Variations

The input/output waveguides were designed to be single mode waveguides, 1.4 µm wide, to deliver an input of a single TE mode at a wavelength of 1.3 µm. However, width deviations are common and can range up to 0.1 µm which would lead to higher order mode excitation. Therefore, the behaviour of two configurations was examined for input/output width change of ±0.1 µm. There is negative correlation between the waveguides width and output waveguide gap size G. So, the output

waveguide width error involves gap size variation of ∓ 0.1 μm as the output positions are determined by locating their centres at $\frac{W_{MM}}{4}$. So, the change in response is due to the output width and the gap size variation. Figure 6.11 demonstrates the change in output power per port as the input/output waveguides widths change. What is interesting in this graph is the output power increment as the width increases. Wider input/output waveguides lead to higher confinement of mode area and hence delivering higher output power. Nevertheless, widths leading to higher mode excitation are not preferable. Moreover, the input port needs to maintain single mode operation to provide stable distribution of the input field [101]. Additionally, wider outputs can lead to greater interaction between light in the two waveguides as the gap becomes smaller.
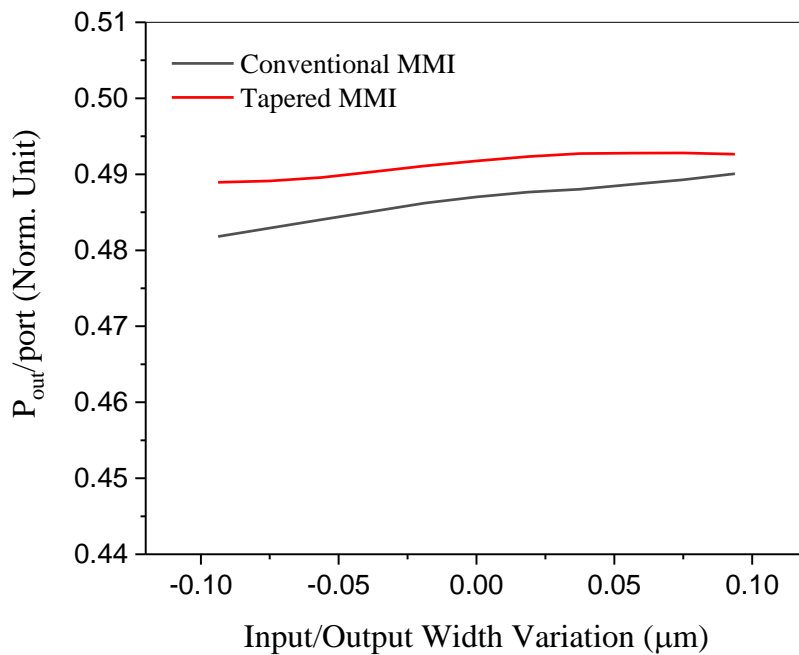
Figure 6.11: Input/output waveguides width fabrication error over range of ±0.1 μm for GaAs/AlGaAs conventional and tapered 1×2 MMI. Results are calculated at $\lambda = 1.3 \ \mu m$ by Fimmprop (eigenmode expansion).

6.4.5   Output Gap Size

The gap size was chosen to be $\frac{W_{MM}}{4}$ using the approximation $W_e \cong W_{MM}$ due to high confinement. Nonetheless, the final formation of this gap is affected by the fabrication error of the output waveguides. So, if each output waveguide suffers from error of ± 0.1 μm, hence the total change of the gap size will be ∓ 0.1 μm (∓ 0.05 μm from each waveguide). This change will cause output reduction of 1.5-2.5 % the conventional design and 1.3-0.7 % in tapered MMI efficiency (Figure 6.12).
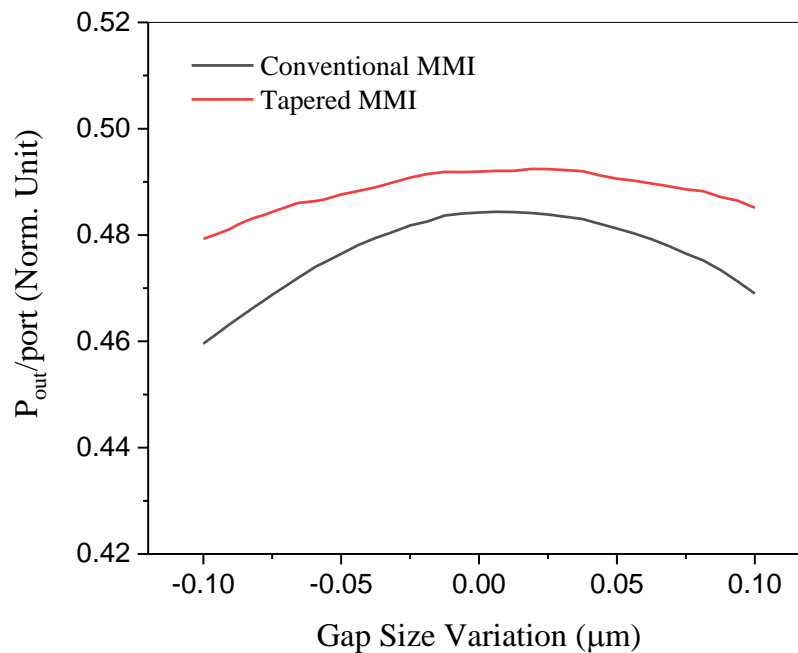
Figure 6.12: GaAs/AlGaAs conventional and tapered 1×2 MMI output gap size tolerance at multimode waveguide width = 6 μm and the optimum length. Results are calculated at $\lambda = 1.3$ μm by Fimmprop (eigenmode expansion).

6.4.6   Input Offset

The efficiency of the device was examined under input position deviation of 0.5 μm from the centre of the multimode waveguide. The results indicates that the efficiency of the device is considerably affected as the input port is shifted from the centre. From Figure 6.13, it can be seen that the efficiency of the conventional MMI

dramatically declines by more than 32% at deviation of 0.5 μm whereas the tapered device decreases steadily up to 15% of its maximum output power.
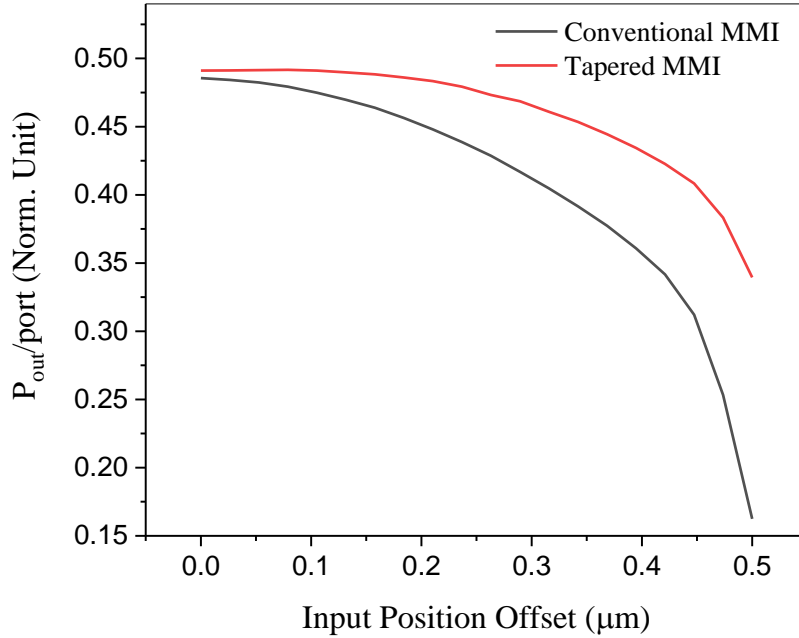
Figure 6.13: Input wavegude offset impact from the center of the multimode waveguide of GaAs/AlGaAs 1×2 MMI. Simulation is done at $\lambda = 1.3\ \mu m$ by Fimmprop (eigenmode expansion).

6.4.7   Etching Depth

Another of the expected errors related to fabrication is the etching depth. For both configurations efficiency was scanned over a range of $\sim \pm 0.1\ \mu m$ from the nominal etching depth. For etching 0.1 μm shallower than core-lower cladding interface there is power reduction of ~ 0.3 % for the conventional device and less than 0.1 % for tapered MMI (Figure 6.14).
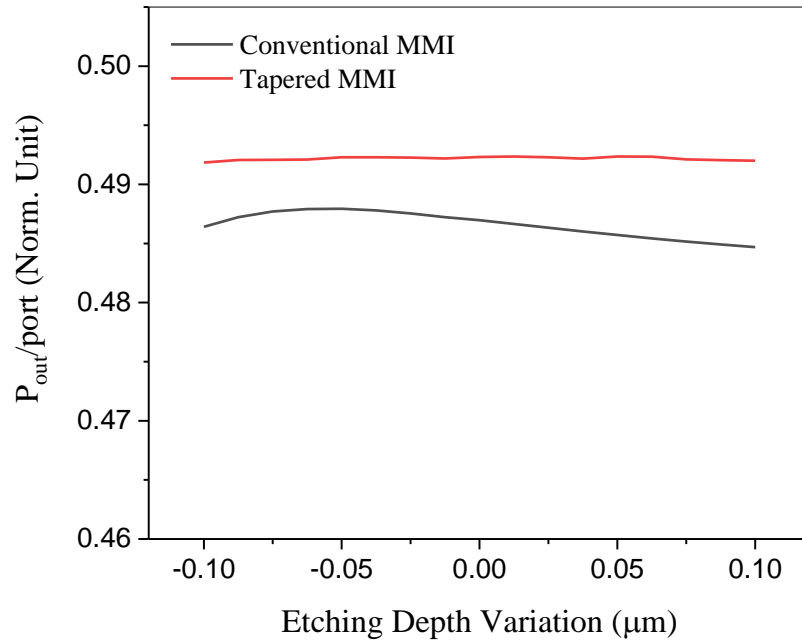
Figure 6.14: GaAs/AlGaAs conventional and tapered 1×2 MMI etching depth tolerance at multimode waveguide width = 6 μm, the optimum length and $\lambda = 1.3$ μ*m* as found by Fimmprop (eigenmode expansion).

.

6.5   Wavelength Response

According to relations (6.2) and (6.18), both length and width of 1×2 MMI is operating wavelength dependant. Referring to equation (6.15), it can be seen that there is negative correlation between the operating wavelength and the beat length, and hence the MMI length also has negative correlation with the operating wavelength. Thus, for longer wavelengths a shorter device is needed and vice versa. For the conventional MMI, the spectral response is stronger than that of the tapered device; reaching 10 % efficiency reduction at 1.4 μm as seen in Figure 6.15. From intensity profiles of the conventional MMI in Figure 6.16, it is clear that the optimum length is affected by wavelength change more than the optimum width. As seen, the image formation length is adjusted as the wavelength changes. At 1.2 μm wavelength, the output ports become multimoded; each is supporting two modes that are interacting with the radiation at multimode/output ports interface. This behaviour is weaker at

1.4 µm as the outputs are single mode waveguides and the radiation is not as strong as in case of 1.2 µm. Hence, the conventional MMI needs to re-optimisation if the wavelength is changed.

On the other hand, the tapered device shows good wavelength tolerance so that the efficiency reduction does not exceed 3.8 %. Moreover, it is noticeable that the width has a much better tolerance as the image formation is parallel to the output ports as the wavelength increases. Moreover, the tapers improve the spectral response as seen in Figure 6.17 where the ripples are less pronounced compared to Figure 6.16. However, taken together with unintentional variations from the design during fabrication, these ripples at the output ports at wavelengths of 1.2 µm and 1.4 µm might cause deviation from expected performance and should be carefully monitored in fabricated devices.
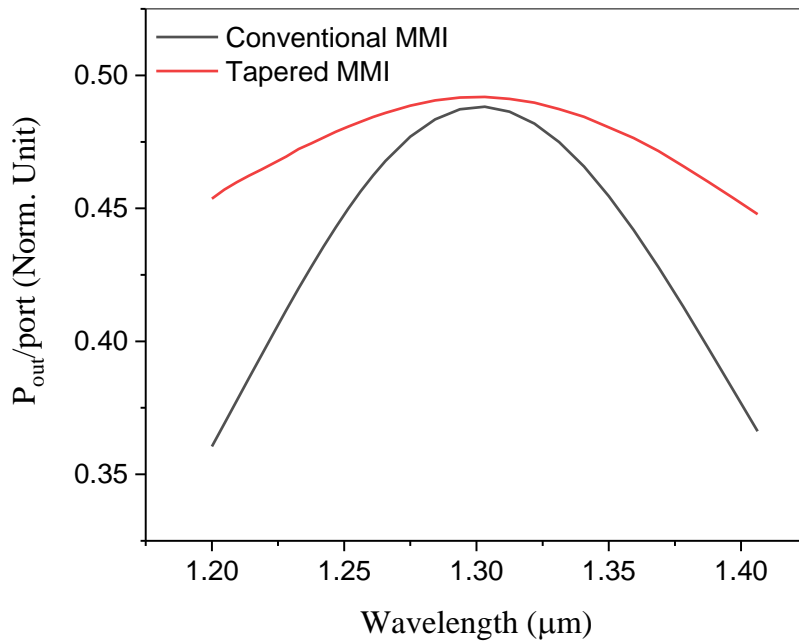
Figure 6.15: Bandwidth of GAAs/AlGaAs conventional and tapered 1×2 MMI at multimode waveguide width = 6 µm and the optimum length. Results are obtained at $\lambda = 1.3$ µ*m* by Fimmprop (eigenmode expansion).
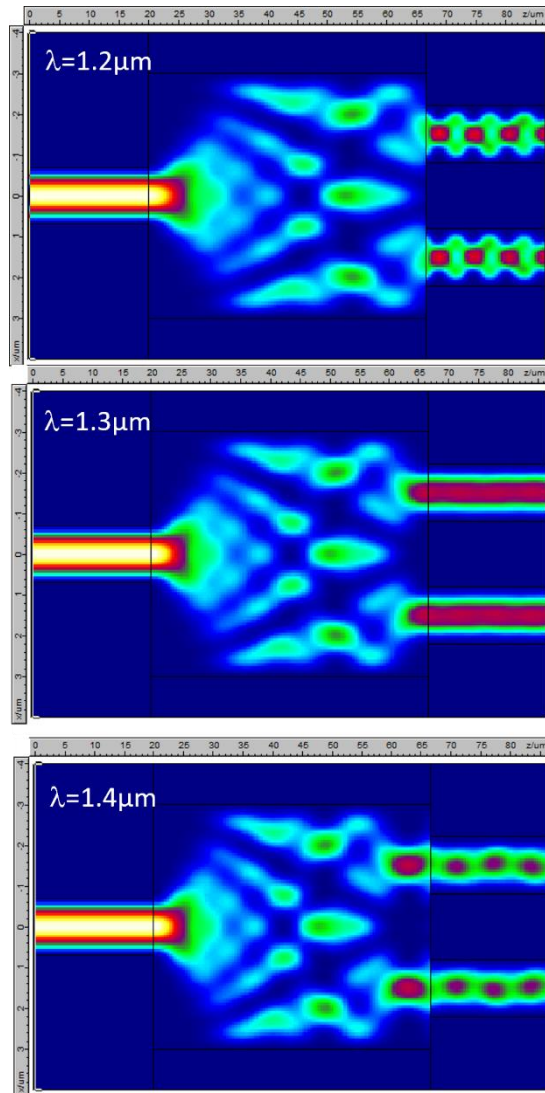
Figure 6.16: Intensity profile of GaAs/AlGaAs conventional 1×2 MMI for operating wavelength of 1.2 μm, 1.3 μm and 1.4 μm. At the output, ripples are formed at wavelengths of 1.2 μm and 1.4 μm. Simulations are done at $\lambda = 1.3$ μm by Fimmprop (eigenmode expansion).
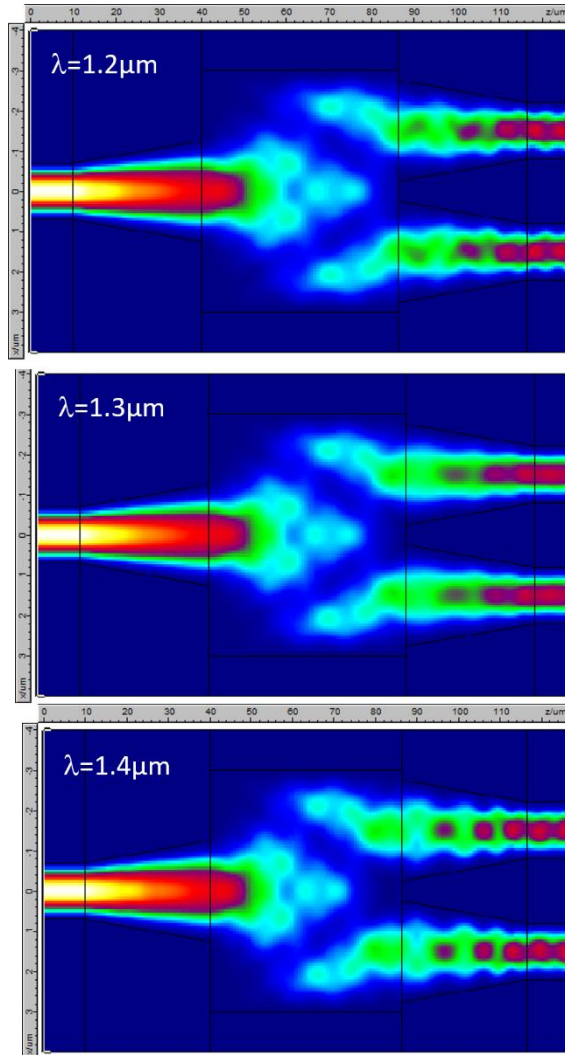
Figure 6.17: Intensity profile of GaAs/AlGaAs tapered 1×2 MMI for operating wavelength of 1.2 μm, 1.3 μm and 1.4 μm. The ripples are weaker than those obtained in the conventional MMI. Simulations are done at $\lambda = 1.3$ μm by Fimmprop (eigenmode expansion).

6.6 Conclusion

In this chapter, a deep etched compact high tolerance symmetrical 1×2 MMI was designed in two configurations: conventional and tapered. Comparing different aspects of both configurations, the tapered device showed higher efficiency (0.49 per port) and geometrical tolerance with relatively flat spectral response over wavelengths from 1.2 μm to 1.4 μm. This tapered 1×2 MMI splitter is promising for OCT that is required to operate over the spectral range between 1.2 μm and 1.4 μm for high resolution. It is also, capable (due to its high efficiency) for cascading 1×2 splitters to distribute signal over a circuit components.

Chapter 7 :

Design and Optimisation of Y-branch Splitters

In this chapter, I report my study of another method of splitting based on optical field splitting. A shallow etched single mode symmetric Y-branch power splitter at ~1.3 μm wavelength for structures made from the GaAs/AlGaAs system is proposed for this functionality. I begin by investigating the splitting functionality of a conventional linear Y-branch to analyse the output and first higher modes. A general optimisation rule is pursued to optimise Y-branches based on both length and curvature of the gap between the output ports. Two small footprint configurations will be compared under variations that are typically encountered due to fabrication with respect to wavelength response and insertion loss. Finally, some modifications, based on results of the two previous chapters, are added to enhance the efficiency of the splitter.

7.1   Background

A Y-branch is a device composed of a wide waveguide that splits into two single mode waveguides. So, an optical signal is divided into two branches. Figure 7.1 shows a schema of the top view of a linear Y-branch consisting of a multimode input of width, $2w$, and two identical single mode output waveguides of width, w, separated by a gap increasing from an input value, G_0, to an output value, G_L along the branch length, L. The gap configuration can be linear or exponential based on the design rule that will be explained later. In this chapter we have considered $G_0 = 0$ as a special case, called the zero-input gap Y-splitter.
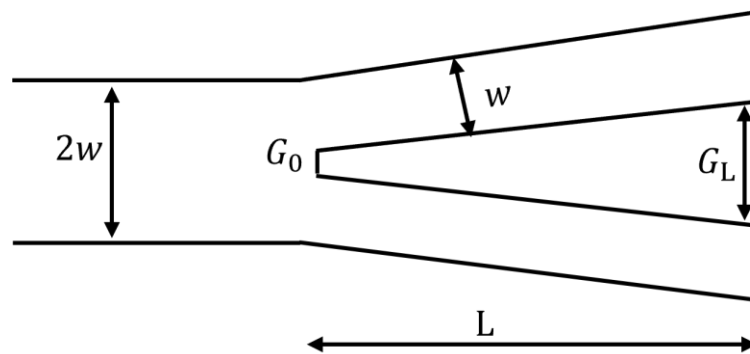
Figure 7.1: Y-branch plan. w is output ports width, G_0 and G_L are input and output gaps, L is branch length.

As has been reported in the literature, the final operation (symmetric splitting and efficiency) of a Y-splitter is influenced by factors like waveguide structure (index contrast), branching angle and length. Previous studies have emphasized the relation between the branching angle and the efficiency of a Y-branch splitter and its wavelength dependence. The relation between TE mode transmission through a linear gap Y-branch and branching angle has been found by studying the radiation losses related to an abrupt junction and separation guide for a single mode waveguide. A positive correlation between radiation loss and branch angle has been found [102]. Using simple ray optics at dielectric interfaces, the interaction between an input optical field and the Y-branch structure and geometry has been explained and compared to beam propagation method simulations. The evolution of the input ray at the junction has been clarified as well as the interaction between the rays in the two branches and the radiation loss related to this interaction [103]. A wavelength independent multi-sectional bend Y-branch with higher efficiency and shorter branching length than conventional bend configuration (circular, cosine and sine bends) was proposed [104]. The effective branching angle in [104] has been calculated based on a simplified coherent coupling effect by optimizing the angles of bend waveguide segments [105]. Regarding the waveguide before the branching, it has been designed with different configurations for efficiency enhancement and compactness purposes. Tapered or multimode sections have been used [106]–[111]. For large scale optical communication splitting, cascading identical splitters helps to obtain an optimised $1 \times N$ splitter by studying a basic 1×2 splitter [112]–[114]. Additionally, 3D polymer-based 1×4 Y-splitter for wavelength splitting at $1.55\,\mu m$ has been reported [115]. Besides the important role of the Y-junction splitters in broadband communication, Y-branches have application in biosensing [116].

7.2   Methodology

Two configurations of Y-branch splitter where the gap increases in a linear or exponential manner were optimised for shallow etched GaAs/AlGaAs single mode waveguides to design efficient compact splitters. The minimum output gap size, G_L, was set by determining the minimum distance between two identical waveguides at which coupling between the waveguides doesn't occur. A conventional 1×2 single

mode Y-branch with input of width twice that of the output ports was set to a length with maximum efficiency to study the output and the first excited modes as they propagate from an input multimode waveguide through the splitting until the end of the output branches. The Y-branches were optimised using the general rule that finds the best curvature for various branch lengths for the smallest gap size between the branches ends. The limitation related to fabrication of a zero size input gap was studied. The devices were analysed for input gap size of zero and 0.3 μm. The simulation is carried out using eigenmode expansion (EME) method [117]. The software parameter values such as mesh size, maximum number of calculation modes and taper paraments were set by considering similar convergence tests to those used in previous chapters.

7.3 Minimum Output Gap (G_L) Size

The final separation required for the two output ports of the splitter may depend on the application due to the physical space required for subsequent components but here we will examine the minimum required separation or output gap, G_L, size where the ports can be considered independent. The interaction between two waveguides causes a splitting of the eigenmodes. The coupled system has so-called supermodes, which are a linear superposition of the original waveguide modes, with a splitting in the eigenvalues proportional to the overlap of the waveguide modes. Therefore, the difference in the eigenvalues, n_{eff}, of the two supermodes is a simple measure of the interaction of the two waveguides. Therefore, the gap between the output waveguides was scanned to find the smallest output gap at which the output modes have zero splitting. In practice, this is found when the mode splitting is trivial. Figure 7.2 shows the effective indices of the output modes of the two branches (A) and the progression of difference between the output modes effective indices as function of output gap size (B). It is seen that the waveguides become independent at gap size of approximately 2 μm. So, this size is set as the smallest gap size at the branching end, *L*. The mode profile for gap size of 0, 1 and 2 μm is presented in Figure 7.2-C,D and E. It is clear that as the gap is increasing, the two branches become more independent of each other and recover their resemblance to two isolated waveguide modes.
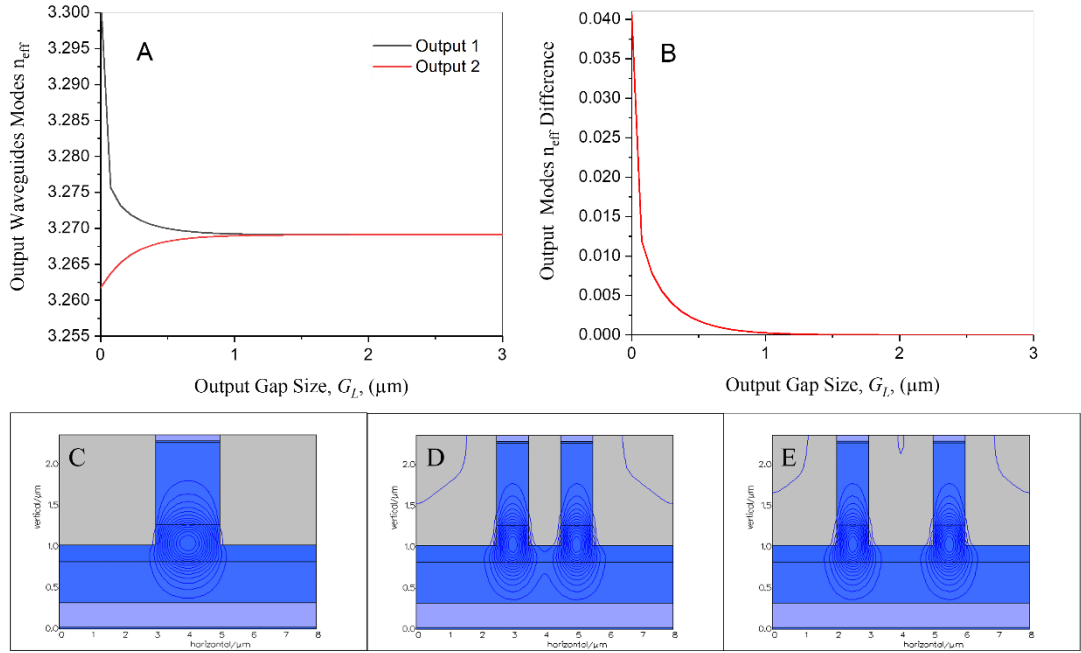
Figure 7.2: (A) Effective indices of the output modes as function of output gap, G_L, size. **(B)** Difference between the effective indices of the output modes as function of output gap, G_L, size. Output mode profiles at output gap size of **(C)** 0, **(D)** 1 μm and **(E)** 2 μm. Simulations are done at $\lambda = 1.3$ μm by Fimmwave FDM solver for mode calculations and Fimmprop (eigenmode expansion) for mode splitting evolution.

7.4 Zero Input Gap ($G_0 = 0$) Y-Branch

In this section the behaviour with zero input gap, G_0, which is defined in Figure 7.1 is investigated to understand the influence of both the gap shape between the output branches and the length on the output confined mode and radiation modes and hence on the efficiency and stability of the splitter under some variations in dimension such as might be seen due to imperfect fabrication and for varying input wavelength.

7.4.1 Length Impact on Output and Radiation Modes Evolution in a Linear Splitter

To study the way modes propagate through the conventional symmetric linear Y-branch (Figure 7.1), the output power per port of the output mode and the radiation mode is recorded as the branch length is varied from 0 to 100 μm as seen in Figure 7.3. The fluctuating behaviour of the output power is due to interference of the output

mode with the radiation mode originating at the start of the branch as the first higher mode radiates upon branching [102]. As the branch becomes longer, the interaction between the output and radiation modes becomes weaker because the radiation power decreases with branch length. Figure 7.1 displays geometrical parameters of linear Y-branch that are used to study the output and first higher modes.

Table 7.1: Linear Y-branch parameters.

Parameter	Value
Input type	Multimode waveguide (constant width)
Output type	Single mode waveguide (constant width)
G_0 (μm)	0
G_L (μm)	2
Etching Depth (μm)	~0.5 H
Wavelength (μm)	1.3
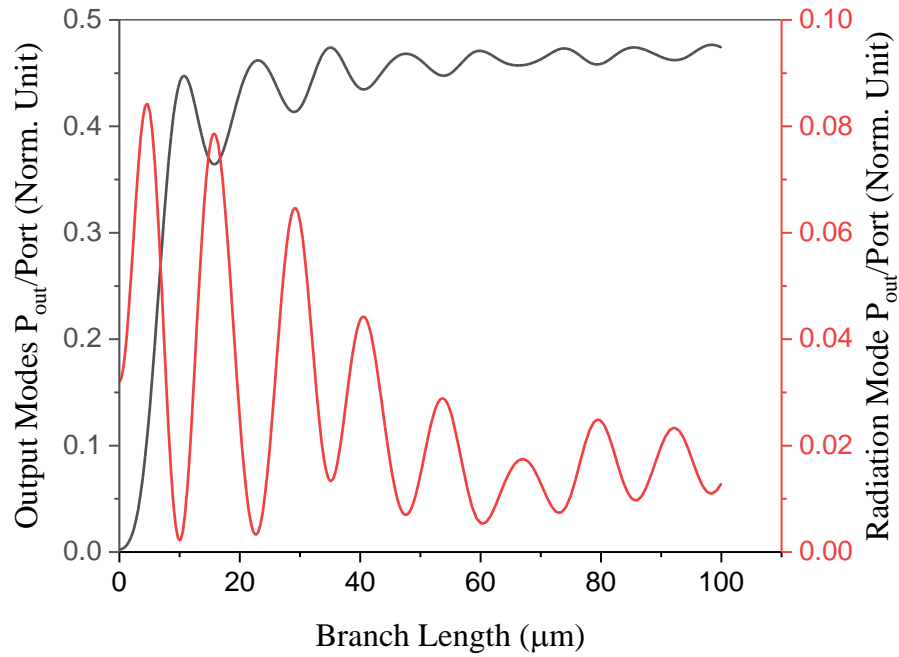
Figure 7.3: P_{out} per port and radiation power per port as function of branch length for GaAs/AlGaAs linear Y-branch of $G_0 = 0$. Simulations are done at $\lambda = 1.3 \, \mu m$ by Fimmprop (eigenmode expansion).

The intensity profiles of the fundamental and first higher modes were tracked along the branch from the start of the splitting until the end of the branch at length of 100 μm. While the fundamental mode stays bound in the branches, the first excited mode transforms into radiation upon the splitting and maintains the same behaviour along the branch as presented in Figure 7.4. At the input waveguide, just before the branch ($G_0 = 0$ μm), the first excited mode is bound in the input multimode waveguide of width twice that of the output waveguides. As the gap advances, the higher mode converts into radiation as its power splits through the gap. Like the fundamental mode, the higher mode starts to undergo a complete split into two parts at gap size between 1.2 and 1.4 μm.
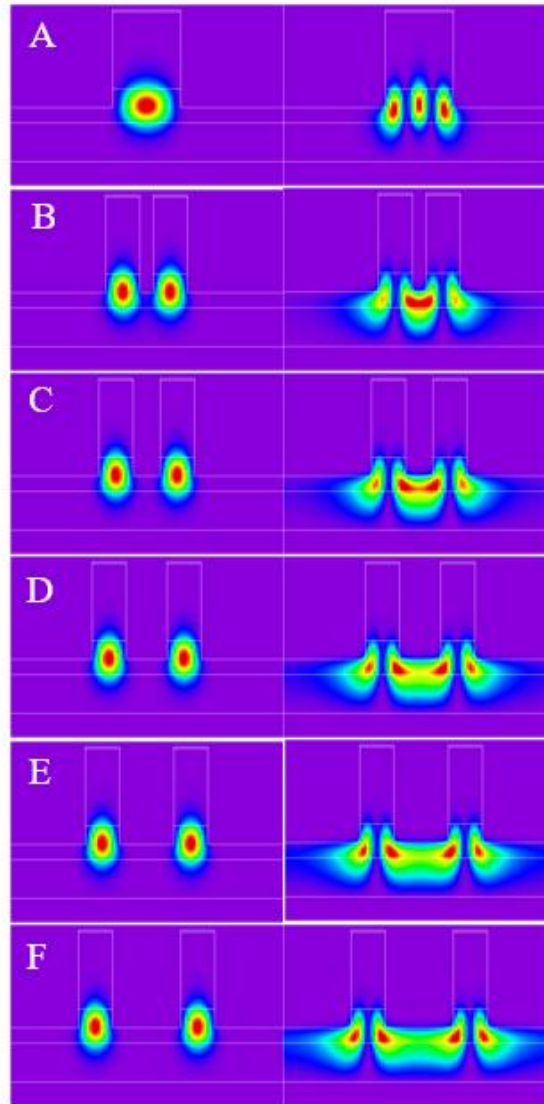
Figure 7.4: Fimmwave FDM solver calculations of intensity profiles of the fundamental (right) and first excited (left) modes along GaAs/AlGaAs taper of length 100 μm at gap size of (A) 0, (B) 0.4 μm, (C) 0.8 μm, (D) 1.2, (E) 1.6 μm and (F) 2μm at $\lambda = 1.3$ μm.

The reason for the increase in P_{out} per port (Figure 7.3) at a length of 100 μm, even though the radiation mode power is small at this length, is the constructive interference between the output mode and the radiation mode as seen in Figure 7.5. So, the choice of optimum length is sensitive to the interaction between the output mode and the radiation mode.
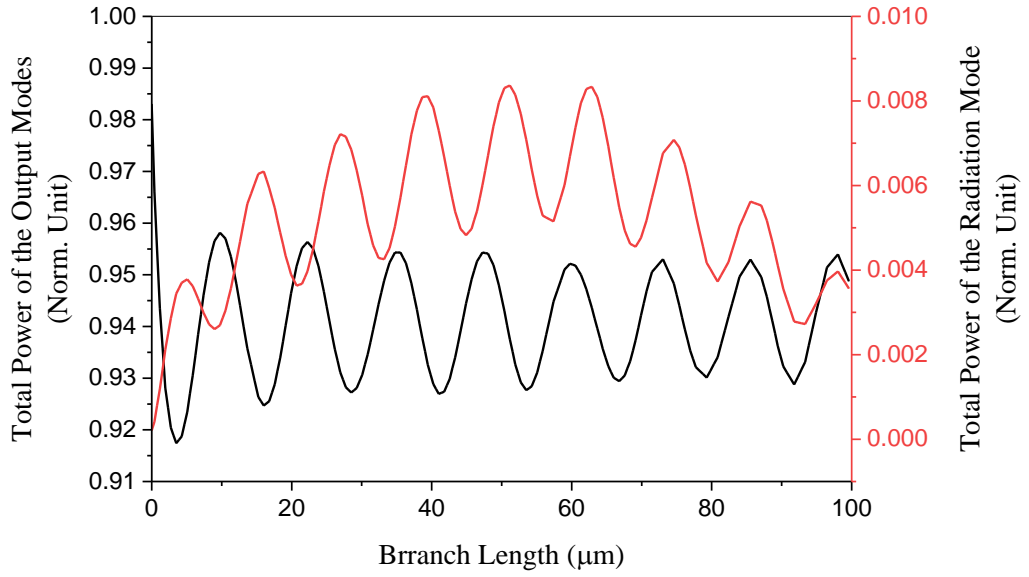
Figure 7.5: Total power of output and radiation modes along GaAs/AlGaAs linear Y-branch of 100 μm long and $G_0 = 0$ at $\lambda = 1.3$ μm as found by Fimmprop (eigenmode expansion).

7.4.2   Geometrical Optimisation at $G_0 = 0$

It is known that extending the length of propagation in devices of varying dimension like tapers and Y-branches will result in high efficiency output. In this section, I will present a generic design rule that optimises shape and length simultaneously to achieve high efficiencies at considerably shorter length. This rule, is similar to that applied in Chapter 5, and is stated as equation (7.1) where $G(z)$ is the gap size as a function of position, z, along the gap between the branches, G_0 is the gap size at position $z = 0$, G_L is the gap size at the end of splitter, L is the length of the branching sector and the curvature constant, b, is optimisation factor (controls the gap geometry along the branching sector) that is scanned for series of chosen L values at known G_0 and G_L.

$$G(z) = (G_L - G_0) * \left(\frac{z}{L} - 1 \right)^b + G_L \qquad (7.1)$$

For each length L from 0 to 50 μm (steps of 0.5 μm), the exponent b is changed over range from 0.2 to 2 in steps of 0.05. The results presented by the colour map in Figure 7.6 are corresponding to $G_0 = 0$μm and $G_L = 2$μm. The alternating patterns as function of length also appear here for all b values in a similar way to that noticed for

the linear branch in Figure 7.3, as result of the interference between the output mode and the radiation mode created at the junction. As the branching section gets longer, this interaction becomes weaker and hence the output power per port turns out to be higher. The most interesting thing in these results is that an efficiency up to 98.1% is achievable for lengths that do not exceed 50 μm with positive correlation between the branch length and both the length tolerance and curvature shape. For $b = 1$, the gap configuration is linear. It is noticeable that for short length (~ 10 μm), the linear Y-branch has higher efficiency compared to other configurations at the same length. However, as the branch becomes longer (~20 μm), other configurations show higher efficiency and better length tolerance than that of the linear one. Considering the length tolerance, a branch length of 23 μm and $b = 0.76$ have efficiency up to P_{out} per port =0.47 nom. Unit is considered optimum. This Y-branch is chosen as high tolerance efficient splitter and will be considered in the following section for further investigations.
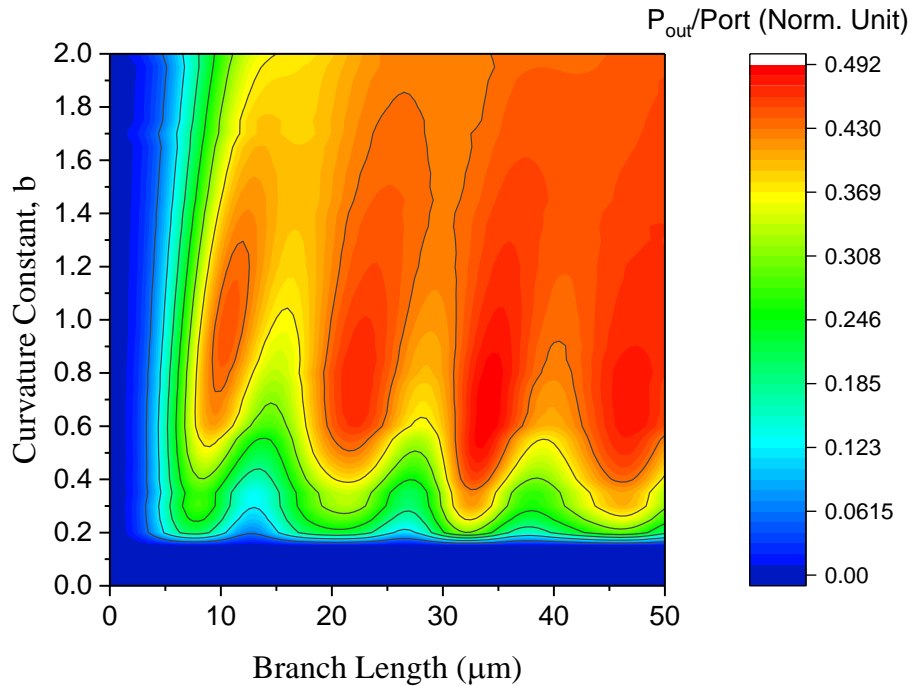
Figure 7.6: GaAs/AlGaAs Y-branch geometrical optimisation at $G_0 = 0$ and $\lambda = 1.3$ μm as simulated by Fimmprop (eigenmode expansion). Branch length extends from 0 to 50 μm and curvature is change over range of $b = 0$ to 2.

7.4.3   Tolerances

Based on the results obtained in the previous section an optimised device of length $L = 23$ µm and $b = 0.76$ with efficiency of P_{out} per port =0.47 nom. unit and length tolerance of ± 1 µm with power reduction of ~ 1.2 % has been chosen. The effect of etching depth and waveguide width variations will be considered in the following section for two configurations: linear and curved device ($b = 0.76$) with the same length. The variation range related to photolithography (~ ± 0.1 µm for I-line) is covered and etching depth variation up to ± 0.1 µm. The fabrication variations are assumed to be the same and changes all features (widths, gaps, etching depths) by the same magnitude.

7.4.3.1   Waveguide Width

The relation between the splitter efficiency and waveguide width changes of ± 0.1 µm is presented in Figure 7.7. The linear Y-branch has a higher stability whereas the efficiency of the exponential one increases as the width increases by 0.1 µm. Increasing the width results in higher confinement and consequently higher output power and vice versa. As for the width variation response, the exponential gap splitter is better in the case of increasing the width.
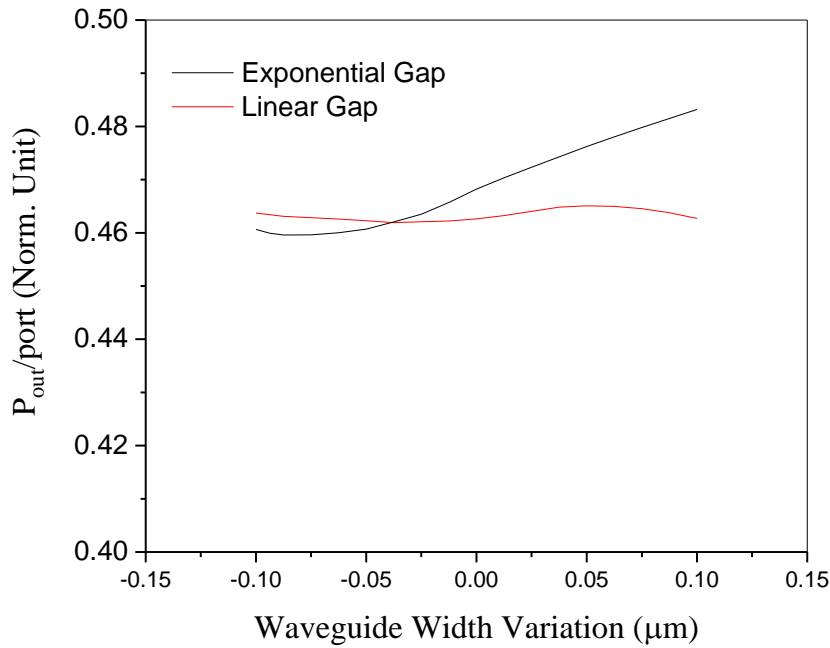
Figure 7.7: Waveguide width variation of both input multimode waveguide and branch single mode waveguides of GaAs/AlGaAs Y-branch of $L = 23$ μm, $G_0 = 0$ and $b = 0.76$ compared to a linear one of the same length and structure. Results are found at $\lambda = 1.3$ μm by Fimmprop (eigenmode expansion).

7.4.3.2   Etching Depth

The two configurations of $b = 1$ and $b = 0.76$ with parameters stated in Table 7.1 were investigated under etching depth variations of ± 0.1 μm. The positive values indicate the etching depth become deeper while the negative values mean the waveguide gets shallower. Both configurations, linear and exponential, as seen in Figure 7.8 have similar response to the etching depth alteration but the linear case has a higher output as it experiences changes in the etching depths. So, the exponential configuration is not preferred unless the etching level variation is between - 0.05 and +0.02 µm.
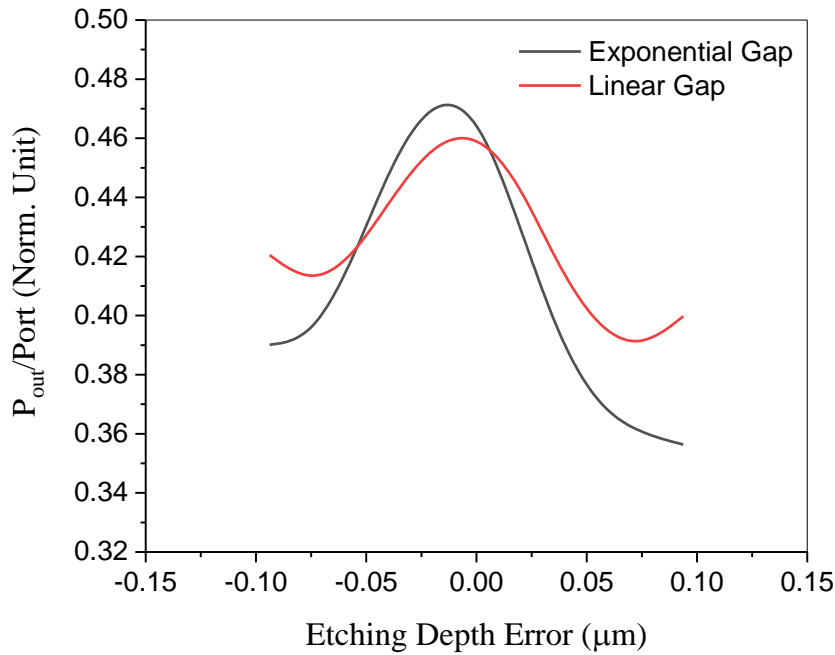
Figure 7.8: Etching depth variation effect on output power per port for both GaAs/AlGaA exponential ($b = 0.76$) and linear Y-branches of $L = 23\ \mu m$ and $G_0 = 0$. Results are found at $\lambda = 1.3\ \mu m$ by Fimmprop (eigenmode expansion).

7.4.4 Wavelength Response

The response of the splitter to the wavelength was studied from 1.2 μm to 1.4 μm as presented in Figure 7.9. Generally, the wavelength change has negative impact on the efficiency between 1.3% at 1.2 μm and 0.6% at 1.4 μm. The exponential Y-splitter response stays flat between 1.26 μm and 1.32 μm with a dramatic increase and fractional decrease at shorter wavelengths than 1.26 μm and greater than 1.32 μm. On the other hand, the linear Y-branch efficiency decreases linearly as the wavelength increases. The overall spectral response is good for both configurations over the range between 1.2 μm and 1.4 μm. The reason for the small decrease at longer wavelength is that the bigger mode size that needs a wider waveguide to ensure high confinement.
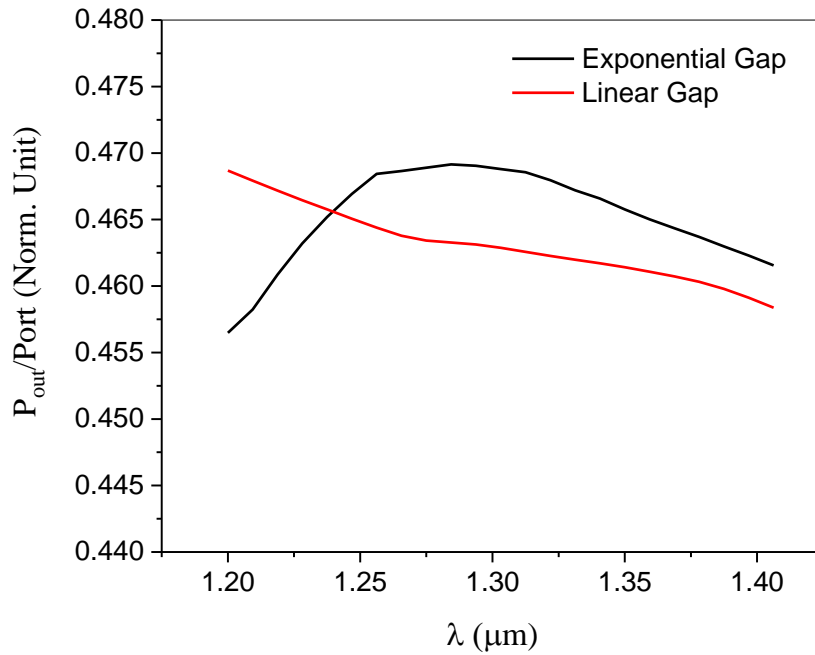
Figure 7.9: Wavelength response of GaAs/AlGaA exponential ($b = 0.76$) and linear Y-branches of $L = 23\ \mu m$ and $G_0 = 0$. Results are found by Fimmprop (eigenmode expansion).

7.5   Non-Zero Input Gap ($G_0 = 0.3\ \mu m$) Y-Branch

In this part of my study, I will track the effect of a non-zero gap, at the beginning of the branch, on the output and radiation modes and check if this gap affects the optimisation and efficiency. A gap close to zero is difficult to fabricate and the 0.3 µm gap is believed to be more realistic. Both further fabrication tolerances and performance will be explored over a range of variations.

7.5.5   Length Impact on Output and Radiation Modes Evolution in a Linear Splitter

Similar steps to those done before were followed to study the output and first higher modes as they propagate from input multimode waveguide undergoing splitting into two parts over a sudden split of 0.3 µm at the beginning of the branch. I assume the gap size increases with the same value all over the branch length but the other parameters are kept the same (Table 7.2Table 7.2).

Table 7.2: Linear Y-branch parameters of $G_0 = 0.3$ μm.

Parameter	Value
Input type	Multimode waveguide (constant width)
Output type	Single mode waveguide (constant width)
G_0(μm)	0.3
G_L (μm)	2.3
Etching Depth (μm)	~0.5 H
Wavelength (μm)	1.3

In this device, the output and first excited modes output power per port as a function of branch length (Figure 7. 10) behave roughly in similar manner to the device of $G_0 = 0$ μm with output power reduction of ~12.4% for the output mode and ~0.7% for first higher mode compared to their output power in case of $G_0 = 0$ μm. As the only change made on the design is the size of gap between the two ports, the reduction in mode power could be caused by experiencing an abrupt change where the splitting starts with a gap of a relatively big size.
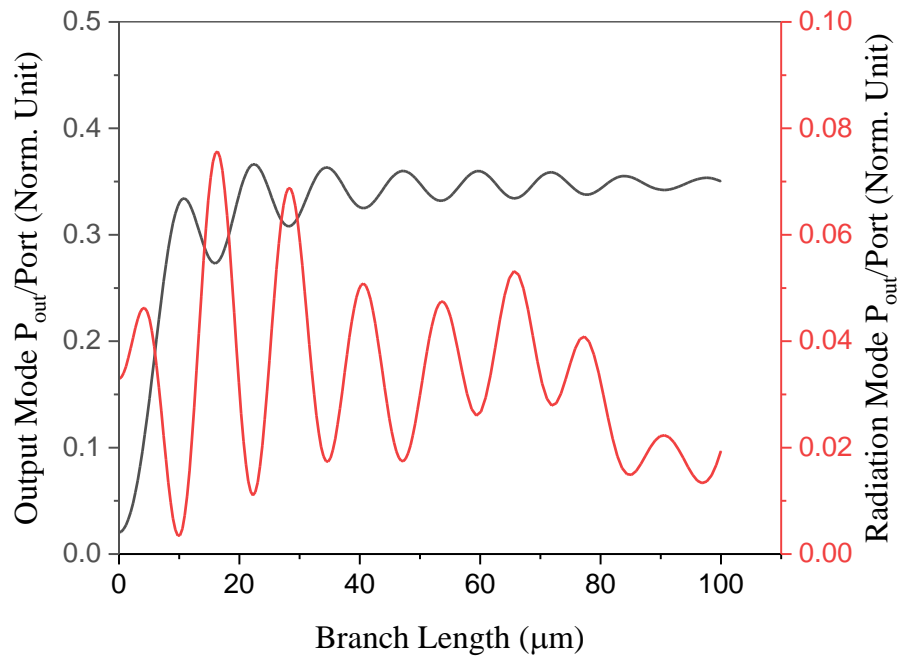
Figure 7. 10: P_out per port and radiation power per port as function of branch length for GaAs/AlGaAs linear Y-branch of $G_0 = 0.3$ μm. Simulations are done at $\lambda = 1.3$ μm by Fimmprop (eigenmode expansion).

Figure 7.11 provides information about the total power of output and radiation modes along a linear Y-branch of 100 µm long and $G_0 = 0.3$ µm. The main finding of this graph is that the two modes are out of phase along the branch and the amount of power carried by the radiation mode in comparison with the same mode in $G_0 = 0$ µm Y-branch is larger. This means having the gap at the starting point of splitting enhances the radiation which results in a drop in the power delivered by the output mode at the end of the splitter.
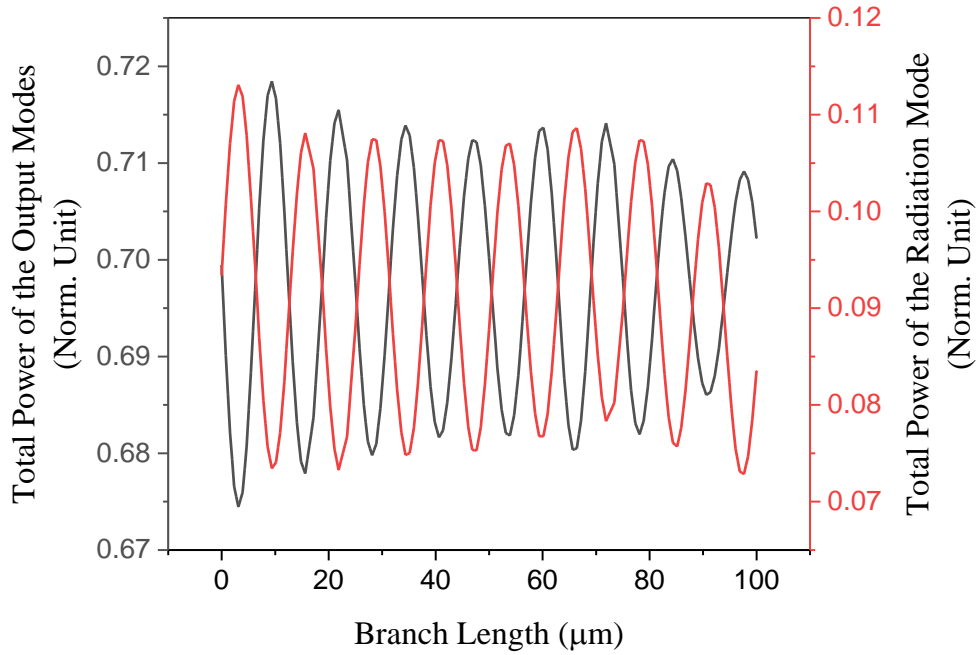
Figure 7.11: Total power of output and radiation modes along GaAs/AlGaAs linear Y-branch of 100 μm long and $G_0 = 0.3$ μm at $\lambda = 1.3$ μm as found by Fimmprop (eigenmode expansion).

7.5.6 Geometrical Optimisation at $G_0 = 0.3$ μm

One of the challenging fabrication limitations is the realisation of acute angles due to the shape and size of the lithography beam or depth of focus of projected image. The minimum size feature limit of lithography defines the achievable minimum gap size which is markedly dependent on the lithography system and the process steps [118]. For example, using deep UV lithography a gap error of less than ± 50 nm was reported for silicon photonics [119] and gap of 100 nm was achievable in InP arrayed waveguide grating [118]. For photolithography using I-line (356 nm) a minimum size feature of 250 nm to 300 nm is achievable. However, a minimum gap size $G_0 = 0.3$ μm is considered here to study its influence on length and curvature optimisation of both length and curvature as well as efficiency to represent the worst case for the type of lithography used in the Institute for Compound Semiconductors. Figure 7.12 presents the length and curvature optimisation of the Y-branch of $G_0 = 0.3$ μm. I assume the gap size is changed by the same amount from $Z = 0$ to $Z = L$, $G_\text{L} =$

$2.3\ \mu m$. The most interesting point of this figure is that the highest achievable efficiency is 0.39 norm. unit per port for maximum length of 50 μm which means the efficiency is significantly G_0 dependant. Although the same type of behaviour is observed as for the zero input gap, the optimum values are shifted toward shorter lengths ($\sim 2\ \mu m$) and smaller b values. For instance, within the same range chosen for $G_0 = 0$ μm, the optimum length was 23 μm and $b = 0.76$ whereas for $G_0 = 0.3$ μm, the optimum length is 21 and $b = 0.6$. For length changes of $\pm 1\ \mu m$ the efficiency reduction is up to 1.1%.
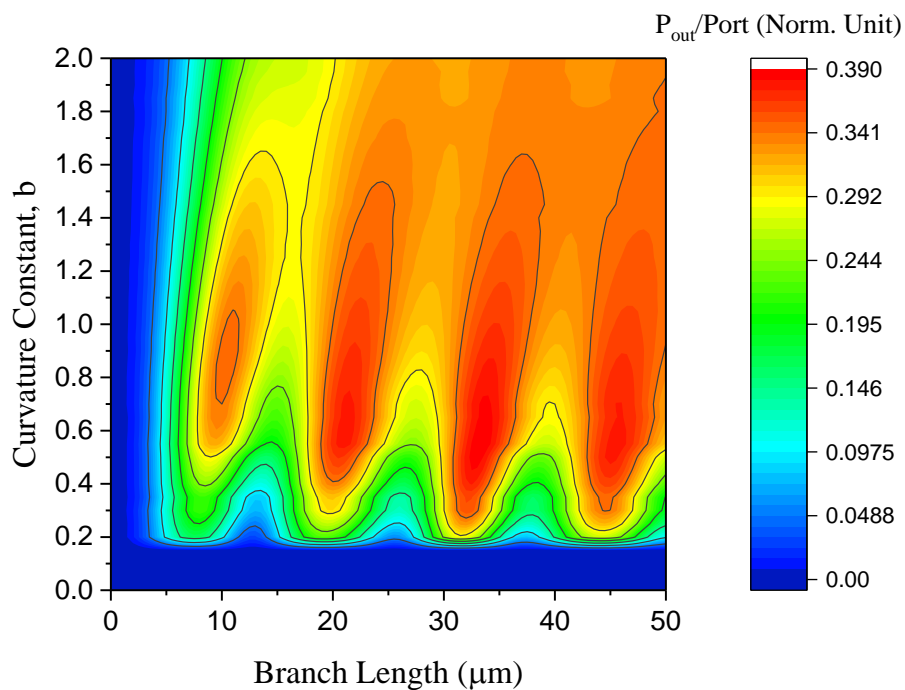
Figure 7.12: GaAs/AlGaAs Y-branch geometrical optimisation at $G_0 = 0.3\ \mu m$ and $\lambda = 1.3\ \mu m$ as simulated by Fimmprop (eigenmode expansion). Branch length extends from 0 to 50 μm and curvature is change over range of $b = 0\ to\ 2$.

7.5.7   Tolerances

7.5.7.1   Waveguide Width

The influence of a width variation range of ± 0.1 μm is illustrated in Figure 7.13. The general outcome of this calculation is similar for both configurations with higher efficiency for the exponential Y-splitter. As the waveguides width increases, the output power increases until it reaches a peak at $+0.07$ μm where the confinement is highest. Further width increments result in the confinement of higher order modes and consequently, lower output is obtained. So, under this variation with the presence of the gap at the start of the branching the exponential device is better due to its higher efficiency.
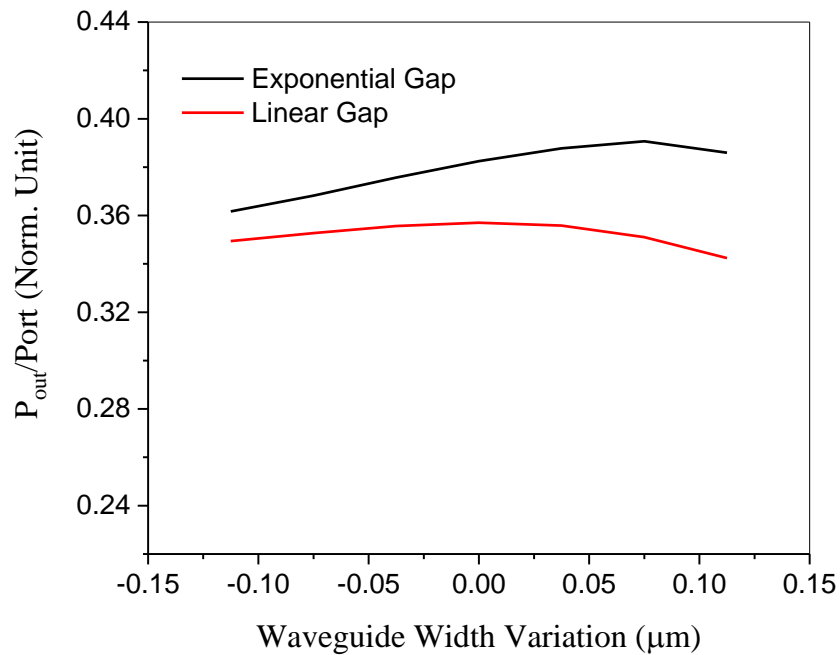
Figure 7.13: Impact of waveguide width change of both input and branch sectors on output power per port of GaAs/AlGaAs Y-branch of $L = 23$ μm, $G_0 = 0.3$ μm and $b = 0.76$ compared to a linear one of the same length and structure. Results are found at $\lambda = 1.3$ μm by Fimmprop (eigenmode expansion).

7.5.7.2   Etching Depth

An overview of the efficiency response to a variation of etching depth is compared for two Y-branch configurations in Figure 7.14. Similar to the case of $G_0 = 0\ \mu m$, the linear Y-branch has higher output power at shallow etching whereas the exponential one only has higher efficiency between 0.02 μm to 0.02 μm etching level. In general, the power of both shapes is dramatically decreasing as the etching become deeper.
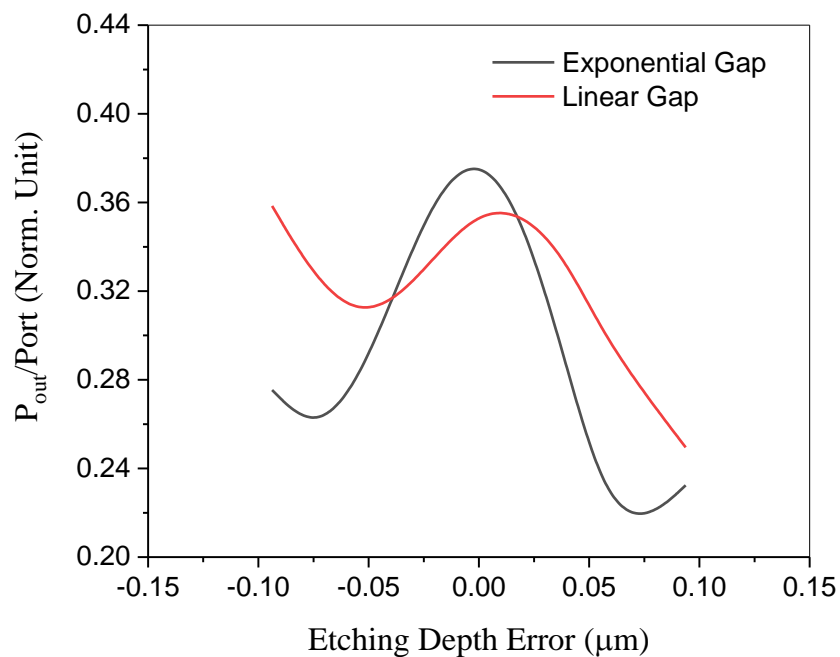
Figure 7.14: Output power per port response to etching depth variation for both GaAs/AlGaA exponential ($b = 0.76$) and linear Y-branches of $L = 23\ \mu m$ and $G_0 = 0.3\ \mu m$. Results are found at $\lambda = 1.3\ \mu m$ by Fimmprop (eigenmode expansion).

7.5.8   Wavelength Response

The effect of a change of wavelength from 1.2 μm to 1.4 μm on the splitters' performance is presented in Figure 7.15. Both configurations are responding somewhat similarly: negative corelation between efficiency and wavelength from 1.2 μm to 1.41 μm followed by steady response. This can be due to the positive

correlation between wavelength and mode size. Thus, the larger the mode size, the less the confinement.
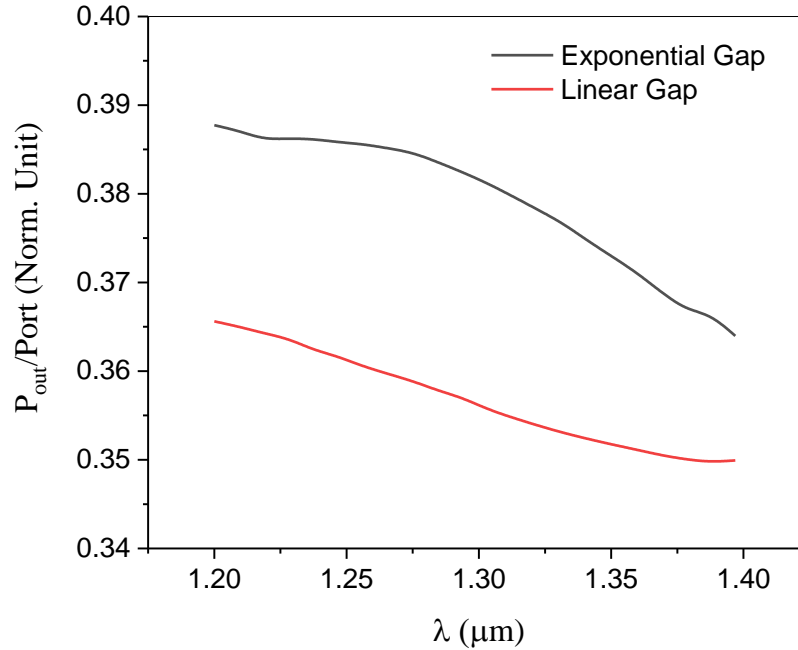
Figure 7.15: Efficiency of GaAs/AlGaA exponential ($b = 0.76$) and linear Y-branches of $L = 23\ \mu m$ and $G_0 = 0.3\ \mu m$ as function of wavelength. Results are found by Fimmprop (eigenmode expansion).

7.6   Modification

A Y-branch can be modified to raise the efficiency or to make the fabrication easier. Here, I will present some designs based on optimised Y-branch of $G_0 = 0.3\ \mu m$. The change will be in the area in between the input and output. I will present the consequence of adding optimised tapered waveguide and tapered multimode sections in the middle of the device.

Table 7.3 provides information about the efficiency of different types of Y-branches. The efficiency of both basic linear and exponential Y-branches is compared with two different types where the input is changed to tapered section or a tapered multimode section is used in between a single mode waveguide input and the branching section. It is found that these modifications have positive impact on the device efficiency. The configuration and intensity profiles are presented in Figure 7.16

. The interference patterns along the branches are result of low confinement due to shallow etching. Looking at the patterns along the MMI based one, it can be seen that this configuration is the best between the three as the intensity profile becomes steady near the end of the branch and deliver the highest efficiency between the three configurations as seen in Table 7.3.

Table 7.3: Efficiency of various GaAs/AlGaAs Y-branch configurations of $G_0 = 0.3 \, \mu m$.

Device Type	Linear P_{out} per port (Norm. Unit)	Exponential P_{out} per port (Norm. Unit)
Basic	0.36	0.38
Tapered input based	0.41	0.4
Tapered MMI based	0.42	0.42
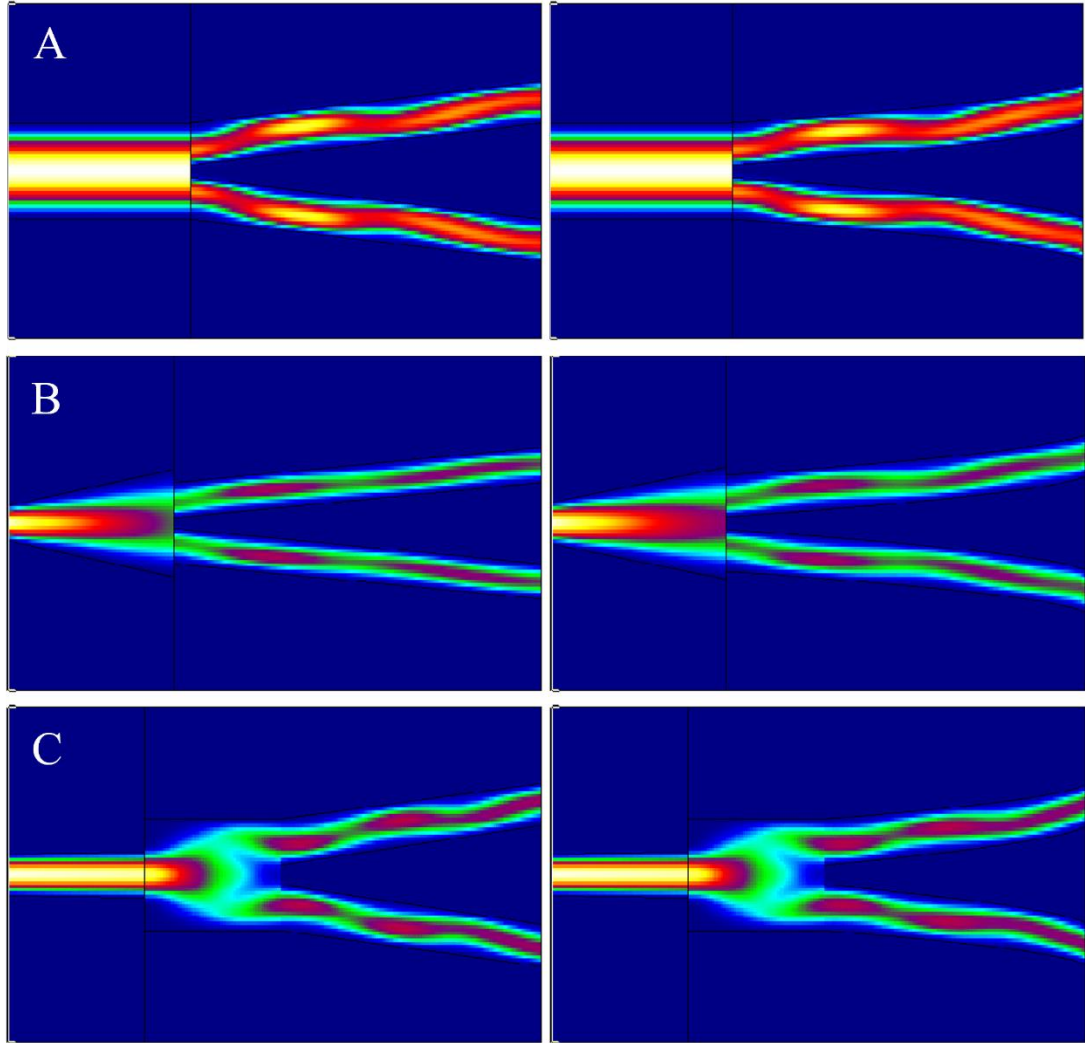
Figure 7.16: Top view of different configurations of linear (right) and exponential (left) Y-branches: (A) Basic (multimode input), (B) Tapered input based and (C) Tapered MMI based. Simulations are performed at $\lambda = 1.3$ μm by Fimmprop (eigenmode expansion).

7.7 Conclusion

In this chapter, I have studied the behaviour of output and first higher mode as they propagate along Y-branches with zero and non-zero input gap. Then, I generated a range of optimisation options of pairs of values (length, curvature) for chosen parameters: G_0 and G_L. This gives wide freedom to choose a preferable design based on different criteria like small footprint, high efficiency and large fabrication tolerances. In addition, the tolerances and performance were examined for different compact configurations. Finally, both non-zero input gap linear and exponential basic designs were modified to enhance the efficiency and give more options of designs. I

found out that both zero and non-zero input gap have similar response to geometrical and operational variations with higher efficiency in case of zero gap device. This work illustrates that it is important to know pre-design whether fabrication limitations will produce a non-zero input gap so that the effects of this can be minimised. To minimise the effect of the input gap, the design rule in equation (7.1) may be used for known length and optimised for (input gap, curvature) to optimise the shape for range of input gaps based on the fabrication limits.

Chapter 8 :

Conclusion

8.1   Summary

The silicon photonic integration research has produced wide range of components at 1.55 µm and some at 1.3 µm and InP based integrated photonics is well established at 1.55 µm wavelength. The aim of this thesis was to explore in a systematic manner, taking account of manufacturability, photonic integrated circuits in GaAs-based materials at a wavelength of 1.3 µm that are compatible with direct growth on a silicon substrate. Towards this aim, the design of several small footprint GaAs-based photonic integration components, which can be used as basic and composite building blocks, are described. The designed components have been optimised using commercially available simulation tools for bandwidth and tolerances typically found when using fabrication tools. The designed components were investigated at a wavelength 1.3 µm and over wavelength range of ±0.1 µm and with tolerances on the size and etching depth typically found following fabrication – a variation of ±0.1 µm for both width and etching depth. Waveguides, tapers, and splitters have been designed and analysed.

As a fundamental step for the optimisation of deep etched waveguides, the structure has been tested numerically for single mode operation in the vertical direction. The results indicate that single mode operation of a (1D) slab waveguide can be obtained with a core height of 0.4 ± 0.2 µm. A waveguide of this height exhibits single mode operation in the lateral direction for ridge waveguide widths between 0.7 and 1.4 µm. These single mode operation dimensions are much smaller than that achieved in [27] and [28] of the same functionality. The influence of a variation in the core height of ±0.1 µm on the single mode width has been analysed. It was found that as the core height increases, the width required to achieve single mode (or "cut-off" higher order modes) becomes smaller. So, with smaller core heights the single mode widths would be easier in fabrication. For a waveguide of constant physical dimension, as the wavelength is changed from 1.2 to 1.4 µm the fundamental mode effective index decreases.

The study of rib waveguides has demonstrated the relation between the core height, width and etching depth required to achieve single mode operation. Heights from 0.4 µm up to a size suitable for fibre coupling have been covered. The main

finding of this part of the thesis is that there is a positive corelation between the core height and the critical etching depth that determines the single mode operation. Generally, for a certain core height as the etching depth gets shallower, the single mode cut-off width gets wider and width tolerance becomes bigger. For a waveguide of a certain core height and etching depth, the fundamental mode effective index decreases as the wavelength increases. The understanding of the two types of waveguides, ridge and rib, provides a good basis for further functional elements in the GaAs-based photonic integration scheme. Similar to [32], the deepest etching depth, critical etching depth, that guarantees single mode operation and offers the highest confinement was obtained for various core heights.

Two design rules, based on adiabaticity and curvature, have been applied to deep etched GaAs-based waveguides to obtain efficient tapers. In comparison with a linear taper, the designed tapers have been found to be more efficient (1/3 linear taper length of the same efficiency) and stable under etching depth variation. Also, the designed tapers have flat spectral response. So, high efficiency small footprint tapers can be obtained to connect different cross-section circuit components to minimise the losses due to mismatch. Adiabaticity based design has predicted similar results to those shown in [82]. Contrary to the previous work, the exponential design introduced in this thesis gives generic optimisation options that allow the designer to choose the suitable size/shape of the taper based on set of conditions such as chip size or fabrication capabilities.

Using the ridge waveguide that is investigated in Chapter 3, two configurations of small footprint 1×2 MMI's have been designed and compared. The simulation results show that the tapered MMI efficiency is higher than 0.45 per port over the spectral range 1.2 µm to 1.4 µm. In addition, the use of tapers on the MMI input and exit ports somewhat relaxes width, length, gap size and input position tolerances. Both tapered and untapered configurations have similar behaviour with regard to input width and etching depth changes. However, the tapered MMI is preferable for its higher efficiency and fabrication tolerances. In comparison with previous work done on GaAs, our design is much smaller than the footprint mentioned in [34] and [39]. Like the results of [36], this design is more sensitive to width variation compared to length variation.

Shallow etched waveguides have been implemented in Chapter 7 to optimise efficient Y-branch splitters. The smallest gap required for independent output waveguides has been found by calculating the splitting of the supermodes in the output waveguides. The interaction between output and radiation modes has been demonstrated. An approach based on an exponential taper was applied to design an efficient Y-branch. The most efficient with zero and non-zero input gap have been compared to the corresponding linear ones. The input gap, which is likely due to fabrication imperfections, has negative impact on the efficiency where the highest efficiency is 0.39 per port with input gap of 0.3 µm while efficiency up to 0.49 per port can be obtained with zero input gap. The designed (zero and non-zero input gap) Y-branch has higher output as the waveguide width is increased. Both the linear and designed (zero and non-zero input gap) are sensitive to etching depth variation. The zero input gap Y-branch has stable response for spectral changes, with a less than 1.3% reduction in output intensity across the wavelength range from 1.2 to 1.4 µm, but the non-zero output gap design has a higher efficiency at 1.2 µm wavelength. The non-zero input gap Y-branch efficiency has been improved (4-6%) by adding tapering to the input and using multimode section. This illustrates that it is essential to design based on the known fabrication performance as the optimum design is quite different for e.g. non-zero and zero input gap size. The exponential based approach gives a wide range of options to choose much smaller footprint devices in comparison with [41] and [42].

This thesis introduced a range of novel structure-based components that are useful for integration with other device, both passive or active, for mainly light coupling by waveguides and tapers and splitting by 1×2 splitters. Two types of efficient 1×2 splitters have been demonstrated. The general comparison shows that the tapered MMI has better fabrication tolerance but with larger footprint. However, both MMI and Y-branch are of good capability at a specified etching level. More options for the splitting functionality devices could be achieved with other design approaches like inverse design. This technology would produce some other options of geometries that can be tested and compared with our designs.

8.2   Future Work

This thesis contains a description and understanding of the designs of some GaAs-based photonic integration building blocks. The simulation has given details about size and configuration of these building blocks. In addition, the expected reaction for some variations has been covered. Hence, a clear idea about these components capability for a certain functionality has been obtained. An iterative approach should now be followed where fabricated and characterised components are used to update the tolerances assumed here and a process design kit (PDK) is established for the GaAs based photonic integration platform. After establishing the performance of individual components, they can be simulated with other devices for on-chip integration and then moved to fabrication for further evaluation and feedback to the design process.

Bibliography

[1]   L. Chrostowski and M. Hochberg, *Silicon Photonics Design: From Devices to Systems*, 1st ed. Cambridge: Cambridge University Press., 2015.

[2]   G. T. Reed and A. P. Knights, *Silicon Photonics An Introduction*, 1st ed. Sussex: John Wiley & Sons Ltd, 2004.

[3]   M. Hilbert and P. López, "The world's technological capacity to store, communicate, and compute information," *Science (80-.).*, vol. 332, no. 6025, pp. 60–65, 2011, doi: 10.1126/science.1200970.

[4]   P. J. Winzer, D. T. Neilson, and A. R. Chraplyvy, "Fiber-optic transmission and networking: the previous 20 and the next 20 years [Invited]," *Opt. Express*, vol. 26, no. 18, p. 24190, 2018, doi: 10.1364/oe.26.024190.

[5]   P. J. Winzer and D. T. Neilson, "From Scaling Disparities to Integrated Parallelism: A Decathlon for a Decade," *J. Light. Technol.*, vol. 35, no. 5, pp. 1099–1115, 2017, doi: 10.1109/JLT.2017.2662082.

[6]   Y. Kawaguchi, Y. Tamura, T. Haruna, Y. Yamamoto, and M. Hirano, "Ultra low-loss pure silica core fiber," *SEI Tech. Rev.*, no. 80, pp. 50–55, 2015.

[7]   "What is C band and L band in WDM (Wavelength Division Multiplexing)?," 2020. https://www.thunder-link.com/blog/what-is-c-band-and-l-band-in-wdm-wavelength-division-multiplexing/ (accessed Aug. 31, 2022).

[8]   "The Fiber Optic Association." https://www.thefoa.org/tech/ref/basic/SMbands.html (accessed Mar. 30, 2023).

[9]   S. Yun, G. Tearney, B. Bouma, B. Park, and J. de Boer, "High-speed spectral-domain optical coherence tomography at 1.3 μm wavelength," *Opt. Express*, vol. 11, no. 26, p. 3598, 2003, doi: 10.1364/oe.11.003598.

[10]   R. N. Khurana, Y. Li, M. Tang, M. M. Lai, and D. Huang, "High-speed Optical Coherence Tomography of Corneal Opacities," *Ophthalmology*, vol. 114, no. 7, pp. 1278–1285, 2007, doi: 10.1016/j.ophtha.2006.10.033.

[11]   M. Smit *et al.*, "An introduction to InP-based generic integration technology," *Semicond. Sci. Technol.*, vol. 29, no. 8, 2014, doi: 10.1088/0268-1242/29/8/083001.

[12]   G. es Lifante, *Integrated Photonics: Fundamentals*, 1st ed. John Wiley & Sons Ltd, 2003.

[13]   C. Vieu *et al.*, "Electron beam lithography: Resolution limits and applications," *Appl. Surf. Sci.*, vol. 164, no. 1–4, pp. 111–117, 2000, doi: 10.1016/S0169-4332(00)00352-4.

[14]   C. Wagner and N. Harned, "EUV lithography: Lithography gets extreme," *Nat. Photonics*, vol. 4, no. 1, pp. 24–26, 2010, doi: 10.1038/nphoton.2009.251.

[15]   L. R. Harriott, "Limits of Lithography," *Ext. Defects Ger.*, vol. 89, no. 3, 2009, doi: 10.1007/978-3-540-85614-6.

[16]   O. Karker, R. Bange, E. Bano, and V. Stambouli, "Optimizing interferences of DUV lithography on SOI substrates for the rapid fabrication of sub-wavelength features," *Nanotechnology*, vol. 32, no. 23, 2021, doi: 10.1088/1361-6528/abe3b6.

[17]   T. Manouras and P. Argitis, "High sensitivity resists for EUV lithography: A review of material design strategies and performance results," *Nanomaterials*, vol. 10, no. 8, pp. 1–24, 2020, doi: 10.3390/nano10081593.

[18]   S. Chuang, *Physics of Photonic Devices*, 2nd ed. New Jersey: John Wiley & Sons Ltd, 2009.

[19]   G. A. Vawter, "Defining capabilities of Si and InP photonics," *2010 IEEE Avion. Fiber-Optics Photonics Technol. Conf. AVFOP 2010*, vol. 1, pp. 53–54, 2010, doi: 10.1109/AVFOP.2010.5637674.

[20]   M. V. Maximov, N. N. Ledentsov, V. M. Ustinov, Z. I. Alferov, and D. Bimberg, "GaAs-based 1.3 μm InGaAs quantum dot lasers: A status report," *J. Electron. Mater.*, vol. 29, no. 5, pp. 476–486, 2000, doi: 10.1007/s11664-000-0032-5.

[21] S. Mokkapati and C. Jagadish, "III-V compound SC for optoelectronic devices," *Mater. Today*, vol. 12, no. 4, pp. 22–32, 2009, doi: 10.1016/S1369-7021(09)70110-5.

[22] S. S. Mikhrin *et al.*, "High power temperature-insensitive 1.3 μm InAs/InGaAs/GaAs quantum dot lasers," *Semicond. Sci. Technol.*, vol. 20, no. 5, pp. 340–342, 2005, doi: 10.1088/0268-1242/20/5/002.

[23] N. Y. Gordeev *et al.*, "Low-threshold 1.3 μm ring lasers with InAs/InGaAs/GaAs quantum dot active region," *Laser Physics Letters*, vol. 19, no. 6. 2022. doi: 10.1088/1612-202X/ac6a62.

[24] R. Williams, *Gallium Arsenide Processing Techniques*, 1st ed. Washington: Artech House, 1984.

[25] A. Karunagaran, R. Bute, and A. Ranjan, "Circuits Today: Energy Band Structure of Gallium Arsenide (GaAs)," 2015. http://www.circuitstoday.com/energy-band-structure-of-gallium-arsenide-gaas# (accessed Feb. 20, 2018).

[26] L. M.-F. et Al, "Optimization of InAs/GaAs quantum dot structures and application to 1.3 μm mode-locked laser diodes," *Chinese Phys*, vol. 23, no. 2, 2014.

[27] A. Ferguson, S. Clements, S. Iezekiel, R. Pollard, and C. Snowden, "Design of deep-etched, AlGaAs/GaAs optical waveguides with reduced fabrication tolerance sensitivity," *IEEE High Freq. Postgrad. Student Colloq.*, vol. 2002-Janua, 2002, doi: 10.1109/HFPSC.2002.1088430.

[28] J. M. Heaton *et al.*, "Optimization of Deep-Etched, Single-Mode GaAs/AlGaAs Optical Waveguides Using Controlled Leakage into the Substrate," *J. Light. Technol.*, vol. 17, no. 2, pp. 267–280, 1999, doi: 10.1109/50.744237.

[29] E. D. Finlayson, J. M. Heaton, B. M. A. Rahman, and S. S. A. Obayya, "Polarization conversion in passive deep-etched GaAs/AlGaAs waveguides," *J. Light. Technol.*, vol. 24, no. 3, pp. 1425–1432, 2006, doi: 10.1109/JLT.2005.863240.

[30] C. D. Watson, M. Poirier, J. M. Heaton, M. Lewis, and M. Boudreau, "Acoustooptic resonance in deep-etched GaAs-AlGaAs electrooptic modulators," *J. Light. Technol.*, vol. 22, no. 6, pp. 1598–1603, 2004, doi: 10.1109/JLT.2004.829221.

[31] M. Sieger and B. Mizaikoff, "Optimizing the design of GaAs/AlGaAs thin-film waveguides for integrated mid-infrared sensors," *Photonics Res.*, vol. 4, no. 3, p. 106, 2016, doi: 10.1364/prj.4.000106.

[32] A. D. Ferguson, A. Kuver, J. M. Heaton, Y. Zhou, C. M. Snowden, and S. Iezekiel, "Low-loss, single-mode GaAs/AlGaAs waveguides with large core thickness," *IEE Proc. Optoelectron.*, vol. 153, no. 2, pp. 51–56, 2006, doi: 10.1049/ip-opt:20050024.

[33] Y. T. Byun, K. H. Park, S. H. Kim, S. S. Choi, and T. K. Lim, "Single-mode GaAs/AlGaAs W waveguides with a low propagation loss," *Appl. Opt.*, vol. 35, no. 6, p. 928, 1996, doi: 10.1364/ao.35.000928.

[34] J. P. Koester, M. Radziunas, A. Zeghuzi, H. Wenzel, and A. Knigge, "Simulation and design of a compact GaAs based tunable dual-wavelength diode laser system," *Opt. Quantum Electron.*, vol. 51, no. 10, pp. 1–12, 2019, doi: 10.1007/s11082-019-2050-2.

[35] B. M. A. Rahman, W. Boonthittanont, S. S. A. Obayya, T. Wongcharoen, E. O. Ladele, and K. T. V. Grattan, "Rigorous beam propagation analysis of tapered spot-size converters in deep-etched semiconductor waveguides," *J. Light. Technol.*, vol. 21, no. 12, pp. 3392–3398, 2003, doi: 10.1109/JLT.2003.821753.

[36] S. Cao *et al.*, "Multimode interference couplers for 2x2 high speed GaAs-GaAlAs electro-optic switches," *Opt. Components Mater. III*, vol. 6116, p. 61160O, 2006, doi: 10.1117/12.641502.

[37] D. S. Levy, Y. M. Li, R. Scarmozzino, and R. M. Osgood, "A multimode interference-based variable power splitter in GaAs-AlGaAs," *IEEE Photonics Technol. Lett.*, vol. 9, no. 10, pp. 1373–1375, 1997, doi: 10.1109/68.623267.

[38] J. M. Heaton *et al.*, "Novel 1-to-N way integrated optical beam splitters using

symmetric mode mixing in GaAs / AlGaAs multimode waveguides Novel I-to-N way integrated optical beam splitters mixing in GaAs / AIGaAs multimode waveguides using symmetric mode," vol. 1754, no. 1992, pp. 46–49, 2017.

[39]   R. Yin, J. Teng, and S. Chua, "A 1 × 2 optical switch using one multimode interference region," *Opt. Commun.*, vol. 281, no. 18, pp. 4616–4618, 2008, doi: 10.1016/j.optcom.2008.05.042.

[40]   K. Al-hemyari, G. F. Doughty, C. D. W. Wilkinson, A. H. Kean, and C. R. Stanley, "Optical Loss Measurements on GaAs / GaAlAs Single-Mode Waveguide Y-Junctions and Waveguide Bends," vol. 11, no. 2, pp. 272–276, 1993.

[41]   P. Buchmann, H. Kaufmann, H. Melchior, and G. Guekos, "Broadband Y-branch efectro-optic GaAs waveguide interferometer," vol. 462, pp. 10–13, 1985, doi: 10.1063/1.95613.

[42]   R. K. Price *et al.*, "Y-Branch Surface-Etched Distributed Bragg Reflector Lasers at 850 nm for Optical Heterodyning," vol. 19, no. 20, pp. 1610–1612, 2007.

[43]   S. M *et al.*, "On-Chip Integrated Mid-Infrared GaAs-AlGaAs Mach−Zehnder," *Anal Chem. 2013*, vol. 85, no. 6, 2012, doi: 10.1021/ac302551s.

[44]   K. D. Jöns *et al.*, "Monolithic on-chip integration of semiconductor waveguides, beamsplitters and single-photon sources," *J. Phys. D. Appl. Phys.*, vol. 48, no. 8, 2015, doi: 10.1088/0022-3727/48/8/085101.

[45]   J. Wang *et al.*, "Gallium arsenide (GaAs) quantum photonic waveguide circuits," vol. 327, pp. 49–55, 2014, doi: 10.1016/j.optcom.2014.02.040.

[46]   W. Grande, J. Johnson, and C. Tang, "GaAs/AlGaAs photonic integrated circuits fabricated using chemically assisted ion beam etching," *Appl. Phys. Lett. 57,* vol. 2537, no. 57, 1990.

[47]   P. Jiang and K. C. Balram, "Suspended gallium arsenide platform for building large scale photonic integrated circuits: passive devices," *Opt. Express*, vol. 28,

no. 8, p. 12262, 2020, doi: 10.1364/oe.385618.

[48]   S. L. Hada and B. M. A. Rahman, "Rigorous analysis of numerical methods: a comparative study," *Opt. Quantum Electron.*, vol. 48, no. 6, pp. 1–13, 2016, doi: 10.1007/s11082-016-0579-x.

[49]   Jia-Ming Liu, *Photonic Devices*, 1st ed. Cambridge University Press., 2005.

[50]   C. Pollock and M. Lipson, *Integrated Photonics*, vol. 90. 2004.

[51]   B. M. A. Rahman and A. Agrawal, *Finite Element Modeling Methods for Photonics*. Boston: Artech House, 2013.

[52]   Y. Shi, *Design, Simulation and Characterization of Some Planar Lightwave Circuits*, PhD thesis. Stockholm: KTH School of Information and Communication Technology, 2008.

[53]   L. Feng, H. Liu, G. Wang, and H. Yu, "Design on waveguides coupler for integrated fiber optical gyroscope based on SOI wafer," no. November 2007, 2022, doi: 10.1117/12.779846.

[54]   X. Xu, S. Chen, J. Yu, and X. Tu, "An investigation of the mode characteristics of SOI submicron rib waveguides using the film mode matching method," *J. Opt. A Pure Appl. Opt.*, vol. 11, no. 1, 2009, doi: 10.1088/1464-4258/11/1/015508.

[55]   M. Lohmeyer, "Wave-matching method for mode analysis of dielectric waveguides," *Opt. Quantum Electron.*, vol. 29, no. 9, pp. 907–922, 1997, doi: 10.1023/A:1018581701193.

[56]   S. J. Zhong, D. A. Yuen, and L. N. Moresi, "Numerical Methods for Mantle Convection," *Treatise Geophys.*, vol. 7, pp. 227–252, Jan. 2007, doi: 10.1016/B978-044452748-6.00118-8.

[57]   N. M. Kassim, A. B. U. B. Mohammad, and M. H. Ibrahim, "OPTICAL WAVEGUIDE MODELLING BASED ON SCALAR," vol. 42, no. D, pp. 41–53, 2007.

[58]   "FIMMPROP Manual Version 7.2," *Phot. Des.*, 2021.

[59]   "BATOP GmbH." https://www.batop.de/index.html (accessed Jul. 24, 2022).

[60]   "Foothill   Instruments."   http://www.foothill-instruments.com/AP01.htm
         (accessed Jul. 24, 2022).

[61]   "Fimmwave." Photon Design, 34 Leopold St, Oxford, OX4 1TW, UK. [Online].
         Available: www.photond.com

[62]   "FIMMWAVE Manual Version 7.2," *Phot. Des.*, 2021, [Online]. Available:
         www.photond.com

[63]   J. Dailesasse, N. Hoionyak, J. Sugg, T. Richard, and N. El-Zein, "Hydrolyzation
         oxidation of Al x Ga 1 − x As-AlAs- GaAs quantum well heterostructures and
         superlattices," vol. 2844, no. June 1998, pp. 3–6, 2013.

[64]   K. D. Choquette *et al.*, "Advances in Selective Wet Oxidation of AlGaAs
         Alloys," vol. 3, no. 3, pp. 916–926, 1997.

[65]   S. Majumder and R. Chakraborty, "Semianalytical method to study silicon slot
         waveguides for optical sensing application," *Opt. Eng.*, vol. 52, no. 10, p.
         107102, 2013, doi: 10.1117/1.oe.52.10.107102.

[66]   S. T. Lim, C. E. Png, E. A. Ong, and Y. L. Ang, "Single mode, polarization-
         independent submicron silicon waveguides based on geometrical adjustments,"
         Opt. Express, vol. 15, no. 18, p. 11061, 2007, doi: 10.1364/oe.15.011061.

[67]   M. Masi, R. Orobtchouk, G. Fan, J. M. Fedeli, and L. Pavesi, "Towards a
         realistic modelling of ultra-compact racetrack resonators," *J. Light. Technol.*,
         vol. 28, no. 22, pp. 3233–3242, 2010, doi: 10.1109/JLT.2010.2078797.

[68]   Y. K. Lize, E. C. Magi, V. G. Ta'eed, J. A. Bolger, P. Steinvurzel, and B. J.
         Eggleton, "Microstructured optical fiber photonic wires with subwavelength
         core diameter," *Opt. Express*, vol. 12, no. 14, p. 3209, 2004, doi:
         10.1364/opex.12.003209.

[69]   R. A. Soref, J. Schmidtchen, and K. Petermann, "Large Single-Mode Rib

Waveguides in GeSi-Si and Si-on-SiO2," *IEEE J. Quantum Electron.*, vol. 27, no. 8, pp. 1971–1974, 1991, doi: 10.1109/3.83406.

[70] H. Huang, K. Liu, B. Qi, and V. J. Sorger, "Re-analysis of single-mode conditions for silicon rib waveguides at 1550 nm wavelength," *J. Light. Technol.*, vol. 34, no. 16, pp. 3811–3817, 2016, doi: 10.1109/JLT.2016.2579163.

[71] D. Yuan, Y. Dong, Y. Liu, T. Li, X. Zhang, and Y. Tan, "Polarized single-mode condition for SOI rib waveguide with large cross section," *2015 Int. Conf. Opt. Instruments Technol. Micro/Nano Photonics Fabr.*, vol. 9624, p. 96240A, 2015, doi: 10.1117/12.2185098.

[72] S. Pogossian, L. Vescan, and A. Vonsovici, "The Single-Mode Condition for Semiconductor Rib Waveguides with Large Cross Section," *J. Light. Technol.*, vol. 16, no. 10, pp. 1851–1853, 1998, doi: 10.1109/JLT.2004.832427.

[73] A. G. Rickman, G. T. Reed, and F. Namavar, "Silicon-on-insulator optical rib waveguide loss and mode characteristics," vol. 12, no. October, pp. 0–5, 1994.

[74] J. Lousteau, D. Furniss, A. B. Seddon, T. M. Benson, A. Vukovic, and P. Sewell, "The single-mode condition for silicon-on-insulator optical rib waveguides with large cross section," *J. Light. Technol.*, vol. 22, no. 8, pp. 1923–1929, 2004, doi: 10.1109/JLT.2004.832427.

[75] Y. Li, T. Lan, D. Yang, and Z. Wang, "Results in Physics Re-analysis of single-mode conditions for thin-film lithium niobate rib waveguides," *Results Phys.*, vol. 30, p. 104824, 2021, doi: 10.1016/j.rinp.2021.104824.

[76] H. Jung, "Modal analysis and design of silicon nitride rib waveguides for evanescent-wave bimodal biosensors," *Curr. Opt. Photonics*, vol. 3, no. 5, pp. 382–389, 2019, doi: 10.3807/COPP.2019.3.5.382.

[77] P. G. Suchoski and R. V. Ramaswamy, "Design of single-mode step-tapered waveguide sections," *IEEE J. Quantum Electron.*, vol. 23, no. 2, pp. 205–211, 1987, doi: 10.1109/JQE.1987.1073307.

[78] O. Mitomi, K. Kasaya, and H. Miyazawa, "Design of a Single-Mode Tapered Waveguide for Low-Loss Chip-to-Fiber Coupling," *IEEE J. Quantum Electron.*, vol. 30, no. 8, pp. 1787–1793, 1994, doi: 10.1109/3.301643.

[79] V. Muniswamy and N. Krishnaswamy, "Modelling, design and optimization of compact taper and gratings for mode coupling to SOI waveguides at C-band," *J. Mod. Opt.*, vol. 67, no. 12, pp. 1112–1119, 2020, doi: 10.1080/09500340.2020.1810797.

[80] P. Sethi, A. Haldar, and S. K. Selvaraja, "Ultra-compact low-loss broadband waveguide taper in silicon-on-insulator," *Opt. Express*, vol. 25, no. 9, p. 10196, 2017, doi: 10.1364/oe.25.010196.

[81] B. Luyssaert, P. Bienstman, P. Vandersteegen, P. Dumon, and R. Baets, "Efficient nonadiabatic planar waveguide tapers," *J. Light. Technol.*, vol. 23, no. 8, pp. 2462–2468, 2005, doi: 10.1109/JLT.2005.850795.

[82] Y. Fu, T. Ye, W. Tang, and T. Chu, "Efficient adiabatic silicon-on-insulator waveguide taper," *Photonics Res.*, vol. 2, no. 3, p. A41, 2014, doi: 10.1364/prj.2.000a41.

[83] A. S. Abdeen, A. M. Attyia, and D. Khalil, "Compact Adiabatic Taper for SOI Waveguide," *ACCS/PEIT 2019 - 2019 6th Int. Conf. Adv. Control Circuits Syst. 2019 5th Int. Conf. New Paradig. Electron. Inf. Technol.*, pp. 176–179, 2019, doi: 10.1109/ACCS-PEIT48329.2019.9062852.

[84] W. K. Burns, A. F. Milton, and A. B. Lee, "Optical waveguide parabolic coupling horns," *Appl. Phys. Lett.*, vol. 30, no. 1, pp. 28–30, 1977, doi: 10.1063/1.89199.

[85] A. F. Milton and W. K. Burns, "Mode Coupling in Optical Waveguide Horns," *IEEE J. Quantum Electron.*, vol. 13, no. 10, pp. 828–835, 1977, doi: 10.1109/JQE.1977.1069240.

[86] Z. Zhang, Y. Wang, and H. K. Tsang, "Ultracompact 40-Channel Arrayed Waveguide Grating on Silicon Nitride Platform at 860 nm," *IEEE J. Quantum Electron.*, vol. 56, no. 1, 2020, doi: 10.1109/JQE.2019.2951034.

[87]   D. Mao *et al.*, "Adiabatic Coupler with Nonlinearly Tapered Mode-Evolution Region," *IEEE Photonics Technol. Lett.*, vol. 33, no. 16, pp. 840–843, 2021, doi: 10.1109/LPT.2021.3072787.

[88]   K. Pierscinski *et al.*, "Optimization of Cavity Designs of Tapered AlInAs/InGaAs/InP Quantum Cascade Lasers Emitting at 4.5 μm," *IEEE J. Sel. Top. Quantum Electron.*, vol. 25, no. 6, pp. 1–9, 2019, doi: 10.1109/JSTQE.2019.2948500.

[89]   X. Li *et al.*, "Development of a High-Power Surface Grating Tunable Distributed-Feedback Bragg Semiconductor Laser Based on Gain-Coupling Effect," *Appl. Sci.*, vol. 12, no. 9, 2022, doi: 10.3390/app12094498.

[90]   T. Sahraeibelverdi, L. J. Guo, H. Veladi, and M. R. Malekshahi, "Polymer ring resonator with a partially tapered waveguide for biomedical sensing: Computational study," *Sensors*, vol. 21, no. 15, pp. 1–8, 2021, doi: 10.3390/s21155017.

[91]   C. Ozcan, J. S. Aitchison, and M. Mojahedi, "Adiabatic Waveguide Taper Profile Optimization on Al2O3/Si Platform for Polarization Insensitive Fiber-to-Chip Light Coupling," vol. 20, no. 1, p. 1500224, 2021.

[92]   G. Pedrola, *Beam Propagation Method for Design of Optical Waveguide Devices*. John Wiley & Sons, Ltd., 2015. doi: 10.1002/9781119083405.

[93]   D. Chack and S. Hassan, "Design and experimental analysis of multimode interference-based optical splitter for on-chip optical interconnects," *Opt. Eng.*, vol. 59, no. 10, pp. 1–11, 2020, doi: 10.1117/1.oe.59.10.105102.

[94]   Z. L. Hussain and R. S. Fyath, "Design and simulation of a compact three-mode (de)multiplexer based on a subwavelength grating multimode interference coupler," *Photonics Nanostructures - Fundam. Appl.*, vol. 47, no. March, p. 100966, 2021, doi: 10.1016/j.photonics.2021.100966.

[95]   F. Wang, X. Xu, C. Sun, and J. Zhao, "Ultracompact 1310/1550 nm wavelength demultiplexer based on subwavelength grating-assisted multimode interference coupler," *Opt. Eng.*, vol. 60, no. 08, pp. 1–7, 2021, doi:

10.1117/1.oe.60.8.087104.

[96] E. C. M. Pennings *et al.*, "Ultracompact, low-loss directional couplers on InP based on self-imaging by multimode interference," *Applied Physics Letters*, vol. 59, no. 16. pp. 1926–1928, 1991. doi: 10.1063/1.106188.

[97] P. E. Morrissey, H. Yang, R. N. Sheehan, B. Corbett, and F. H. Peters, "Design and fabrication tolerance analysis of multimode interference couplers," *Opt. Commun.*, vol. 340, pp. 26–32, 2015, doi: 10.1016/j.optcom.2014.11.083.

[98] R. U. and T. Kamiya, "Resolution of self-images in planar optical waveguides," *Opt. Soc. Am.*, vol. 68, no. 5, pp. 583–592, 1978.

[99] L. B. Soldano and E. C. M. Pennings, "Optical Multi-Mode Interference Devices Based on Self-Imaging: Principles and Applications," *J. Light. Technol.*, vol. 13, no. 4, pp. 615–627, 1995, doi: 10.1109/50.372474.

[100] X. Wang, C. Yin, W. Yuan, Y. Li, C. Li, and M. Xu, "Lateral shift assisted by guided modes on a metal cladding planar waveguide of micrometer scale," *Opt. Commun.*, vol. 343, pp. 47–50, 2015, doi: 10.1016/j.optcom.2015.01.006.

[101] M. BŁahut and D. Kasprzak, "Multimode interference structures -properties and applications," *Opt. Appl.*, vol. 34, no. 4, pp. 573–587, 2004.

[102] M. Kuznetsov, "Radiation Loss in Dielectric Waveguide Y-Branch Structures," vol. L, no. 3, pp. 3–6, 1985.

[103] H. Hatami-Hanza, M. J. Lederer, P. L. Chu, and I. M. Skinner, "A Novel Wide-Angle Low-Loss Dielectric Slab Waveguide Y-Branch," *J. Light. Technol.*, vol. 12, no. 2, pp. 208–214, 1994, doi: 10.1109/50.350602.

[104] C. Hsu, H. Chen, and W. Wang, "Compact Y -Branch Power Splitter Based on Simplified Coherent Coupling," *Technology*, vol. 15, no. 8, pp. 1103–1105, 2003.

[105] J. J. Su and W. S. Wang, "Novel coherently coupled multisectional bending optical waveguide," *IEEE Photonics Technol. Lett.*, vol. 14, no. 8, pp. 1112–1114, 2002, doi: 10.1109/LPT.2002.1021986.

[106] P. Wang, G. Brambilla, Y. Semenova, Q. Wu, and G. Farrell, "Design of an Extra-low-loss Broadband Y-branch Waveguide Splitter Based on a Tapered MMI Structure," *30th Prog. Electromagn. Res. Symp.*, pp. 1483–1486, 2011, doi: 10.1364/AO.41.007644.

[107] Y. Zhang *et al.*, "A compact and low loss Y-junction for submicron silicon waveguide," *Opt. Express*, vol. 21, no. 1, p. 1310, 2013, doi: 10.1364/oe.21.001310.

[108] I. A. Krutov, M. Y. Saygin, I. V. Saygin, and S. P. Kulik, "Optimized low-loss integrated photonics silicon-nitride Y-branch splitter," vol. 020027, no. June, pp. 1–5, 2020.

[109] R. Peyton, J. Martinez, F. A. Videla, and G. A. Torchia, "A small footprint Y-branch power splitter based on simplified coherent coupling on Silicon Nitride," no. August 2021, p. 36, 2021, doi: 10.1117/12.2593727.

[110] R. W. Purnamaningsih, N. R. Poespawati, T. Abuzairi, S. Rahardjo, M. Hamidah, and E. Dogheche, "The effect of waveguide parameters on gan based S-bend Y-junction optical power divider," *15th Int. Conf. Qual. Res. Int. Symp. Electr. Comput. Eng.*, vol. 2017-Decem, pp. 353–356, 2017, doi: 10.1109/QIR.2017.8168510.

[111] H.-C. Chung and S.-Y. Tseng, "Ultrashort and broadband silicon polarization splitter-rotator using fast quasiadiabatic dynamics," *Opt. Express*, vol. 26, no. 8, p. 9655, 2018, doi: 10.1364/oe.26.009655.

[112] K. K. Chung, H. P. Chan, and P. L. Chu, "A 1 × 4 polarization and wavelength independent optical power splitter based on a novel wide-angle low-loss Y-junction," *Opt. Commun.*, vol. 267, no. 2, pp. 367–372, 2006, doi: 10.1016/j.optcom.2006.06.048.

[113] S. Sereˇcunovʹ, D. Seyringer, H. Seyringer, and F. Uherek, "Design and optimization of 1 × 2 N Y-branch optical," vol. 71, no. 5, pp. 353–358, 2020, doi: 10.2478/jee-2020.

[114] S. Kumari and S. Prince, "Broadband Planar Waveguide Power Splitter Based

on Symmetrical S-bends," *2022 Int. Conf. Wirel. Commun. Signal Process. Networking, WISPNET 2022*, pp. 231–235, 2022, doi: 10.1109/WiSPNET54241.2022.9767169.

[115] P. Gaso *et al.*, "3D Polymer Based 1x4 Beam Splitter," *J. Light. Technol.*, vol. 39, no. 1, pp. 154–161, 2021, doi: 10.1109/JLT.2020.3026170.

[116] H. S. Jung, "A Study on the Design of Integrated-Optic Biosensor based on the Power Coupling of Two Modes utilizing Si3N4Rib-Optical Waveguides," *Proc. Int. Conf. Numer. Simul. Optoelectron. Devices, NUSOD*, vol. 2020-Septe, pp. 91–92, 2020, doi: 10.1109/NUSOD49422.2020.9217690.

[117] D. F. G. Gallagher and T. P. Felici, "Eigenmode expansion methods for simulation of optical propagation in photonics: pros and cons," *Integr. Opt. Devices, Mater. Technol. VII*, vol. 4987, p. 69, 2003, doi: 10.1117/12.473173.

[118] J. Bolk *et al.*, "Deep UV Lithography Process in Generic InP Integration for Arrayed Waveguide Gratings," *IEEE Photonics Technol. Lett.*, vol. 30, no. 13, pp. 1222–1225, 2018, doi: 10.1109/LPT.2018.2840224.

[119] V. H. Nguyen, I. K. Kim, and T. J. Seok, "Low-loss and broadband silicon photonic 3-db power splitter with enhanced coupling of shallow-etched rib waveguides," *Appl. Sci.*, vol. 10, no. 13, pp. 22–24, 2020, doi: 10.3390/app10134507.

[120] J. Talghader and J. S. Smith, "Thermal dependence of the refractive index of GaAs and AlAs measured using semiconductor multilayer optical cavities," *Appl. Phys. Lett.*, vol. 335, p. 335, 1995, doi: 10.1063/1.114204.

[121] J. Pyo Kim and A. M. Sarangan, "Temperature dependent sellmeier equation for the refractive index of AlxGa1-xAs," *Opt. Lett.*, vol. 32, no. 5, pp. 1–3, 2007.

Contributions

- T. R. Albiladi, D. M. Beggs, E. Le Boulbar and P. M. Smowton, (2018) "Modelling of single-mode GaAs-based 1x2 MMI and Y-branch splitters", Semiconductor and Integrated Optoelectronics (SIOE) Conference, 2018.

- T. R. Albiladi, D. M. Beggs, E. Le Boulbar, Z. Li, S. Shutts and P. M. Smowton, (2018) "Modelling, Fabrication and Characterization of Single-Mode GaAs-based 1x2 MMI splitter", UK Semiconductors Conference, 2018.

- T. R. Albiladi, D. M. Beggs, F. T. AlBeladi, S. Shutts, and P. M. Smowton, (2022) "Design and Optimisation of Tapered Waveguides", Semiconductor and Integrated Optoelectronics (SIOE) Conference, 2022.

- F. T. Albeladi, S. Gillgrass, T. R. Albiladi, S. Shutts, M. Tang, H-Y. Liu and P. M. Smowton, "Design of Low-Loss GaAs Based Optical Waveguides Incorporating Low-Index AlOx Layers.", Semiconductor and Integrated Optoelectronics (SIOE) Conference, 2022.

- T. R. Albiladi, D. M. Beggs, F. T. Albeladi, S. Gillgrass, S. Shutts and P. M. Smowton, (2022) "GaAs-Based Efficient Y- Splitter Design Rules", UK Semiconductors Conference, 2022.

- F. T. Albeladi, S. Gillgrass, J. Nabialek, P. Mishra, R. Forrest, T. R. Albiladi, S. Shutts, M. Tang, H-Y. Liu and P. M. Smowton, " Multimode Interference Reflector-based InAs-QD Laser", UK Semiconductors Conference, 2022.

- F. T. Albeladi, S. Gillgrass, J. Nabialek, P. Mishra, R. Forrest, T. R. Albiladi, S. Shutts, M. Tang, H-Y. Liu and P. M. Smowton, " Multimode Interference Reflector-based InAs-QD Laser", International Semiconductor Laser Conference (ISLC), 2022.

- F. T. Albeladi, Sara-Jayne Gillgrass, Josie Nabialek, Pawan Mishra, Richard Forrest, T. R. Albiladi, Craig Allford, Samuel Shutts, Mingchu Tang, Hui-Yun Liu and Peter M. Smowton "Realisation of Multi-Mode Reflector Lasers for Integrated Photonics", CLEO®/Europe-EQEC, 2023.

- F. T. Albeladi, Sara-Jayne Gillgrass, Josie Nabialek, Pawan Mishra, Richard Forrest, T. R. Albiladi, Craig Allford, Samuel Shutts and Peter M. Smowton,

"Multi-Mode Interference Reflector for Integrated Photonics", Semiconductor and Integrated Optoelectronics (SIOE) Conference, 2023.